Design of a Helicopter Slung Vehicle for Actuated Payload Placement

Robert James Collins

Thesis submitted to the faculty of the
Virginia Polytechnic Institute and State University
in partial fulfillment of the requirements for the degree of

Master of Science
In
Mechanical Engineering

Kevin B. Kochersberger, Chair
Christopher B. Williams
Alexander Leonessa

April 12, 2012
Blacksburg, Virginia

Keywords: Tethered Payload, Helicopter, Slung Load, Autonomous Systems

Design of a Helicopter Slung Vehicle for Actuated Payload Placement

Robert James Collins

Abstract

Helicopters have been used in applications where they need to carry a slung load for years. More recently, unmanned (UAV) helicopters are being used to deliver supplies to military units on the ground in theaters of war. This thesis presents a helicopter slung vehicle used to carry the payload and furthermore, provide a means of actuation for the payload. This provides more control authority to the system and may ultimately allow a helicopter to fly higher with a longer tether.

The vehicle designed in this thesis was designed for use with 100kg class helicopters, such as the Yamaha RMAX operated by the Virginia Tech Unmanned Systems Lab. Each system on the vehicle was custom designed – including the propulsion system, wall detection / localization system, and controller. Three shrouded propellers provided thruster actuation. A scanning laser range finder and inertial measurement unit (IMU) were used to provide localization. A first attempt at a linear full state feedback controller with a complementary filter was used to control the vehicle.

All of the systems were tested individually for functionality. The shrouded propellers met their design goals and were capable of producing .7lbf of thrust each. The wall detection system was able to detect walls and windows reliably and with repeatability. Results from the controller however were less than ideal, as it was only able to control yaw in an oscillatory motion, most likely due to model deficiencies. A reaction wheel was used to control yaw of the vehicle with more success.

Acknowledgements

I'd like to first acknowledge and thank my advisor, Dr. Kevin Kochersberger, for allowing me to work in the lab and furthermore, allowing me to work on this project. In addition, I would like to thank the other members of my committee for their assistance.

I'd also like to thank those whom I've worked with over the past year in the Unmanned Systems Lab. Starting off; I'd like to thank Ken Kroeger, for providing assistance whenever possible, including his time in the machining of some of the components that made up this assembly. In addition, I'd like to thank Bryan Krawiec and Pete Fanto for their insight as well. Those others who also worked in the USL need to be acknowledged, for they also provided at the very least an occasional distraction, which was critical in the interest of my sanity.

Finally, I'd like to thank my family and my parents for their encouragement and support. They encouraged me to work hard and to continue my education.

All photos by the author, 2012.

Table of Contents

List of Figures

List of Tables

List of Symbols

The following symbols were used for ***shrouded propellers***:

T	static thrust
A	area
ρ	density of air
P	power
M	factor of merit
D	diameter

The following subscripts were used for ***shrouded propellers***:

s	shrouded propeller
f	free propeller
e	exit
p	propeller disc

The following symbols were used for ***wall detection***:

R	distance
x	Cartesian x coordinate
y	Cartesian y coordinate
θ	angle of wall

The following subscripts were used for ***wall detection***:

i	i^{th} point, counter

The following symbols were used for the ***mechanical design***:

M	moment
x	position along beam
ω	loading per length

δ	deflection
σ	normal stress
c	distance from neutral axis
E	modulus of elasticity
I	area moment of inertia
l	length of beam

The following symbols were used for spherical ***pendulum dynamics***:

θ	pendulum angle
φ	precession angle

The following symbols were used for ***linear control dynamics***:

J	vehicle moment of inertia
I	reaction wheel moment of inertia
θ	yaw angle
R	thruster moment arm
T	thrust
c	linear damping coefficient
m	mass
x	position from wall
φ	angle of thrusters
g	gravitational constant
L	tether length
e	bias error
t	time
b	bias
τ	filter time constant

s	Laplace variable
K	gain matrix
A	impulse amplitude
ζ	damping ratio
T	vibration period
ω	frequency, rad/s

The following subscripts were used for linear control dynamics:

1	station 1
2	station 2
3	station 3
4	station 4
i	i^{th} impulse, counter
w	reaction wheel

Chapter 1
Introduction

This thesis presents the design of a helicopter slung vehicle actuated by three thrusters for payload placement control, with the ultimate goal of increasing the slung-load system's total control authority and stability. The vehicle will be used for the actuated placement of payloads from a mid-sized 100kg class unmanned helicopter. This can be useful in applications where a tethered payload needs to navigate a small area and / or an area that may consist of obstacles such as buildings or irreplaceable property. A hypothetical system consisting of an actuated slung vehicle is shown in Figure 1.1.

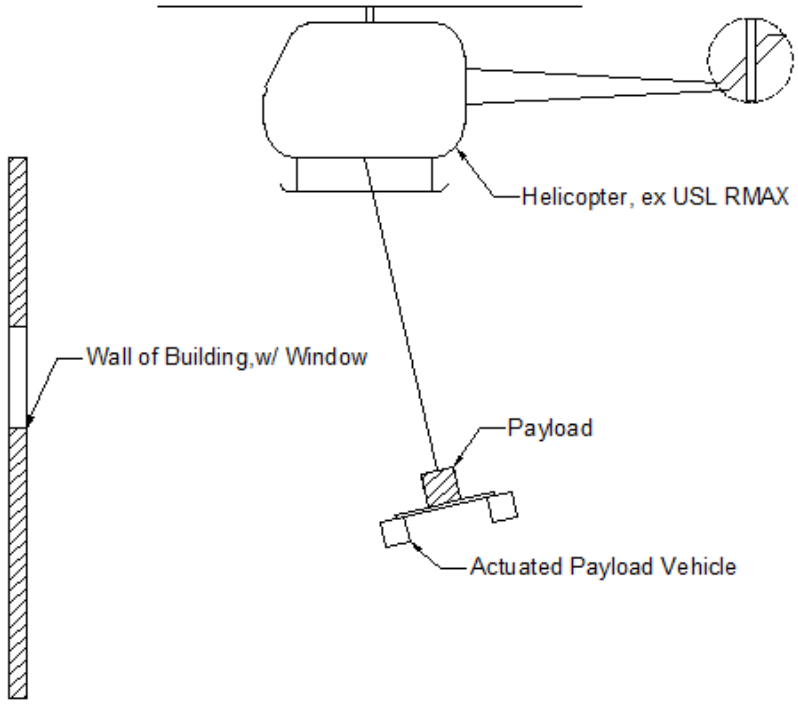

Figure 1.1. A slung payload with an actuated payload vehicle. The actuated payload vehicle provides more control authority to the slung-load system.

Helicopters and fixed wing aircraft are regularly used to deliver equipment and supplies quickly and effectively. Aircraft are used in this capacity routinely with the armed forces, commercial operations, and for humanitarian aid. Helicopters in particular are used routinely in conjunction with slung / tethered payloads. Such examples include aerial cranes, firefighting, and military operations. However, such operations can be unsafe for not only people and property on

the ground, but also for the pilot / crew and the payload itself. This thesis presents a tethered vehicle with thrusters, a navigation system, and a controller that can be used to place payloads on the ground and avoid obstacles (such as walls), as shown previously in Figure 1.1. In normal tethered payload operations, the helicopter is used to position the payload. This thesis presents a vehicle capable of carrying a 5kg payload of which can actuate and position itself.

Each of the different subsystems used in the vehicle – propulsion, wall detection, and the controller had to be designed. Software to debug and control the vehicle was written for the onboard computer and microcontroller. The vehicle was fabricated as a 16”x16” planform area, weighing 8.1lb empty. After fabrication, the vehicle was tethered to a fixed point at the Unmanned Systems Lab to begin testing it. This thesis presents the design, research, fabrication, and testing of the tethered vehicle.

1.1 Project Motivation

Payloads are currently slung / tethered from helicopters using relatively short tethers lengths. This allows the helicopter to provide position control of the payload. However, situations may arise where the payload needs to be navigated and placed near buildings, people, or other areas where property damage and harm could occur. In these situations, control authority of the helicopter may not be enough, especially if disturbances such as wind, gusts, rotor downwash, etc impact the payload. Depending on the amplitude of the sway, the helicopter itself may become uncontrollable.

In addition, long tether operations may be of interest. Using a long tether, helicopters can fly at a higher altitude. In a military application, this would permit a helicopter to fly out of acoustic range and to avoid small arms fire. Controlling a tethered payload with a long tether can present issues due to the disturbances and large accelerations that the helicopter must undergo to cancel out the sway. It is likely that the helicopter will not have enough control authority for a payload slung by a long tether, thus an actuated vehicle will likely need to be used for control. While long tether operations were not a focus of this particular thesis, the vehicle developed in this thesis could potentially be used in long tether operations utilizing the proper control techniques.

Even though the dynamics derived in this thesis only account for short tether operations, a practical implementation of the vehicle is still novel and useful. Unmanned helicopters have

only recently been used to carry tethered payloads. Utilizing a vehicle with thruster actuators to carry the payload can help with positioning and the overall control of the system, providing a factor of safety.

1.1.1 Design Requirements

Considering the overall motivation of the project, several broad design requirements of the vehicle can be derived. These include:

- ***The vehicle must be able to locate obstacles and position itself.*** This is the crux of the problem. In order to position itself without the aid of the helicopter, the vehicle needs to have onboard thrusters. Localization of obstacles such as walls is necessary for the controller to actuate the thrusters.
- ***The vehicle must be able to localize itself using onboard sensors.*** It is necessary to develop a vehicle that can localize and control itself / the payload using only the information gathered by onboard sensors and without the aid of GPS. This eliminates the need to communicate to the helicopter for orientation information and provides reliable measurements of the dynamic states. The vehicle will need to be completely self-powered.
- ***The vehicle must weigh less than 5kg empty and must be able to carry a payload of 5kg.*** This requirement is derived from the typical maximum payload of the 100kg class helicopter (10kg). The tethered vehicle developed in this thesis was designed to be tethered with the Virginia Tech Unmanned Systems Lab's RMAX helicopter.

1.2 Overview of Thesis

This thesis first presents the previous work done in the field of tethered operations and payload control. In particular, this includes research on sway control of cranes and control techniques such as input shaping. Since the vehicle encompasses multiple, very different systems, the theory used to design each individual system (propulsion, wall detection, etc) is presented as well.

The design and performance of each system is then discussed. The propulsion system is first presented. Starting off with the design requirements, the fundamental theory and prior

research conducted on shrouded propellers is discussed in more detail. A design which results in a 5” inner diameter shroud results and is presented along with relevant (static thrust) test data and characterization curves.

Next, the wall and window detection algorithm are discussed. A theoretical overview of the Hough transform as a line detection technique (used to detect walls, which would likely be an obstacle to avoid while the vehicle is deployed) is given. The actual implementation using a scanning laser range finder and a custom written LabVIEW program is then presented. Performance is shown in terms of computational speed and measurement repeatability.

The next chapter presents the system architecture and mechanical design of the overall tethered vehicle. The electrical hardware is selected, including the inertial measurement unit, the laser range finder, and the onboard computer / wireless communication hardware. Basic control theory is then discussed as it was used to ensure the vehicle would remain controllable. The resultant mechanical design is then presented.

System dynamics and the controller are then discussed. The linearized equations of motion are presented along with the accompanying linear control law used. The vehicle controller is coded, implemented, and tested in this chapter.

Finally, the thesis concludes with a summary of work and suggestions for future work / improvements. Several deficiencies presented themselves, mostly during the implementation of the controller. These deficiencies are discussed with suggestions on how to minimize them.

Chapter 2
Literature Review

Designing a helicopter tethered vehicle for supplying ground units requires many sub-systems. In particular, such a vehicle would need a vision system to detect obstacles for the ultimate goal of locating and avoiding them. Once an obstacle is located, a propulsion system is necessary to ensure the vehicle does not collide with the obstacle. Finally, in order to control the vehicle in a meaningful manner, a controller would need to be implemented. This chapter discusses an overview of each of these systems that were used in the design and fabrication of the resupply vehicle.

2.1 Current Supply Techniques

Airborne supply missions have been and will continue to be a critical component of modern logistics. Aircraft have been delivering supplies in a commercial, humanitarian, and military capacity for almost as long as airplanes have been around. In World War II, accompanying the development of airborne paratrooper units, military units began to airdrop supplies to ground units by strapping parachutes to cargo. Airdrop techniques evolved as loads and requirements changed. Various methods exist for extracting loads out of airplanes and to slow the rate of decent of the airdropped cargo [1]. Different aircraft have evolved and are used for different missions and load carrying capability. Today, the United States Air Force's C-5 Galaxy is able to air drop 200,000 pounds of material utilizing multiple pallets [1].

Airdrops are effective at distributing large amounts of cargo. However, they're not the only technique used to deliver supplies in the military's supply chain. If there is a large enough airstrip in the destination area, cargo aircraft can land to deliver supplies. Vehicle convoys are often used to deliver supplies and transport people. Helicopters are used frequently as well, especially in areas that have little to no supporting infrastructure (roads, bridges, runways) and may be home to dangerous terrain.

Helicopters are often used to transport large loads, often larger than the helicopter is itself. This requires the load to be tethered to the helicopter. Tethering a load to a helicopter is not entirely new. This is a common practice with helicopters used in aerial firefighting and as aerial cranes. The Unmanned Systems Lab at Virginia Tech routinely executes tethered payload

operations from a Yamaha RMAX, mostly utilizing it to deploy a ground based tracked robot. This is shown in Figure 2.1.

Figure 2.1. A ground robot being deployed from the VT Unmanned System Lab Yamaha R-MAX.

In December 2011, autonomous K-MAX helicopters developed by Lockheed Martin and Kaman went into service for the sole purpose of transporting supplies. The Navy's major motivation for developing this project was to avoid the hazards of ground based supply convoys, as they are easily targetable by makeshift explosives. Operating since December 17, 2011, the helicopters have been successful at delivering more than 100,000lbs as of January 31, 2012 [2].

2.2 Control of Tethered Systems

Tethered systems such as a tethered payload attached to a helicopter or to a crane are often times uncontrolled. Depending on the mechanics of the system, this may or may not be acceptable. For example, if a long tethered payload is attached to a crane, a disturbance or even the stoppage of the crane could cause the payload to sway. This could be dangerous to property or people in the surrounding area. Sway can also influence the system's speed and accuracy.

To address the problem of sway, engineers have most notably used a technique called input shaping. Input shaping is a feed-forward control technique, not requiring any

instrumentation for feedback. Rather, the input shaper only requires knowledge of the natural frequency of the system. By utilizing the natural frequency of the system, the input shaper manipulates the user's desired commands to effectively cancel out the system sway [3].

This technique has been used with success in many crane applications. Singhose et al describes numerous industrial applications where cranes have utilized input shaping. Such applications include shipyards, nuclear power plants, and warehouses [4]. Even though input shaping is successful in many applications, it does have its deficiencies. Such an example is a tower crane, where slewing motions are common. In these instances where nonlinear dynamics are prevalent, other command shaping techniques are used. Lawrence and Singhose describe and verify in their command shaping techniques for a tower crane setup in [5]. Several command shapers are demonstrated to reduce vibrations considerably. In the experiments conducted in [5], it is still found that conventional input shapers can still control vibrations, although at a degraded performance.

As stated earlier, helicopters often carry tethered payloads. If such a payload were to sway, it could result in stability issues for the helicopter pilot or if unmanned, a flight controller. Such systems have been mathematically modeled and studied extensively to eliminate dangerous sway. R.A. Stuckey models and simulates slung-load systems from helicopters in [6]. In particular, he looked at the open-loop system dynamics of the CH-47D Chinook with various slung loads and analyzed stability for various load-to-helicopter mass ratios. James May wrote his Master's thesis on tethered payload control for an autonomous helicopter, featuring a simulated payload oscillation controller. This was achieved by hoisting the load with the onboard winch using a passive controller [7]. The Georgia Tech Input Shaping Lab is researching helicopter sling load dynamics and the influence of using input shaping on the helicopter's handling qualities [8]. This is part of an effort to reduce sway and oscillations of the payloads of flying cranes.

In conducting this literature search, no techniques were found involving thrusters on the payload vehicle itself. However, Agrawal et al explored dynamics and control from a helicopter using a multiple-cable suspended robot in [9]. Their work focused on controlling the helicopter for large motions and to use the cable system for fine positioning of their payload robot. The cable system for the robot utilized a nonlinear sliding mode controller. Results were obtained by simulations only.

2.3 Propulsion System

Rather than relying on the helicopter to provide position control of the payload, the vehicle presented in this thesis utilizes onboard thrusters. There isn't one single piece of machinery for airborne vehicles to provide thrust / act as a thruster. For example, propellers, shrouded propellers, and turbines are all fairly common to be found on airborne vehicles. The choice of such a propulsion system depends upon the vehicle's requirements and operating environment.

Propellers used in an aerodynamic sense are as old as powered flight, first being used successfully to power the world's first powered airplane, the Wright Flyer, in 1903. As aviation progressed, so did propellers. Even though propellers are essentially spinning airfoils, there are many different forms of propellers in existence today. A unique application and modification of the propeller is the shrouded propeller / ducted fan. Shrouded propellers often find themselves used in applications where high static thrust is desired, such as hover or low speed operations. Used in many small UAVs, shrouded propellers offer the advantage of minimizing tip losses and downstream contraction, thus minimizing power requirements.

Research into shrouded propeller performance was largely executed by NACA during the mid-1940s thru the 1970s. NACA technical memorandum (TM) 1202 [10] is arguably one of the most complete resources for characterization of shrouded propellers. In [10], W. Kruger tests and characterizes a shrouded propeller in static and wind tunnel tests. Different shroud and propeller geometry is tested and characterized, such as the lip, chord, profile thickness, etc. Data is presented supporting the claim that shrouded propellers can offer better static thrust than a free propeller [10].

Robert Platt also researched static thrust of shrouded and free propellers in [11]. His tests involved two propellers – one free, and one shrouded. He found that for the equivalent amount of power, the shrouded propeller produced twice the static thrust of the free propeller. Other parameters such as diffuser area and shroud length were tested as well [11]. Platt also provides a theoretical momentum derivation of shroud and free propellers in static conditions.

Harvey Hubbard executed experiments to characterize the acoustics of a shrouded propeller while it was used to generate static thrust in [12]. In his test, five separate shrouded propellers were tested and compared to a free propeller. Keeping diameter and rotational speed / power relatively constant, he found that reducing the tip speed and increasing the blades had the

effect of reducing the acoustic signature. These findings applied both for the shrouded and free propellers. Hubbard's experiments indicated that the flow quality was arguably the single most influential factor in the acoustic quality of the shroud. Depending upon the quality of attachment, noise could be reduced by ½ or increased by a factor of two as compared to a free propeller [12].

Donald Black et al of United Aircraft Corporation in [13] presented a performance study of shrouded propellers. In their study, various shroud geometric parameters are changed. Performance data is then compared to a baseline shrouded propeller. Experiments were executed for static thrust conditions and multiple Mach numbers. Ultimately, their study concluded that the area ratio of the shroud (diffuser cross sectional area to propeller disc area) is the most critical parameter in terms of performance change for static thrust [13].

These resources proved critical in the design of the shrouded propeller propulsion system employed by the vehicle as extensive flow characterization and experimental aerodynamic techniques were not used to iterate the design.

2.4 Line Detection

The tethered vehicle must be able to detect the surrounding environment. There are many different ways to do this. For example, image processing to detect feature points or edges of interest may be used. Various instruments can be used to collect this data, such as cameras, LIDAR, etc. In the case presented in this thesis, a scanning laser range finder was used for reasons explained in Chapter 4.

The laser range finder used on this vehicle returns a data vector of a distance and angle of a point in a single plane (2D environment). These points may or may not represent a line. Many techniques can be used to determine if a line can be drawn from the points, however, many methods are computationally inefficient. Utilizing the Hough transform however, a wall can be detected from a data vector quickly. Originally patented in the 1960s, the Hough transform is a useful and time proven tool in calculating lines from images. Richard Duda and Peter Hart from the Artificial Intelligence Center presented the Hough transform to detect lines in an image using a digital computer in [14]. In their work, they explore the use of an angle and distance (normal) parameter space. Computational time is explored as a function of quantization interval / accumulator array size.

Even though the Hough transform has been implemented for some time with success, there have been efforts to improve it. Probabilistic techniques have been implemented and used

in effort to reduce the computation time. An example of such a technique is described in Galambos et al in [15]. Their work leads to the development of the Progressive Probabilistic Hough Transform algorithm. Other techniques such as the Randomized Hough Transform exist as well. In each case, computational time is reduced [15] [16].

The instrumentation to orient the vehicle / payload in its surroundings does not necessarily need to be located on the vehicle itself. Instead, a vision system may be located on the helicopter (which would probably only be useful for relatively short tether lengths). Lawrence and Singhose describe using a Siemens camera mounted to a crane trolley to capture sway motions in [5]. They do not describe the processing techniques they used, but it is likely that feature points of the vehicle could be detected, depending on tether length.

Chapter 3
Propulsion System Design

In order to avoid obstacles and to navigate to a particular location, a helicopter-deployable vehicle must have an independent propulsion system. This chapter discusses the methodology behind the propulsion system design.

3.1 Propulsion System Requirements

Since the vehicle is tethered to a helicopter, the propulsion system does not need to generate enough thrust to support the vehicle outright on its own. Instead, the propulsion system needs only to provide enough thrust to move and rotate the vehicle in the horizontal plane (perpendicular to the direction of gravity). Since the thrust-to-weight ratio of the vehicle can be far less than 1, smaller, lighter, and cheaper propulsion mechanisms can be used. In particular, the propulsion system must satisfy the following requirements:

- ***Low Weight.*** Since the primary mission of this vehicle is to deliver supplies to ground units, it is desired that the propulsion system be as light as possible. Having an unnecessarily heavy system only robs the amount of weight that the user can load onto the vehicle, as the gross weight of any helicopter is limited. For this particular vehicle, considering the gross weight limitations of the Virginia Tech Unmanned Systems Lab's RMAX, it is desired to develop a propulsion system that weighs less than 4lb, which is about a third of the desired vehicle's empty weight.
- ***Adequate Thrust Output.*** An important aspect of this vehicle is to avoid obstacles. In order to do this successfully, the vehicle must be able to respond quickly to an acquired obstacle to navigate around it or to stop before colliding with it. This requirement of course depends on the total mass / inertia of the vehicle and its payload. It is desired to have enough thrust output to accelerate the vehicle .1g in some direction to be able to avoid a collision with a wall / obstacle. Assuming the vehicle weighs about 10-11lb, it would then be desired to have the capability to output about 1lbf.
- ***Low Energy Consumption.*** The vehicle is completely independent from the helicopter. Therefore, energy to propel the vehicle must be stored on-board the vehicle. Since surface area is rather limited on the vehicle (to allow for as much area as possible to carry

supplies), this means that the amount of energy onboard is rather limited. It is desired to limit the power draw of the entire system to 200W at max thrust conditions. Limiting the power to this level ensures that we can minimize the amount of weight and area onboard the vehicle dedicated to energy storage. This energy consumption was also influenced by theoretical thrust and power relationships of propellers, which will be discussed later.

- ***Low Acoustic Signature.*** In a hypothetical resupply mission, it may be required to insert supplies in a location where noise generation is kept to a minimum. With this said, it is desired to keep the acoustic signature of the propulsion system to a minimum.

3.2 Selecting a Propulsion Method

After identifying the requirements, the first step in the design of a propulsion system is to determine the propulsion mechanism. Many choices exist today for propelling a vehicle through the air, including electric, piston, and turbine powered propellers. In addition, a hypothetical supply vehicle may be able to make use of a turbine engine. However, due to the size constraints imposed by the Yamaha RMAX, a turbine engine would simply be impractical. Thus, the propulsion system was designed around multiple propellers.

3.2.1 Power Generation and Delivery

Once a propulsion system with propellers as its thrust generating component was realized, the next step was to determine how exactly to deliver power to the propeller. In general, two power delivery methods exist – one, by making use of a small scale internal combustion engine, and two, by using a small scale electric motor. At the size and scale of the vehicle, a small internal combustion engine didn't satisfy the requirements. Even though the energy density of gasoline is extremely high (47MJ/kg) compared to a lithium ion battery (720kJ/kg), internal combustion engines tend to be larger, heavy, and loud. For example, consider the geometric profile of an engine versus an electric motor. Given that the rotor must rotate around the stator, electric motors tend to be round in nature. Conversely, small scale internal combustion engines have a crankshaft with a counterweight, a connecting rod, and a piston. In essence, linear motion of the piston is being converted to rotatory motion of the crankshaft, thus forcing the geometric profile of the internal combustion engine to be larger. In addition, small scale engines can in general provide far more power than the 200W maximum requirement. For these reasons, it was decided to use small electric motors (the Hacker A20-30M). The Hacker A20-30M is a 150W

peak motor, providing 980RPM/V. It measures slightly less than 1.100in in diameter. Even though the motor can provide 150W peak, it was hoped to use far less than that to meet the 200W maximum requirement.

Figure 3.1. The Hacker A20-30M brushless motor.

3.2.2 Addressing Power Consumption

After selecting an electric motor model to use, it was decided to look at ways to perhaps improve performance by maximizing thrust output and minimizing power consumption. These goals are obviously competing interests. Traditionally, engineers whom design propellers try to address propeller efficiency (thrust out for a given amount of power) by designing and tweaking the propeller airfoil. In addition, the propeller tips may be designed as they are also of concern. There are numerous reports such as [17] that detail the influence and design methodology of free propeller geometry

There are other methods to improve propeller efficiency. For example, the propeller can be placed in a circumferential shroud. Placing a propeller in a properly designed shroud increases the mass flow through the propeller disc as the air downstream of the propeller cannot contract like it could as if the propeller were free [13]. This effect is illustrated in Figure 3.2.

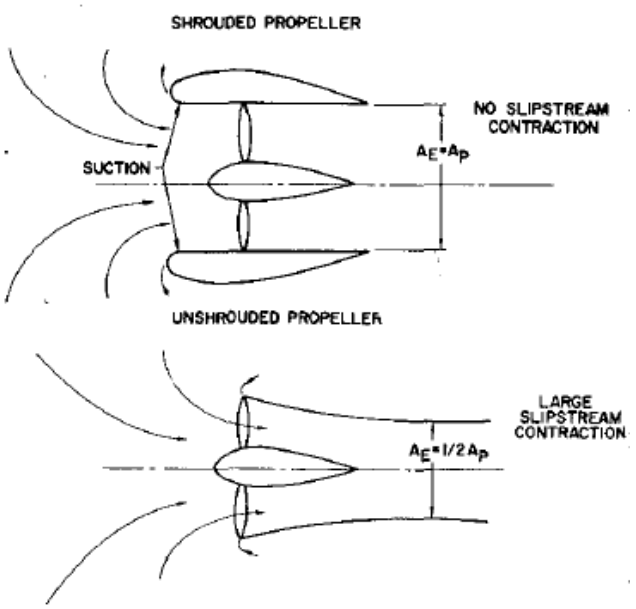

Figure 3.2. Flow field illustrated for the shrouded and free propeller cases. Preventing downstream contraction increases the mass flow rate thru the propeller disc substantially [13]. Reprinted with permission of the American Institute of Aeronautics and Astronautics.

By utilizing momentum theory to derive ideal static thrust performance equations, it becomes evident just how advantageous a properly designed shroud is. For example, utilizing equation 3.1 below, it becomes apparent that if the diffuser diameter is equivalent to the propeller / entrance diameter, a 26% increase in static thrust can be expected.

$$\frac{T_s}{T_f} = 1.26 \left(\frac{A_e}{A_p}\right)^{\frac{1}{3}} \tag{3.1}$$

A shroud is not limited to being constant in diameter. As equation 3.1 suggests, if the exit area, A_e, is greater than the area of the propeller disc, A_p, then the thrust produced by the shroud will increase. Equation 3.1, plotted in Figure 3.3, states that the thrust produced by the shrouded propeller will increase by the cubic root. However, it is possible that the thrust produced by the shroud would be greater than suggested by equation 3.1, as the loading on the propeller itself would be less [13].

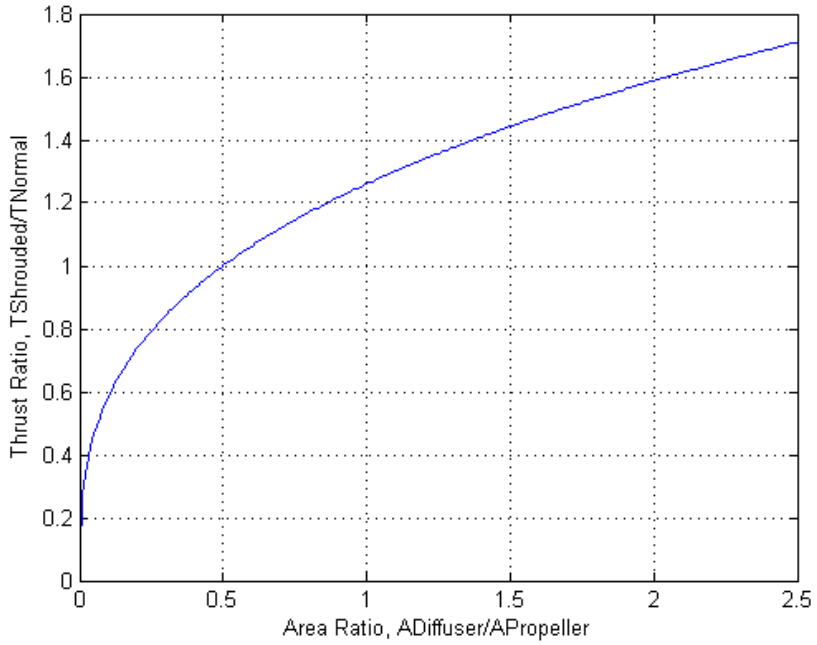

Figure 3.3. Theoretical thrust ratio for a given area ratio. It is likely that increasing the diffuser area would result in a greater thrust ratio than plotted here.

It is important to note that a properly designed shrouded propeller is also advantageous from a power consumption standpoint. Figure 3.4 plots the thrust as a function of power consumption as predicted by momentum theory for both the free and shrouded propellers. It is evident that not only are shrouded propellers able to produce more thrust (by limiting the downstream contraction [13]), but are also able to produce their thrust with a smaller power requirement [11].

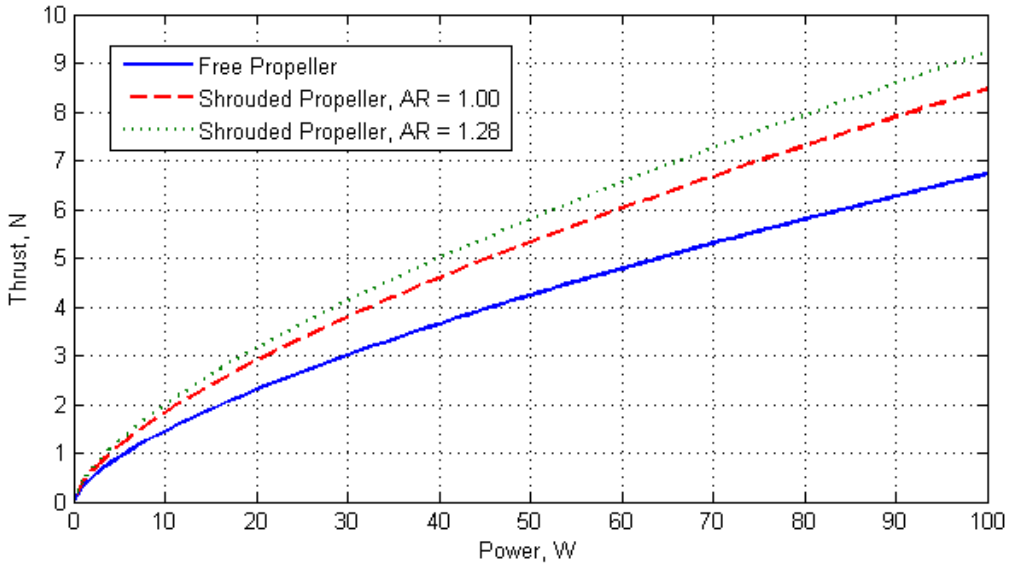

Figure 3.4. A plot of static thrust versus power required for an area ratio of 1.00 and 1.29. The shrouded propeller can generate more thrust for a smaller power requirement.

In addition to Figure 3.4, equations 3.2 and 3.3 quantify not only the thrust generated as a function of power, but also the dependence on the diffuser area and propeller disc area. Equation 3.2 in particular shows that increasing the exit / diffuser area has the added benefit of generating more thrust for the same amount of power. One must approach this result with caution – as momentum theory does not account for aerodynamic separation, a condition that would surely result if the cross sectional profile of the duct was too aggressive [13].

$$T_s = (\rho A_e)^{\frac{1}{3}}(2P)^{\frac{2}{3}} \tag{3.2}$$

$$T_f = \left(2\rho A_p\right)^{\frac{1}{3}}(P)^{\frac{2}{3}} \tag{3.3}$$

Shrouded propellers are very advantageous in the static thrust condition – that is to say, in the absence of significant axial or sideward motion. While shrouded propellers will still function at velocities seen in flight, their performance approaches that of a normal, free propeller. This is because the contraction of the flow-field downstream of the free propeller becomes less dramatic as forward velocity is increased [13]. Considering the likely missions of a tethered supply vehicle, it would be appropriate to assume that the velocities seen by the vehicle would be near-static thrust conditions (as it would be likely be deployed when the helicopter is in a quasi-hover state). For these reasons listed above, it was decided to base the propulsion system off of

shrouded propellers as opposed to free propellers. These reasons outweighed the trade-offs of using free propellers (ex extra weight due to the shroud), especially considering the vehicle's application.

3.3 Shrouded Propeller Design

With the shrouded propeller selected as the method of propulsion, the next step was to identify the requirements and finer details associated with shrouded propellers, ultimately to design them. This section of the chapter covers these requirements and the design process used to develop the shrouded propellers attached to the tethered supply vehicle.

3.3.1 Shrouded Propeller Requirements

To the naked eye, shrouded propellers are relatively simple pieces of machinery, consisting of a propeller, a motor / engine, and a shroud with stator blades. However, there are many finer points that must be addressed when designing a shroud. In particular,

- ***The inlet airflow to the propeller must not be separated.*** If separation occurs, the effectiveness of the propeller and thus, total thrust output is reduced. In addition, the noise generated by the shrouded propeller will increase due to the poor flow quality [12]. Minimizing inflow separation is principally addressed by the shape of the shroud lip. Separation of a curved profile is principally governed by radial forces, and occurs when the radial forces exerted on the flow exceed the pressure gradient generated, as shown in Figure 3.5 [18]. This suggests that the shroud lip will be of critical importance to the success of the propulsion system. In addition, the propeller position with respect to the shroud chord length can be an influential factor, as placing the propeller rearward can help in minimizing the asymmetrical effects of the inlet airflow [13].
- ***The tip clearance between the propeller and shroud wall must be minimized.*** In general, minimizing the tip clearance between the propeller blade and wall results in a higher net static thrust output per shroud [13]. This is especially true at low speeds, as will be experienced by the tethered supply vehicle (at higher speeds, minimizing the tip gap can result in adversely impacting thrust output, most likely due to the influence on the boundary layer). Many studies on shrouded propellers, such as in [11] and [13], focus on tip gaps in the .125% to .5% of propeller diameter range. This can be a difficult goal to achieve, as this can require difficult manufacturing tolerances. In addition, at very small

tip gaps, the rigidity of the shroud and propeller become important parameters as the radial extension of the propeller and the vibrational modes of the shroud may cause a collision between the shroud wall and propeller. There have been studies of developing specialized tips to decrease the "leakage" around the propeller blade such as in [19]. Such studies are extensive as they involve iterations of numerical methods and experimental testing and were considered out of the scope of this thesis. Tip clearances will be primarily addressed by minimizing the geometric clearance between the propeller blade and shroud wall in this work.

- ***The shroud must allow for diffusion and minimize downstream contraction.*** It is imperative that the shroud is long enough to minimize the downstream flow contraction. Especially at lower velocities, this requirement is reflected in the shroud length. In addition, if the shroud is to have a diffuser, the shroud must be long enough to allow for effective diffusing of the flow [13]. This requirement competes directly with the overall desired weight of the propulsion system as adding more length will increase the weight.
- ***The propeller must be designed such that stalling is avoided for the operating range.*** With the propeller being used to move the air mass through the duct, the propeller itself becomes an important variable. In essence, the propeller should be shaped (blade plan form area, blade number, chord length, twist, etc) such that thrust is produced and the blades do not stall [11]. Papers and reports have been written detailing how to design propellers to be specifically used in a shrouded propeller application such as [20] and [21] using blade element theory. However, investigating all of the parameters of a propeller is time intensive, expensive, requires specialized manufacturing process (propellers of this scale would most likely be injection molded, requiring tooling to be developed), and requires lots of experimental testing. Given the scope of this project, and considering the relatively low Reynolds numbers expected to be encountered, commercial propellers used conventionally on remote control aircraft will be used and modified to satisfy the geometric constraints of the shroud. Since the propeller is shrouded, the use of specialized tip geometry (as is sometimes done with a free propeller) will be of relatively small interest as the tip losses will be significantly reduced.

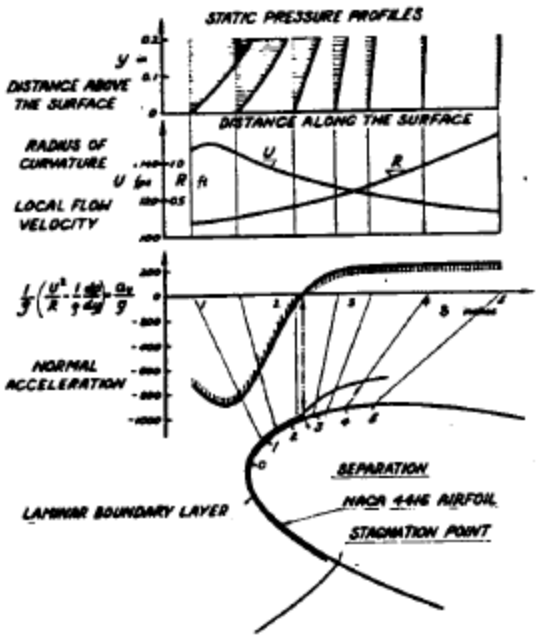

Figure 3.5. A plot of separation on a NACA 4416 airfoil. The separation is due to the radial force experienced by the flow [18]. Used with permission from the American Society of Mechanical Engineers.

3.3.2 Initial Shrouded Propeller Design

With the requirements identified, the next step was to start the design process to begin designing the shrouded propellers to be used as part of the vehicle's propulsion system. Being relatively limited on the overall amount of volume the entire vehicle could consume (as it was desired to design it to fit underside the Yahama RMAX helicopter – 16"x16"x9"), the diameter of the shrouds would have to be constrained. However, constraining the size of the shrouds too much would limit the amount of thrust that could be produced by the propulsion system, hampering the entire vehicle's performance. Using equation 3.2, one could assume a power and desired thrust output to find the exit area (and thus diameter). However, at the small scales being dealt with here, the Reynolds numbers are low; suggesting viscous effects are present and thus skin drag would be a real issue. It is therefore *expected* that the design will deviate significantly from the ideal momentum calculations.

Ultimately, a duct with a 6" major diameter was chosen to start with. This was decided mostly on geometric reasons (having only 9" to work with beneath the helicopter). With the Hacker A20-30M 150W peak motor selected, the next step was to determine the area of the propeller disc and the area of the diffuser. Recall from earlier Figures 3.3 and 3.4 that by

increasing the area ratio (A_e/A_p), a higher thrust output can be achieved. With the vehicle mostly living in the static thrust region, looking at the area ratio and diffusion was thought to be beneficial (in conventional aircraft, the drag and weight from the longer diffuser can negate the diffuser's presence). However, greatly increasing the area ratio, especially with a short shroud length, can adversely impact the design as diffuser / separation losses will be noticeable [13]. This is especially true if the shroud is too short. It's important to note though that some studies, such as [11] and [21] found that adding a diffuser had negligible impact.

With this in mind, the area ratio was chosen to be approximately 1.25 – with an inlet propeller diameter of 5" and a diffuser of 5.57". This ratio was chosen based on previous experiments executed by different organizations (United Aircraft Corporation, NACA). For instance, Donald M. Black from United Aircraft Corporation found that for the shrouds their study tested, a ratio of 1.3 was the highest achievable area ratio. In this particular study, it was found between area ratios of 1.2 and 1.3, the thrust output began to level off due to diffuser losses, as shown in Figure 3.6. It should be mentioned that a shroud with an area ratio of 1.4 and a longer chord length was successfully tested as part of another test program [13]. It was decided to proceed with the 1.25 ratio and iterate this parameter only if diffusion / separation issues presented themselves.

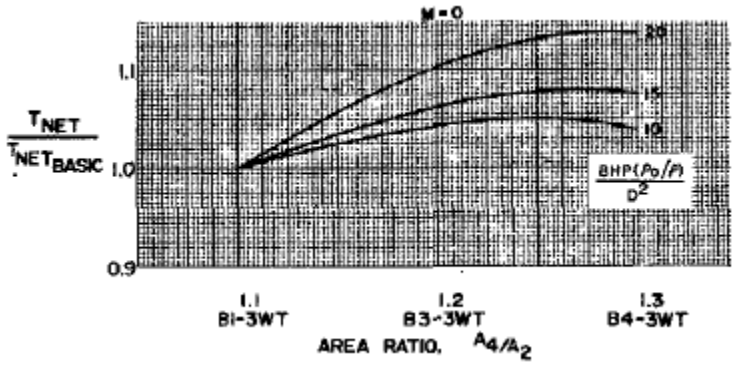

Figure 3.6. The influence of area ratio on static thrust output [13]. Between an area ratio of 1.2 and 1.3, the performance increase begins to taper off. Reprinted with permission of the American Institute of Aeronautics and Astronautics.

With the area ratio / inlet and exit diameters chosen, the next step was to decide on the cross sectional profile of the shroud. This step was critical, and required several iterations. Designing the cross sectional profile consisted of designing the lip shape (elliptical cambered as

compared to toroid shaped), determining the overall shroud length, and determining the diffusor profile (elliptical vs constant angle) and diffusion angle. All of these parameters are critical, as improperly designing them could result in flow separation. Propeller features such as tip clearance and solidity are also of concern. These requirements are presented in a morphological matrix identified as Table 3.1.

Table 3.1. A morphological matrix used to design the shroud.

Sub-Functions	**Solutions**			
Prevent Inlet Separation	Toroid lip	Elliptical cambered lip		
Prevent Stream Contraction	Shroud length			
Increase Thrust	Propeller solidity / geometry	Elliptical diffuser	Constant angle diffuser	Tip clearance

The shroud lip is arguably one of the most important parameters. In essence, one must be careful to design the lip so that the radial forces exerted on the incoming flow do not cause separation. The design of the inlet lip is a function of the air inlet velocity and radius. In other words, it would be beneficial to design the lip inlet curvature radius to be large [18]. In addition, it would be beneficial to minimize the rate of curvature. This can be achieved by using an elliptical-like inlet or perhaps a toroid shaped inlet.

Several iterations consisted of using toroid-shaped lips were designed at first, with the principal idea being to increase the radius of curvature, as shown in Figure 3.7. Due to the limited amount of volume the shrouds could take up, and the limited amount of weight, the shrouds with toroid-shaped lips were eventually discarded in favor of trying to achieve a cambered elliptical design. These design considerations are shown in a concept selection matrix, identified as Table 3.2. The concept selection matrix weights each of the parameters discussed (weight, increasing thrust, and usable propeller disc area) and sums these weights in attempt to ascertain the design to proceed to manufacture. The weights are representative of the relative importance of each requirement. In particular, increasing static thrust was determined to be the most important goal as this is the crux as to why the shrouded propellers were chosen over free propellers. Usable propeller disc area was assigned the next largest weight, as the minimizing this will limit the static thrust. Even though the mass of the shroud is a requirement, this was assigned the smallest weight as the other two tabulated objectives influence the static thrust generated.

Scores were generated based on physical properties of the designed shrouds and normalized. Several preliminary designs consisting of elliptical cambered and toroid shaped lips were solid modeled utilizing the constraints discussed above. Of these preliminary designs, the traditional toroid-shaped lip itself was about 40% to 50% heavier than the elliptical cambered lip (.13lb vs .09lb). This was primarily due to the large radius of the lip. In addition, the larger radius resulted in a smaller usable propeller disc area (which would practically influence how large the diffuser could be due to potential losses generated in the diffuser). For the same outer diameter, it was thought that the toroid-shaped lips would constrain the usable propeller diameter. Several preliminary designs again demonstrated this, with the toroid-shaped lips constraining the propeller disc area to 70% to 80% of that of the elliptical cambered lips. Finally, separation was scored. This was probably the most difficult criteria to score without the aid of physical models and aerodynamic testing. To score this objective, the data collected in [21] was used. In [21], several different configurations of toroid-shaped lips and elliptical cambered lips were examined in terms of lift coefficients, pitching moments, etc as functions of various angles of attack and advance ratios. Data from [21] indicates that at low advance ratios, the shrouds with toroid-shaped lips generated about 10% more thrust than their elliptical counterparts. It's important to stress that the scores in the concept selection matrix were generated with preliminary designs and aerodynamic data collected from other sources. It's possible that a lip design could be optimized using experimental methods of which may differ from the outcome of the selection matrix.

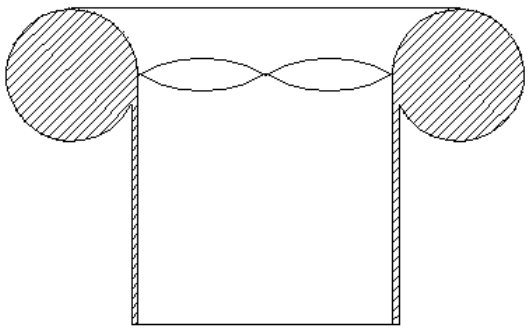

Figure 3.7. A generic shroud with a toroid lip design. While toroid-shaped lips can generate more thrust, they are often large, weigh more. In addition, according to [21] , they are more difficult to control due to the adverse pitching moment when used in aircraft.

Table 3.2. Concept selection matrix of lip choices. The toroid and elliptical cambered lip are compared.

		Toroid Lip		**Elliptical Cambered Lip**	
Objectives	***Weight (%)***	***Score***	***WS***	***Score***	***WS***
Weight	20%	.5	.1	1	.2
Increase Static Thrust Output	50%	1	.5	.9	.45
Usable Propeller Disc Area	30%	.7	.21	1	.3
Total	*100%*	*.81*		*.95*	

Ultimately, the shroud designed shown in Figure 3.8 ended up being 3.94" long (chord length) with an elliptical lip design (modified but based on the leading edge of the NACA 4421 airfoil) and an elliptical diffuser (approximated by a diffusion angle of about 9 degrees) per the morphological matrix previously identified as Table 3.1. Seeing as many shroud lengths are approximately 50% of their propeller diameter [13], this shroud is considered to be quite long. However, given the fairly large area ratio of 1.25, it was decided to be conservative and produce a shroud longer than it perhaps needs to be (with the tradeoff of increasing drag). Note that most researchers found that shroud length for static thrust conditions often did not have a large influence, unless the shroud was excessively short for the diffusion angle [11]. In addition, it was hoped that by designing a longer shroud, the tapering-off phenomenon in Figure 3.6 would be less.

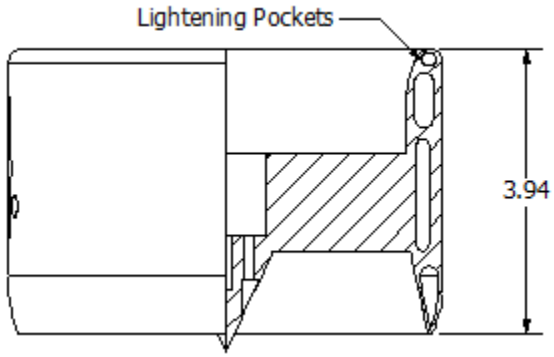

Figure 3.8. The first prototype shroud design. Lip, diffuser, and cross sectional geometry is revealed in this figure. In addition, the motor placement, centerbody, and stators are all visible.

In addition to the cross sectional shroud wall geometry, Figure 3.8 reveals the entire cross sectional construction of the first prototype shroud that was tested. One of the first things to notice is probably the hollow lightening pockets used in the wall cross section. This was done to lighten the structure up considerably. This would normally be a manufacturing challenge as it would perhaps require multiple pieces and molding / casting processes. However, it was decided it would be easiest to fabricate the structure using an FDM rapid prototyping machine (printing an ABS-like polymer). Using this machine, the shroud could be manufactured as a single part. In addition, it would be easy for this machine to manufacture the lip / diffuser geometry (as opposed to conventionally machining it, involving a multiple component assembly, tooling, fixtures, and machine processes).

In addition to the lightening pockets, Figure 3.8 also illustrates the stator position and chord length as well as the motor mount. The stators were designed to be a symmetrical and constant chord in nature, with their principal purpose to support the motor and provide rigidity to the structure. Stators can also be used to recover some of the thrust due to the propeller swirl, if the angle of incidence is correct [21]. With the relatively low power consumption and thrust that these shrouds would be generating, the angle of incidence of the stators was thought to be rather small. After considering the theoretical results and the manufacturing implications, the stators were designed to run parallel to the direction of axial flow. Figure 3.9 illustrates a solid model of the first prototype shroud, and Figure 3.10 is a picture of the actual shroud being manufactured.

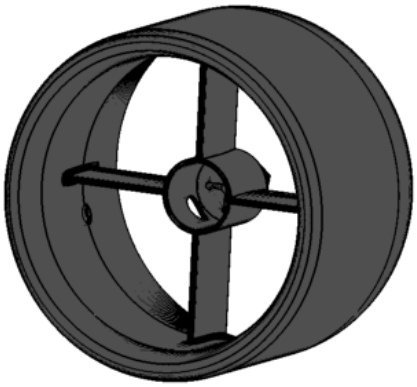

Figure 3.9. The first prototype shroud design as a solid model. This design was ultimately printed on a FDM rapid prototyping machine.

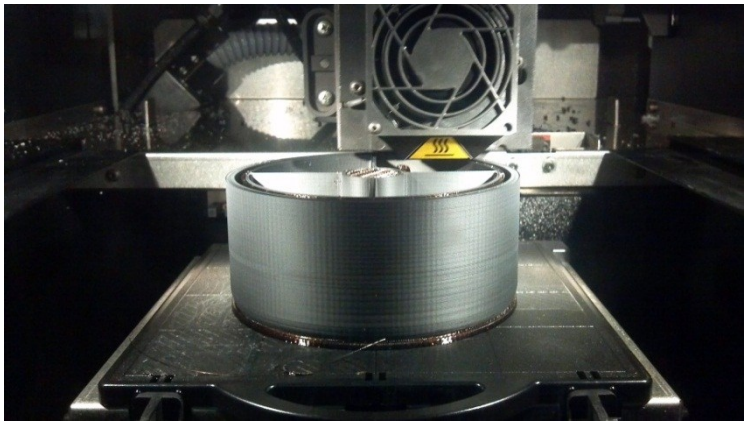

Figure 3.10. The first prototype shroud design being printed on a FDM rapid prototyping machine. The machine is operated by the Virginia Tech DREAMS Laboratory.

As stated earlier, individual propeller design was felt to be outside the scope of this thesis. Commercial propellers were instead bought and machined down to fit inside the shroud. Due to the relative constant chord and three blades (resulting in a higher solidity ratio), a Master Airscrew 3 bladed 8x6 propeller was machined down to an initial diameter of 4.98".

3.3.3 Initial Shrouded Propeller Testing

With the shrouded propeller designed, the next logical step was to manufacture and test it. In assembling the unit for testing, it was discovered that the diameter of the propeller was too large for the shroud. With the shroud being nominally 5" in diameter and the propeller being 4.98" diameter, the propeller was certainly expected to fit inside the shroud with a small tip clearance. Instead, it was found that the motor output shaft, and thus propeller were not perfectly concentric, causing the propeller blades to collide with a section of the shroud wall if ran. In addition to the shroud being not concentric, there were several other causes. These included the motor mounting surface was uneven and not perpendicular to the direction of flow, and of course, tolerances may not have been met by the FDM machine. The propeller ultimately had to be machined down an additional .040" (off the diameter) in order to fit in the shroud. This caused an uneven tip gap with the shroud.

Addressing this concern, the next step was to test the effectiveness of the shroud. This was measured in several ways. First, the shrouded propeller assembly was tested to ensure the flow field was staying attached and did not separate. Once this was confirmed, the shroud was tested for total static thrust output, and characterized as a function of power and PWM.

In order to make sure the flow was attached to the shroud walls, tufts were used to visualize the flow. As seen in Figure 3.11, the flow appears to be attached at both the lip and the diffuser for static thrust conditions. This indicates that the selected shroud geometry is working effectively. To illustrate what separation looks like, an obstruction was placed near the shroud inlet. The tufts during separation are shown in Figure 3.12.

Figure 3.11. Flow visualization - the flow field appears attached throughout the shroud. Left: The prototype shroud inlet with tufts attached. Right: The same shroud, with tufts attached to the rear at the diffuser. Separation does not appear to be an issue.

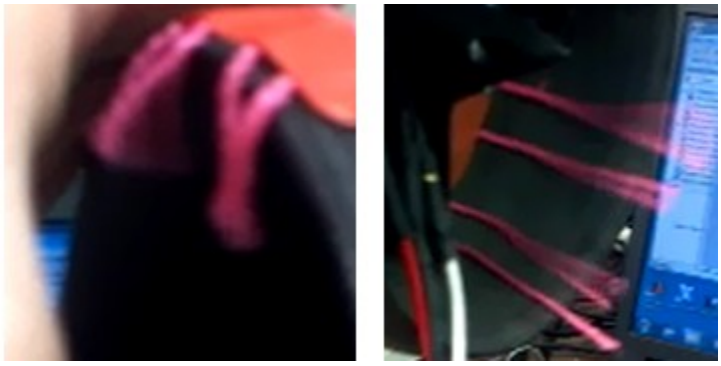

Figure 3.12. Separated flow field at the lip and diffuser. Notice the tufts are no longer streamlined, indicative of separation. The separated flow field was caused by an obstruction being placed at the inlet.

It is worth noting that the noise level increased substantially when the flow was separated. According to [12], shroud noise levels are indicative of the quality of flow attachment to the shroud walls. In essence, one should expect a poorly designed shroud to be loud due to the separation. Likewise, ensuring that the flow field remains attached will result in a quieter shroud.

In addition to testing for flow field attachment, an "L" shaped balance was constructed to measure the total thrust output of the shrouded propeller with a Honeywell Model 11 load cell. Thrust data was acquired using a National Instruments 9234 DAQ and a small custom written LabVIEW VI. Thrust data was collected as a function of rotation (RPM) and shaft power, and is presented in Figure 3.13. Power was provided and measured by an Agilent E3632A power supply. Rotational speed was adjusted by changing the duty cycle of the pulse width modulated signal to the electronic speed controller of the motor. The rotational speed was measured by a DT2234C digital laser tachometer. Notice that this shroud should meet both the thrust and power requirements as discussed earlier. The shroud consumes about 50W at 100% throttle, and produces .7lb of thrust.

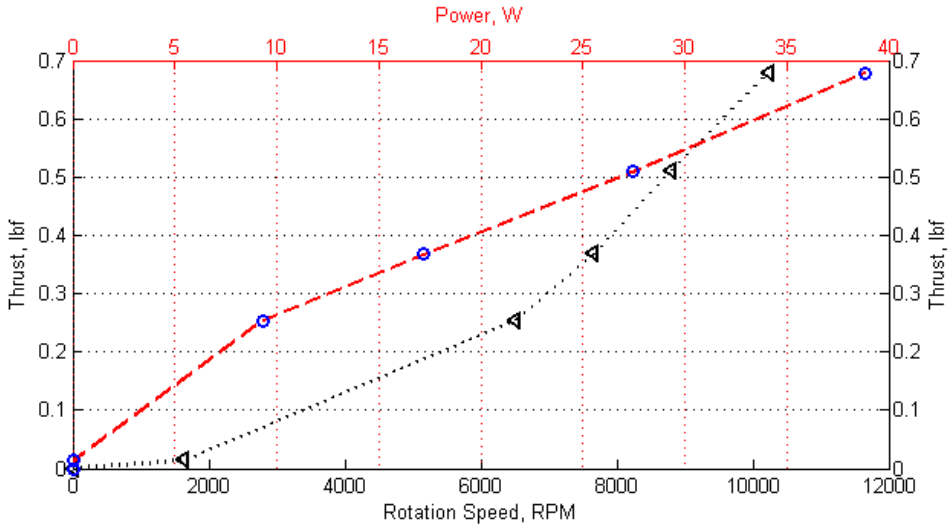

Figure 3.13. Static thrust as a function of power and rotational speed of the propeller. The power curve is shown in red while the rotational speed curve is shown in black. The trend observed is similar to the ideal trend as presented in Figure 3.4.

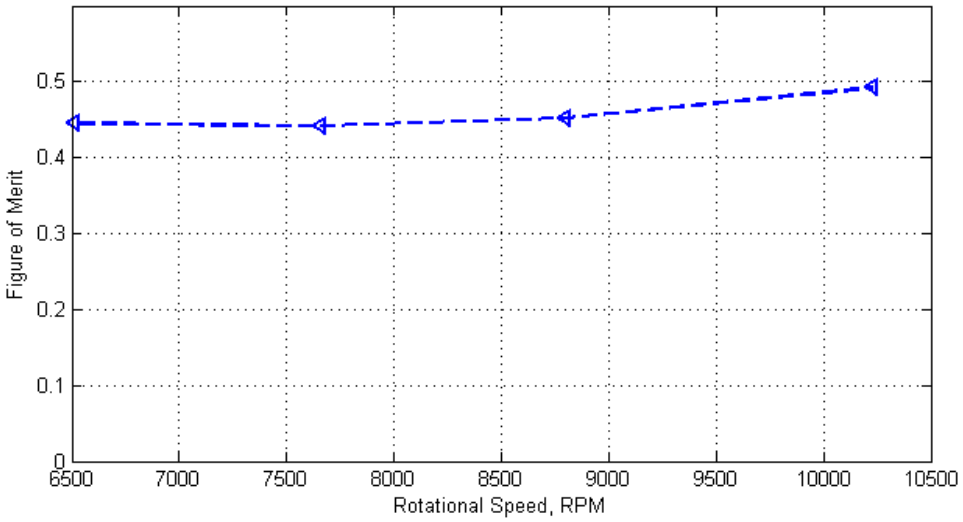

Figure 3.14. Figure of merit plotted as a function of rotational speed of the propeller.

In addition to plotting static thrust as a function of power and rotational speed of the propeller, the figure of merit, as defined in equation 3.4, was calculated and plotted in Figure 3.14. Broadly, the figure of merit is a measure of efficiency, and compares the actual power to induce the velocity through the propeller disc to the ideal power from momentum theory. It should not be expected to have relatively high figures of merit, seeing as the Reynolds number at 75% of the radius of the propeller is quite low at 50,000. This Reynolds number suggests that viscous drag will likely have a large impact on the performance.

$$M = \frac{T^{1.5}}{D_e P \sqrt{\pi \rho}} \tag{3.4}$$

These test results clearly indicate that the shrouded propeller designed will satisfy the design requirements listed earlier in this chapter. However, recall that the primary deficiency is the concentricity of the shroud, causing an excessive and uneven tip gap. To correct this, the design had to be refined.

3.3.4 Final Shrouded Propeller Design

The shrouded propeller from the previous section was redesigned primarily to compensate for the out of tolerance features resulting in a large tip gap. In essence, the same aerodynamic shape was preserved, but the design of the individual shroud components changed.

Unlike the shroud developed and presented in the previous section, it was decided to fabricate the new shroud in different sub-assemblies. For simplicity, three sub-assemblies were chosen – the shroud lip, the shroud center body, and the shroud diffuser. Due to the non-standard geometry of the lip and diffuser, it was decided to print these parts using the same FDM rapid prototyping machine. However, the center body needed to be fabricated out of something far stiffer and needed to be machined on a machine that could fabricate concentric parts. It was chosen to machine the center body (the motor mounts, stators, and shroud wall) out of 6061 Aluminum out of considerations for primarily rigidity and machine/manufacturability. Even though aluminum is relatively light weight for a metal, it is still significantly heavier per volume than the ABS plastic printed by the rapid prototyping machine (specific gravity of 2.65 for aluminum compared to 1.05 for the ABS plastic). Most of the shroud was printed in ABS, and the amount of aluminum comprising the shroud was kept to a minimum.

The resulting design illustrated in Figure 3.15, consisted of three sub-assemblies and eight individual parts. The shroud was designed to be approximately the same weight as the single piece ABS printed shroud (.83lbm, 15% over the ABS shroud). In order to match the weight of the full ABS shroud, some components could have been hollowed out. However, it was decided to match the material thicknesses, especially between the stators and the motor housing to make welding easier. In addition, the wall thickness of the center body ring was already extremely thin at .0625" nominal (especially considering its 5.00" inner diameter).

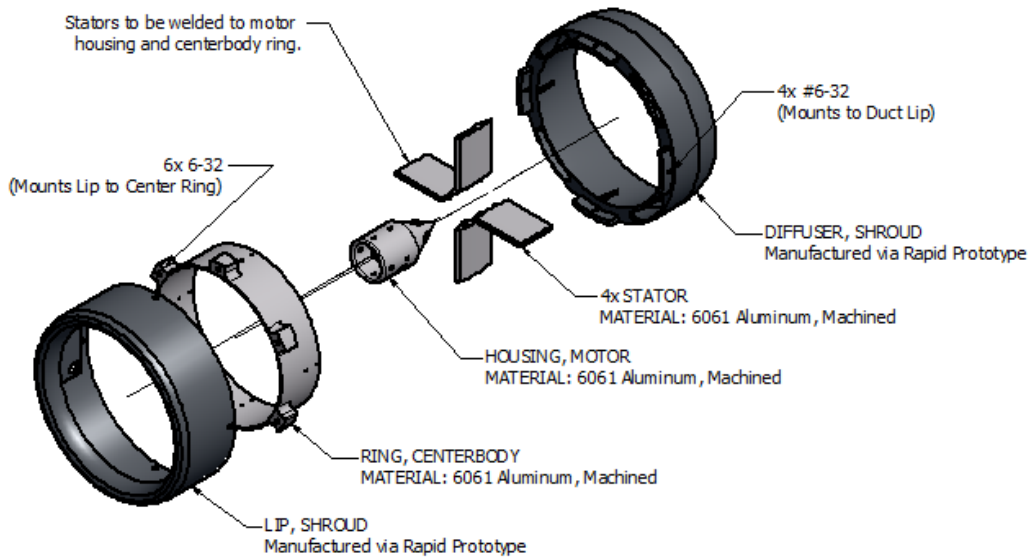

Figure 3.15. Revised shroud design, showing manufacturing and assembly methods.

A specialized fixture was machined to ensure that the stators, center body ring, and motor housing were placed in their proper respective planes and were as concentric as possible. Figure 3.16 shows the fixture with a shroud center assembly ready to be welded.

Figure 3.16. Shroud center assembly fixture, used to place the components in their proper plane and to ensure that they were concentric.

Three shrouds were ultimately fabricated, as shown in Figure 3.17. The reasoning behind fabricating three shrouds will be discussed in a later section, as it deals with controllability of the entire vehicle.

Figure 3.17. The three assembled shrouds used on the final assembly of the vehicle.

3.4 Final Shrouded Propeller Testing

The final step in the process of designing the propulsion system was to confirm that the shrouded propellers designed met the design requirements. Figure 3.18 below plots static thrust versus power and propeller rotational speed. The trends are similar to those presented in Figure

3.13, with the maximum static thrust of the final design roughly the same as the prototype design.

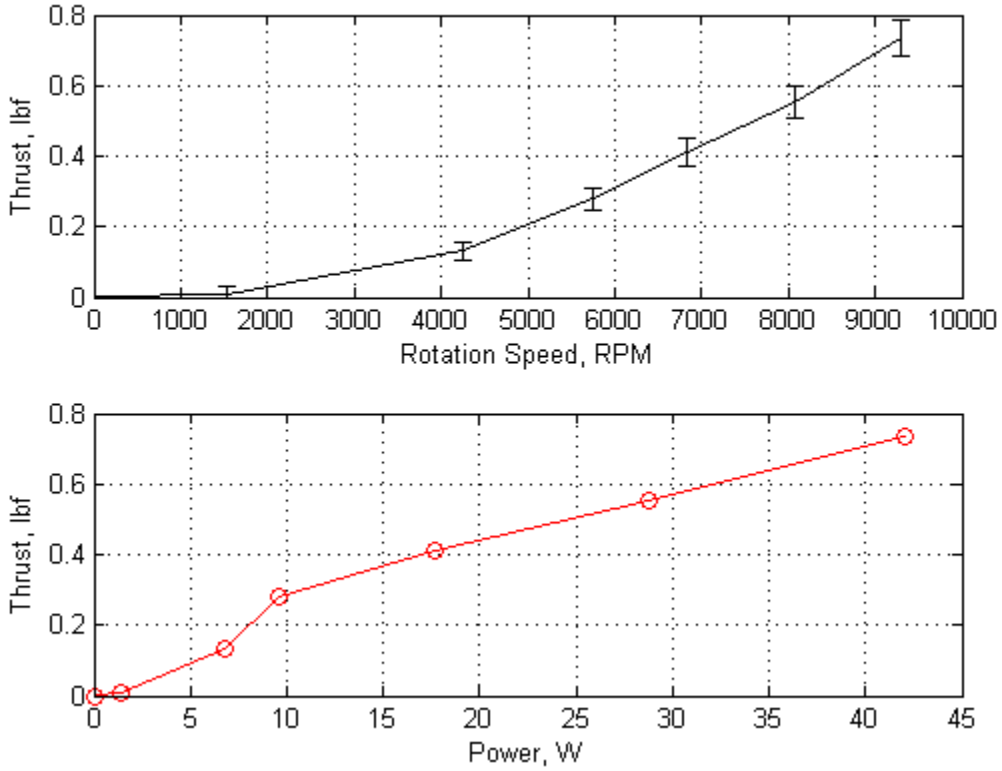

Figure 3.18. Static thrust as a function of power and rotational speed of the propeller. The error bars show two standard deviations.

With each shroud requiring about 43W of power at full throttle, the design power requirements are met. However, the design requirement of being able to produce 1.0lb of thrust is not met by using a single shroud. It is likely two shrouds will be needed to be able to produce 1.0lb to avoid wall / obstacle collisions. This isn't so much of a concern, as overall vehicle stability will require multiple thrusters / shrouds.

The final step in characterizing the shroud required a relationship to be developed between static thrust and the pulse width modulated signal duration. Electronic speed controllers control the RPM of the attached motor by receiving a pulse width modulated signal. The controller that was designed for this vehicle (presented in a later section) requires knowledge of this relationship. Figure 3.19 shows the relationship of static thrust as a function of the pulse width modulated signal duty cycle.

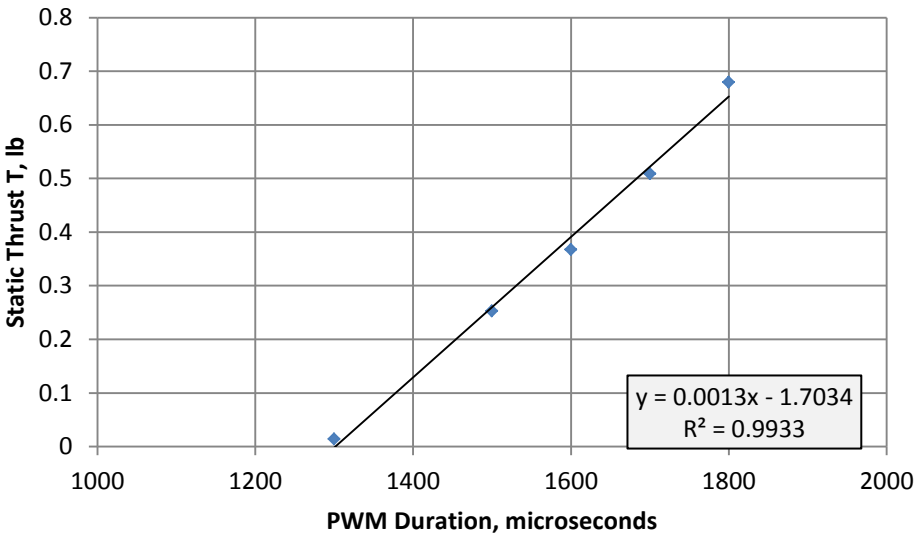

Figure 3.19. Static thrust as a function of PWM duty cycle in microseconds. This relationship will be used in the implementation of the vehicle controller.

With the shrouded propellers designed, tested, and characterized, the next step in designing the propulsion system was to marry the shrouds into the vehicle design. This would be done with consideration of the controller's performance, and as such, will be presented in a later section.

Chapter 4
Wall Detection

Designing a helicopter-deployable vehicle for supplying ground units requires many sub-systems. In particular, such a vehicle would need an environmental detection system to detect walls for the ultimate goal of avoiding collisions with the surrounding environment. In this particular case, the vehicle will use a Hokuyo URG-04LX scanning laser range finder unit for detection.

It's important to note that many different detection techniques could be used such as utilizing various vision algorithms / systems. However, many of these vision systems require a large amount of computational horsepower; provide too much information, or both. For this particular vehicle, the obstacles / walls at the vehicle's altitude are the only concern. This implies that the vehicle will only need a 2D point map (excluding height information). Utilizing an instrument that only collects 2D information will also decrease the computational requirements of the vehicle's onboard computer. The URG-04LX scanning laser range finder collects 2D information only, making it an ideal candidate in light of this discussion. This chapter discusses the design and implementation of the wall detection / tracking system utilizing the URG-04LX.

4.1 System Requirements

In addition to physical hardware to acquire the data, software is a necessity in the detection of walls and the surrounding environment. In order to have a reliable detection system, several requirements must be met.

- ***The detection algorithm must be able to report distance to and angle to the wall precisely.*** With the control scheme utilizing and controlling the distance and angle to a wall, excessive noise is an unacceptable issue. If the distance and angle measurements are noisy, the controller will likely be oscillating to compensate for dynamics that aren't really occurring. A filter will likely have to be used to compensate for some noise.
- ***The detection algorithm must be able to find a window.*** It is conceivable that a vehicle like this could be used in delivering supplies or extracting equipment / people / hardware. In addition, the vehicle could also be outfitted with specialized payloads for mission specific tasks. For example, imaging equipment could be outfitted on the vehicle for

surveillance missions in and around buildings. It is therefore the goal of the algorithm to be able to detect and identify a window.

- ***The speed of the system must be sufficiently fast for control.*** This is an extremely important requirement. Reliable control of a dynamic system often requires fast update rates. It is the hope therefore to achieve the fastest update rate possible by writing computationally efficient software, as the scan update rate of the URG-04LX used onboard the vehicle has an update rate that is fixed at 100ms [22].

4.2 Wall Detection Algorithm

This section of the chapter aims to go over the basic mechanics of the Hough transform, the mathematical principal in wall detection. In addition, the pseudo-code of the algorithm will be presented.

4.2.1 The Hough Transform

The Hokuyo URG-04LX is a scanning laser range finder, able to detect objects 4.1m away and is able to complete a sweep from -120° to 120° [22]. Each scan results in a set of *points* assigned a distance from the URG-04LX and an angle, as seen in Figure 4.1. In order to detect a wall among these points, software utilizing the Hough transform, a common line detection technique, was written.

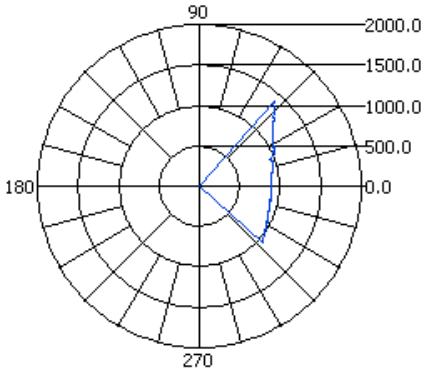

Figure 4.1. Sample output from the URG-04LX. There is a wall at approximately 800mm away.

The Hough transform is a technique used to determine if lines exist in datasets in a computationally friendly way. In essence, using the Hough transform, an X and Y dataset are converted into parametric space, which often results in characterizing the points as functions of radius R and angle θ. This is done for not only computational efficiency, but also to detect

vertical lines. For example, characterizing these points as functions of slope and the vertical axis intercept would lead to problems when a detected line is vertical. To find a common collinear line between these points, many lines are drawn through the point of interest by iterating θ a discrete amount in equation 4.1. The results (an angle and distance of a line drawn through each point) are stored in an array, typically referred to as an accumulator. The accumulator is then examined to look for a common distance R and angle θ within a specified tolerance. A voting scheme is used to analyze the accumulator array to "vote" for common distances and angles. If the number of votes exceeds a certain threshold, a line is claimed to be found [14].

$$R = x_i \cos(\theta) + y_i \sin(\theta) \tag{4.1}$$

To help visualize the mechanics of the Hough transform, a plot can be created relating line distance R to angle θ (typically referred to as the Hough space) of the data set. Figures 4.2 and 4.3 illustrate a sample data set and the Hough space of the sample data set. Figure 4.2 is a plot of a line consisting of seven data points with a slope of -1 and a vertical intercept of 1.

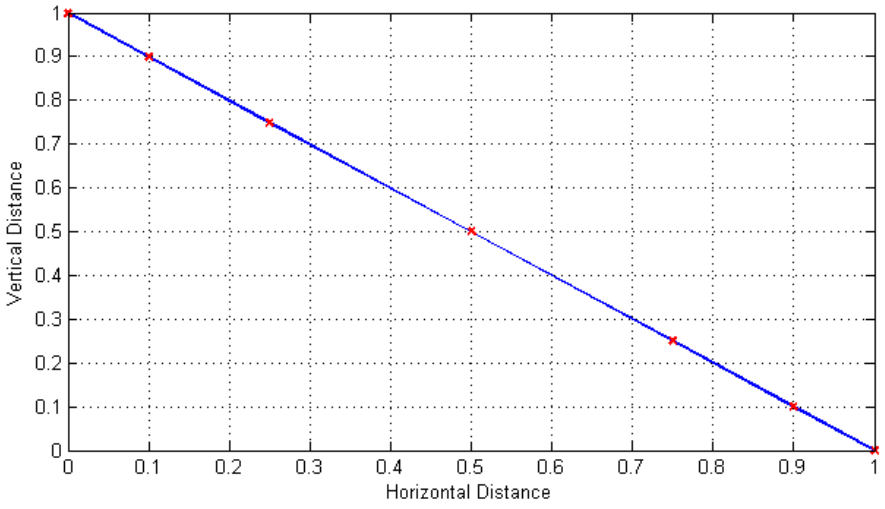

Figure 4.2. A sample data set having a slope of -1 and a y-intercept of 1. All of the sample data points reside along the line, which will be evident in the Hough space.

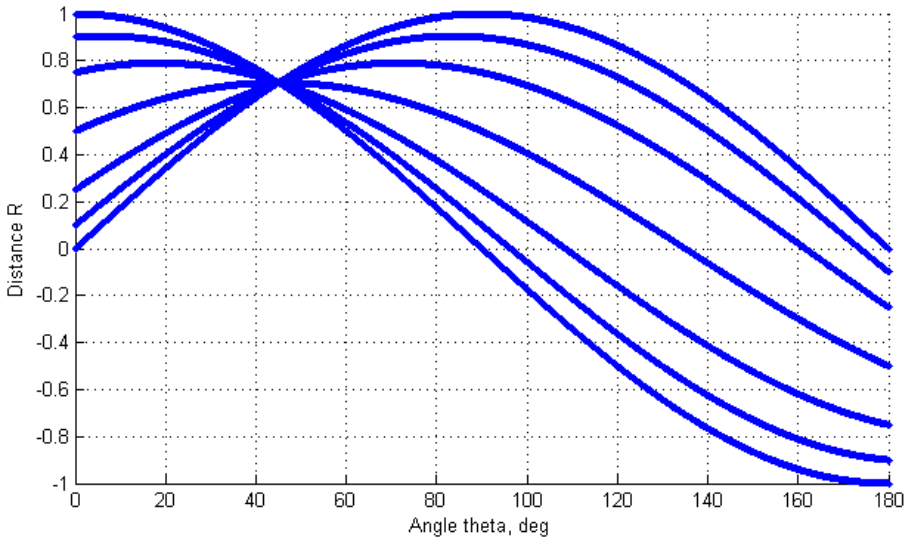

Figure 4.3. The Hough space of the sample data set presented in Figure 4.2. The distance from the origin and corresponding angle can be identified.

The Hough space is a plot of all of the interested distances (from the origin) as functions of angle of the "i^{th}" data point. If the points are collinear, the Hough space of the data set should converge to a particular distance R and angle θ. As shown in Figure 4.3, this is the case. With all of the points residing on the same line, it is quite evident that the distance from the line to the origin is about .71 while the angle is 45 degrees.

In a real world environment, the data set acquired from the Hokuyo laser range finder could potentially contain no walls, other obstacles, or multiple walls. Developing step sizes for the angle, range, and tolerances for the voting scheme are necessary to accurately detect a wall and the respective position. Improperly placed tolerances and step sizes can result in noisy data and incorrect identification of a wall. Since the controller will be using the data processed from the Hough transform to control its yaw angle and distance, the measurements must be relatively noise free and accurate.

4.2.2 Wall Detection Algorithm Pseudo-Code

The wall detection algorithm used in the development of the supply vehicle makes use of the Hough transform presented in the previous sub-section. The wall detection code was written in LabVIEW 2010 (to take advantage of the Hokuyo driver written for LabVIEW). Since LabVIEW is a data flow oriented language utilizing wires and block diagrams and is hard to

present, simplified pseudo-code which the developed code follows is presented below. The actual implementation is more intricate.

```
// Assemble Accumulator
for  i = 1 to NumberOfDataPoints
    for j = MinumAngleofInterest to MaxAngleofInterest by AngleStep
        AccumulatorArray(ArrayCounter,1) = j; // Angle
        AccumulatorArray(ArrayCounter,2) = MeasuredDistanceToPoint;
        ArrayCounter = ArrayCounter + 1;
    end
end

// Assemble Vote Matrix
for  i = 1:1:sizeOfAccumulatorArray
    VoteArray(Distance, Angle) = VoteArray(Distance, Angle) + 1;
end

// The maximum value of our vote is the best guess as to a wall in the
data set
for i = 0 to sizeofVoteArrayDim1
    for j = 0 to sizeofVoteArrayDim2
        if VoteArray(i,j) >= VotingThreshold
            FoundLineDistance = Resolution*i;
            FoundLineAngle = j*AngleStep;
        end
    end
end
```

4.2.3 Wall Detection Testing

Once coded, the next step was to implement the wall detection code and test it. This is critical for not only an accurate prediction of where the vehicle is its environment, but also for feeding the correct state measurement to the controller as well. If the noise is excessive, control may be difficult or impossible.

A simple test was executed to test the accuracy and scatter of the calculated wall distance and angle values. A wall was set up at a distance of 30in (.76m) away from the Hokuyo laser range finder at an angle of 25°. Data was taken for 30 seconds to examine the noise. The data is plotted in Figure 4.4.

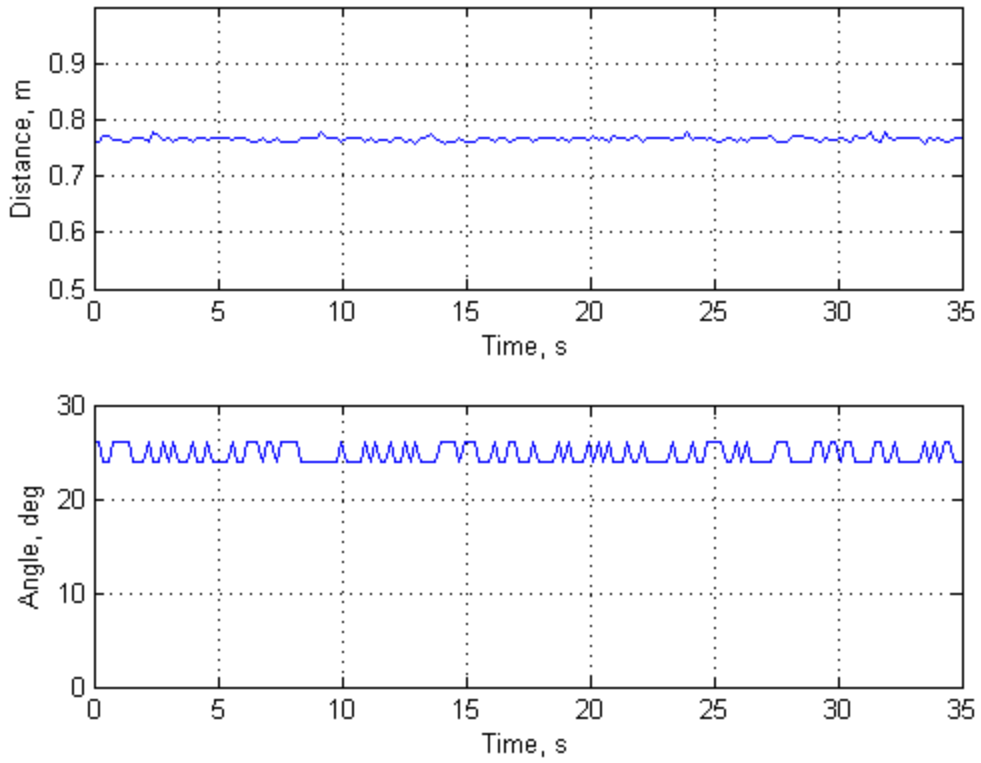

Figure 4.4. Sample record of distance and angle, calculated by the wall detection algorithm. The wall detection algorithm appears to detect the test wall at about .76m at an angle of 25°.

The results of the test plotted in Figure 4.4 indicate that the wall detection algorithm is able to successfully detect a wall at about .76m at an angle of 25°. Both subplots indicate there is some degree of noise to the measurement. However, with the algorithm detecting a wall at an average of .766m (.008m standard deviation) at 24.8° (.979° standard deviation), it shouldn't be an issue to the controller with a filter on it. It should be noted that the wall detection algorithm used an angular step size of 2° and a 4mm distance resolution. These numbers were chosen by iteration, with considerations mostly given towards computation time.

In addition to testing for functionality and noise, the performance of the actual implementation of the wall detection algorithm was measured. The start-to-finish iteration time was collected via LabVIEW's Performance Profiler for a few sample data sets. These results are displayed in Table 4.1. It is important to note that the time logged for each trial represents the start-to-finish runtime of the VI and therefore does *not* include acquisition times. This test was

run on an Advanced Digital Logic ADLS15PC PC/104 with a 1.6GHz Intel Atom and 1.00GB of RAM [23] (the computer that will be used onboard the vehicle).

Table 4.1. Wall finding algorithm runtimes. The loop iteration frequency was obtained by processing a constant set of data continuously. As such, it does not count for acquisition. This data was collected using LabVIEW's performance profiler.

Sweep Angle	Data Points	Frequency (Hz)
10	29	17.1
20	57	15.8
40	115	13.5
60	171	11.8
80	229	10.6
100	285	9.83
120	343	8.87
140	399	8.17
160	457	7.54
180	513	7.11
200	569	6.61
220	627	6.22
240	683	5.88

As will be discussed later, the controller is sensitive to sampling and update rates. As such, it is critical for data acquisition and processing to be completed as quickly as possible. Considering the limitations of the computational power available onboard the vehicle, the sweep range of the Hokuyo laser range finder will have to be limited to allow the controller to obtain accurate data quickly. Unfortunately, this will obviously limit the ability of the vehicle to be aware of its entire surroundings.

4.3 Window Detection Algorithm

In addition to detecting walls, it was also of interest to be able to detect windows as it may be possible to use the window as a dynamic state measurement for the vehicle. From an applications standpoint, the window detector can be used in conjunction with specialized payloads that can be carried by the vehicle. Such payloads may include a vision system that may aid in reconnaissance missions.

Window length and other relevant information cannot be gathered by the traditional Hough transform, as the Hough transform calculates a line of infinite length. An algorithm of

this nature can also be used to detect portals, the edges of walls, etc. This section of the chapter discusses how window detection / finite line detection was implemented.

4.3.1 Window Detection Algorithm and Pseudo-Code

Even though the Hough transform calculates a line infinitely long in length, the data set used to calculate the direction and distance of the wall / line is finite. To detect a window in the infinitely long line, the algorithm must first calculate the distance from each data point of interest to the found line (wall). Since it is expected that there will be noise in the data set, these points are compared to a distance threshold to determine if they actually represent the wall. If any of these points exceed the threshold, they most likely aren't part of the wall and might be a window. The indices of the first data point and last data point that do not exceed the distance threshold from the wall are then stored. Knowing these points, respective X and Y coordinates, the distance of the break in the line (possibly the assumed window) can be easily calculated. The break can then be compared to another threshold to determine if the break is indeed a window of typical size.

Like the wall detection algorithm, this algorithm was written in LabVIEW 2010. It is implemented as a subVI / function that will be called as part of the control routine. Pseudo-code of the basic algorithm is listed below.

```
% Throw away points that are far away from the found line
for i = 1:AmountofDataPoints
    if DistanceFromPointToFoundLine < ThresholdLine
        DistanceFromLine(i) = CalculatedDistanceFromLine;
    else
        DistanceFromLine(i) = 0;
    end
end

% Calculate the distance between
for i = 1:AmountofDataPoints
    if DistanceFromLine(i) >0
        DistanceBetweenPoints(i) = Distance_i_to_iinc1
    end
end
```

4.3.2 Window Detection Testing

With the window detection algorithm coded, the next step was to quantify its performance by testing it. The window detection algorithm was tested by placing a "window" in

the wall measuring 18.25 in (.464 m) across. To see if the measurement and calculation contain significant noise, the calculated window width over time is plotted in Figure 4.5.

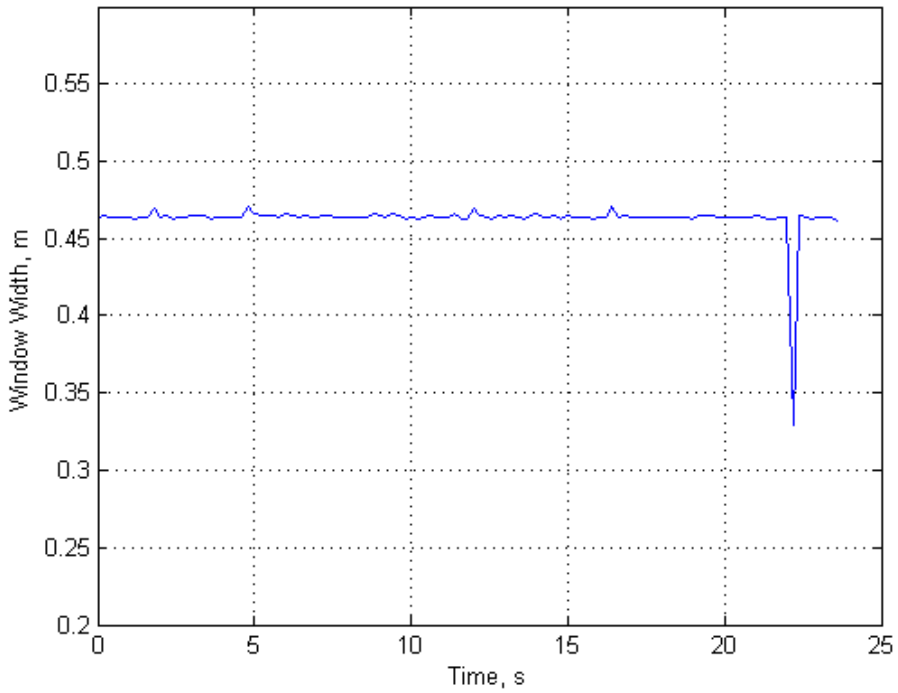

Figure 4.5. Sample record of detected window width. The window detection algorithm successfully detected a window at about .463m. One extreme outlier is shown in this data set.

As seen in Figure 4.5, the window detection algorithm detected a break / window in the test wall. The average window width of the time of the sample was .463m with a standard deviation of .0125m. This agrees with the test setup of 18.25in (.464m). It should be noted that the window detection algorithm was tested with 171 data points and executed in a negligible 1.2ms. While this figure does not include acquisition time, it does include the time it takes to draw and update the indicators and controls on the VI. Since this will be executed as a SubVI in most situations, the execution time will be far less – on the order of .17ms.

Chapter 5
Tethered Supply Vehicle Design

With the subassemblies / systems designed, the next step was to incorporate all of these subsystems into a single, controllable, tethered vehicle. This chapter discusses the design decisions and process of the tethered resupply vehicle.

5.1 Vehicle Requirements

Before the assembly was modeled and designed, the requirements of the vehicle needed to be identified. They are:

- ***The vehicle must meet weight restrictions.*** A typical 100kg class helicopter, like one that may be used in the proposed resupply scenario will realistically will have approximately 10kg worth of payload capacity before exceeding its allowable gross weight. It is desired to budget at least half of this 10kg payload capacity for the hypothetical supplies, with the other 5kg budgeted for the vehicle itself. It is therefore desired to design a vehicle weighing 5kg or less.
- ***The vehicle must meet the geometric constraints of the USL developed winch.*** The USL developed winching system is designed to be attached to the Yamaha RMAX helicopter flown by the lab. Originally designed to deploy a ground sampling / collection robot, it is desired to use the winch for the deployment of other tethered vehicles such as this one. To use the currently designed winch system, the vehicle must first be able to fit in the confined space under the helicopter. This volume measures approximately 19”x19”x9”.
- ***The vehicle must carry computing power and all necessary sensors onboard.*** The main goal of this vehicle is to be able to deliver supplies precisely where needed. In addition, it is desired to be able to use the sensor data collected by the vehicle to avoid obstacles if need be. Simply being tethered to the helicopter, it is desired to do all processing onboard if possible for control. Likewise, sensors will need to be onboard the vehicle as well to provide dynamic measurements (yaw, yaw rate, velocity, etc). In addition, a LIDAR / laser range finder will need to be placed

onboard the vehicle to collect information about walls, windows, and potential obstacles.

- ***The vehicle must be controllable.*** Perhaps the most important practical requirement, the vehicle must be able to control itself using a feedback loop. This directly dictates the vehicle design as thruster placements, the center of mass, the rotation point, etc all govern the dynamics of the vehicle that must be controlled. For example, since the vehicle must be able to rotate under its own power (let's say to follow a wall), the thrusters must be positioned to generate a torque. In addition, since it is desired to have .1g of horizontal acceleration to avoid a wall, the thrusters must be positioned to generate enough thrust. It is for these reasons that some of the basic controller design must be developed along with to design the vehicle.
- ***The vehicle must be able to carry a small payload.*** This requirement is one of the primary goals of designing this vehicle – to be able to deliver a *payload* to a precise location. However, considering that the vehicle will need to have thrusters, a computer and other instrumentation, and is limited by the geometric constraints of the Yamaha RMAX and winch system, there is a very limited amount of area for a payload. It is desired to maximize the amount of area available to secure supplies to the vehicle.
- ***The vehicle's structure must be able to support a payload and all of the sub systems.*** With 5kg worth of payload and the vehicle itself weighing 5kg, the vehicle must be able to adequately support the payload carried by it and all sensors / mechanical equipment. Excessive deflection and inadequate stiffness could potentially cause problems with the controller, having to account for additional dynamics.
- ***The vehicle must be able to operate in a GPS denied environment.*** One of the proposed mission scenarios of this vehicle is to be able to deliver supplies in an urban area. While GPS (Global Positioning System) satellite signals are often times receivable and many GPS units function in an urban area (such as the commercially available units to provide driving directions), position and velocity accuracy can significantly degrade. It is for this reason that it is desired to not rely on any of the position or velocity states of the vehicle by GPS.

5.2 Vehicle Electronics and System Architecture

In order to meet the previously developed requirements and goals, the vehicle will need to have several sensors, microcontrollers, etc. This section of the chapter details the electronic hardware and how all of the systems were bridged together.

5.2.1 Navigational System

As previously detailed in chapter 4 of this thesis, a Hokuyo laser range finder (URG-04LX) was used to detect walls along the vehicle's path. Even though the perpendicular distance to the wall and the respective angle are important measurements and states to have, they alone are not sufficient. Translational and rotational position and velocity information are also required. This information can be gained in several ways – one, by an inertial measurement unit, and two, some position and velocity information can be provided by a GPS. However, per the requirements listed in the previous section of this chapter, outfitting the vehicle with a GPS is not permitted. Measuring and calculating these states therefore requires an IMU on the vehicle.

A MicroStrain 3DM-GX2, pictured in Figure 5.1, was selected for use as an onboard IMU. This particular unit is capable of outputting accelerations in the X, Y, and Z direction (and the integrated velocities). In addition, it is also capable of outputting yaw, pitch, roll, and all of their respective rates. This IMU communicates via RS232 at 115.2kbps and is capable of providing updates at 250Hz [24].

Figure 5.1. A picture of the MicoStrain 3DM-GX2 IMU. This unit will be mounted onboard the supply vehicle to gather the dynamic states of the vehicle.

5.2.2 Vehicle Onboard Computer

As briefly stated in Chapter 4, the tethered supply vehicle was outfitted with an Advanced Digital Logic ADLS15PC PC104 computer. This computer has a 1.6GHz Intel Atom

processor with 1.00GB of RAM [23]. In addition, this computer was outfitted with a solid state hard drive.

The ADLS15PC PC104 was selected for two primary reasons. First, the computer is capable of running Microsoft Windows on it. Second, the URG-04LX laser range finder is easy to communicate with using LabVIEW (installed on Windows) as the acquisition SubVIs were already written by Hokuyo. The disadvantage to this approach is that Windows is not a real-time operating system, and as such, running a program at a specific desired rate may be difficult.

The ADLS15PC PC104 pictured in Figure 5.2 is relatively small. The board measures about 4" x 3.5". This does not include the power supply board, which is also similar in size. However, the bus pins are rather long, which will probably require the computer housing / case to have a significant height. This computer features two serial ports and more than eight USB ports, which is more than enough for the acquisition needs of this vehicle.

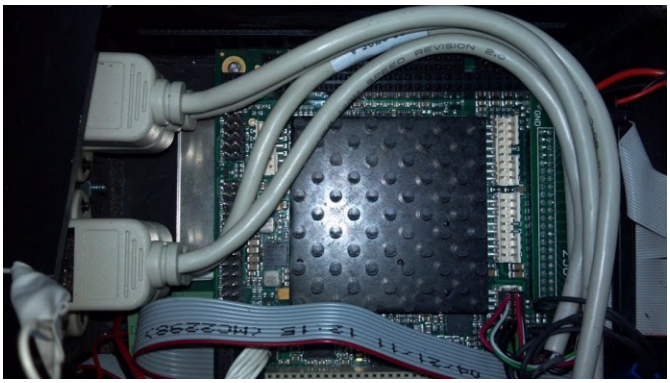

Figure 5.2. A picture of the ADLS15PC PC104. This picture does not feature the power supply board.

5.2.3 Propulsion System Electronics

Even though the propulsion system hardware was designed at selected at this point (Chapter 3), the electronic hardware to control the motors and communicate to the onboard computer had not been selected. In chapter 3, Hacker out runner motors were selected. These motors are typically controlled with electronic speed controllers, such as the Castle 25 selected and used. However, these electronic speed controllers are normally used with small-scale hobby aircraft receivers. As such, these controllers control the speed of the motor by receiving a pulse width modulated input signal. In order to send a digital signal to the electronic speed controller, a small microcontroller is necessary (the ADLS15PC PC104 does not have any digital input or

output pins). An Arduino MEGA (shown in Figure 5.3) utilizing the ATmega1280 was selected to provide this functionality. Selection was primarily based on the hardware available in the lab as this board has 14 PWM outputs, far more than is required.

Figure 5.3. A picture of the Arduino MEGA. The Arduino MEGA was selected to provide a pulse width modulated signal to the electronic speed controllers.

5.2.4 Wireless Communication

It is necessity to be able to communicate with the tethered supply vehicle to perform a variety of functions (turn the controller on/off, to identify windows, for debugging, etc). Seeing as the vehicle is tethered and self-powered, a wireless communication method is necessary. An 802.11n external USB wireless card was used to provide this functionality.

5.2.5 System Architecture Overview

With a variety of sensors and subsystems onboard the tethered supply vehicle identified, the next step was to ensure all of them functioned reliably in concert. In order to achieve this requirement, the first step was to identify how all of the subsystems and instrumentation would communicate. This is shown in Figure 5.4 - a block diagram of the entire vehicle's architecture.

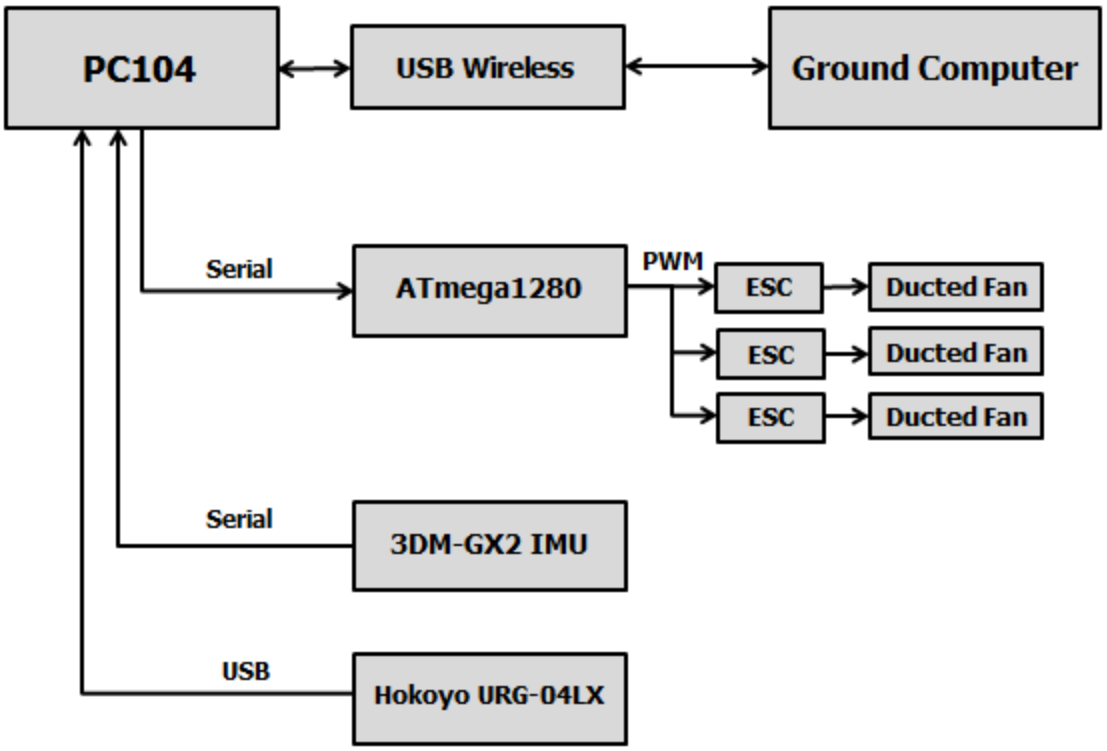

Figure 5.4. Block diagram of the system architecture. Note that the arrows show the primary direction of the flow of data.

As seen from the block diagram in Figure 5.4, the PC104 is used to collect data from the IMU by serial and the laser range finder (USB). The PC104 is then able to determine the dynamic state of the vehicle (position from the wall, velocity, angle from the wall, angular rate, etc) by executing the Hough transform / wall detection algorithm. Using a control loop executed on the PC104, a serial message to the ATmega1280 with regard to the length of the pulse width modulated signal needed to achieve a particular thrust (relationship shown in Figure 3.19). The custom written program on the Arduino outputted PWM signals that were received by the electronic speed controllers. Once the signal was received, the ESCs adjusted the rotational speed, and thus thrust output, of the shrouded propellers / ducted fans. The ground computer (could perhaps also be a computer onboard the helicopter) is able to turn on and off the control algorithm and issue other open-loop commands via the 802.11n wireless adapter onboard.

Most of the executable code on the PC104 was written in LabVIEW 2010. While other languages are certainly faster, LabVIEW 2010 was chosen to take advantage of Hokuyo's pre-

written driver to acquire data from the URG-04LX. Code was also written for the ATmega1280 using a C variant published by Arduino.

Since the vehicle is going to be self-powered and contained, it is important to get a sense of the total power consumption to properly size the batteries. With the motors turned off and the vehicle running just the computer and all sensors, the total power consumption was measured to be 20.8W. With each motor running at full throttle and all systems powered up, the total power consumption of the vehicle was measured at 170W.

5.3 Design and Implementation of Software User Interface

Custom software was written and implemented on the PC104 onboard the tethered supply vehicle. This software ultimately collected the laser range finder data, IMU data, communicated to the ATmega1280, and provided a remote desktop connection for the ground computer. Figure 5.5 shows a screen shot to what the user would see. In normal operation, the user would simply select to turn on and off the controller. The IMU data, laser range finder data, etc, would then be updated every iteration of the control loop automatically. As seen in Figure 5.5, the program is also able to collect the IMU and laser range finder data manually, mostly for debugging purposes.

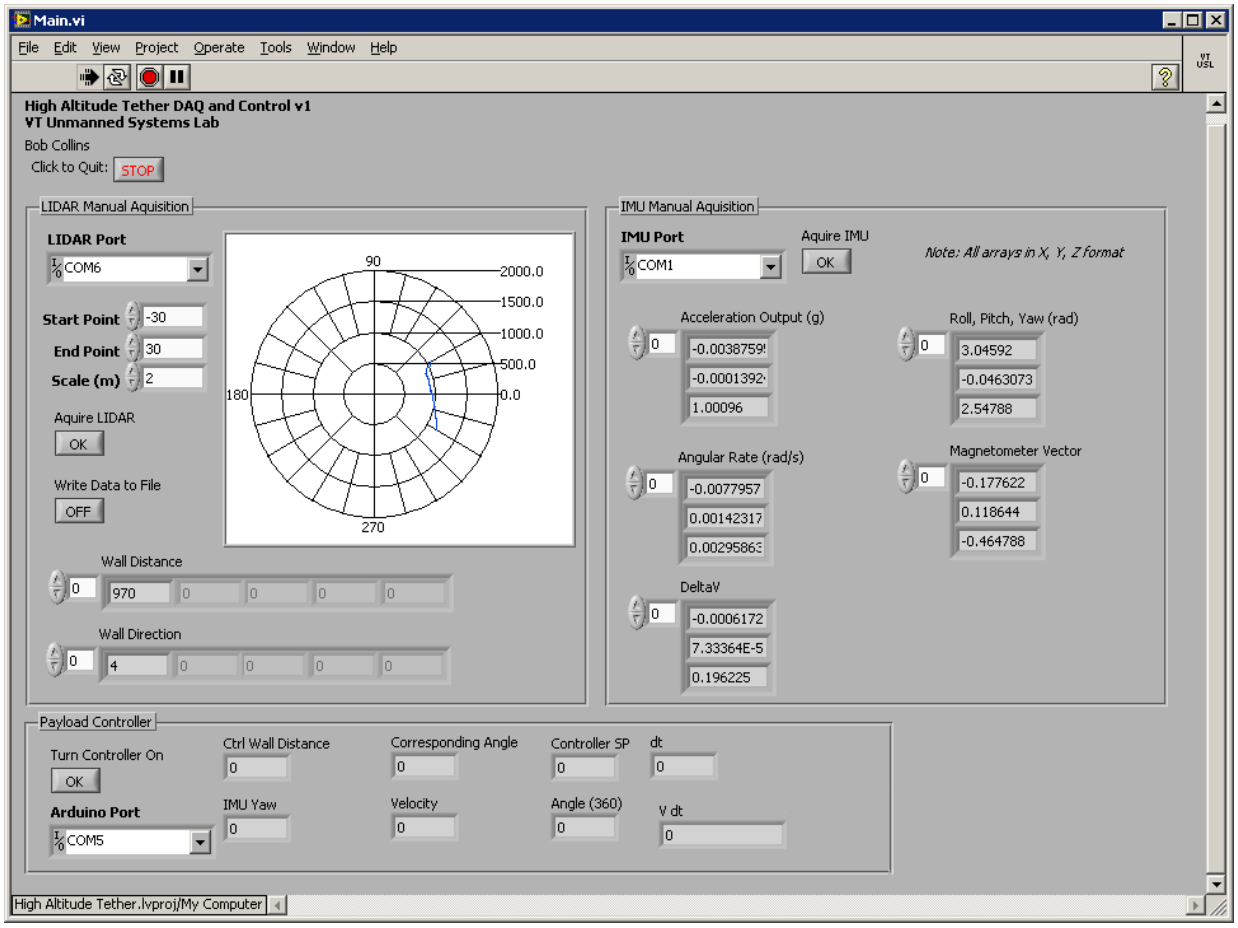

Figure 5.5. Screenshot of the user interface for the tethered supply vehicle. The user can view in real time the environment as acquired by the laser ranger finder, log states, and enable the controller.

The main screen shown in Figure 5.5 is the only LabVIEW VI the user will have to interact with on a normal basis. There are over twenty custom-written virtual instruments though, most of them acting as SubVIs to provide complete functionality.

5.4 Dynamic System Modeling

Before any mechanical design can be done, the requirement of controllability must be addressed. To address this issue, a simple dynamic model was constructed with a full state feedback controller. Simulations were executed iteratively; comparing settling time as the physical parameters of a vehicle platform were varied (thrust angles and positions, moment arms, etc). This section of the chapter discusses the dynamic system modeling used for the design of the tethered vehicle. A more in depth explanation of the dynamics will be given in the next chapter.

5.4.1 Equations of Motion

Before implementing a simple controller for design purposes, the equations of motion for an actuated tethered payload had to be derived. The hypothetical system was first analyzed by creating a generalized model of a hypothetical vehicle with arbitrary thruster positions and directions. The moment equation was derived by examining the vehicle from a top-down orientation as shown in Figure 5.6.

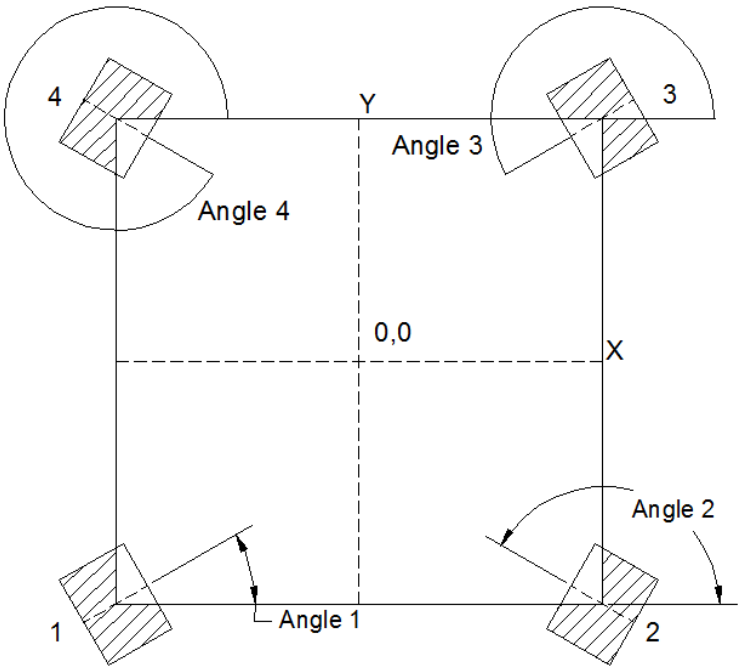

Figure 5.6. Diagram showing the generalized coordinates of the thrusters.

Using Figure 5.6, a generalized moment equation could be written in terms of four thrusters. Equation 5.1 was written using several key simplifying assumptions. Primarily, it was assumed that the center of mass was located in the center of the vehicle, which coincidently is the axis of rotation. Second, it was also assumed that the resultant forces from the tethered lines from the vehicle to the helicopter went through the axis of rotation, therefore not producing any net moments. Note that equation 5.1 lists each moment from the thrusters as positive. This is done only to express the equation in general terms – in actuality, there will need to be a negative moment generated for control.

$$J\ddot{\theta} = R_1T_1 + R_2T_2 + R_3T_3 + R_4T_4 - c\dot{\theta} \tag{5.1}$$

In addition to equation 5.1, an equation to relate the vehicle's position from the wall was necessary. Again, using Figure 5.6 and Figure 5.7, a force balance (equation 5.2) was written in terms of the thrusters and the mass of the vehicle. In addition to accounting for thrusters, small deflection linear pendulum dynamics were incorporated in the "x" direction. More detail on this derivation can be found in the next chapter.

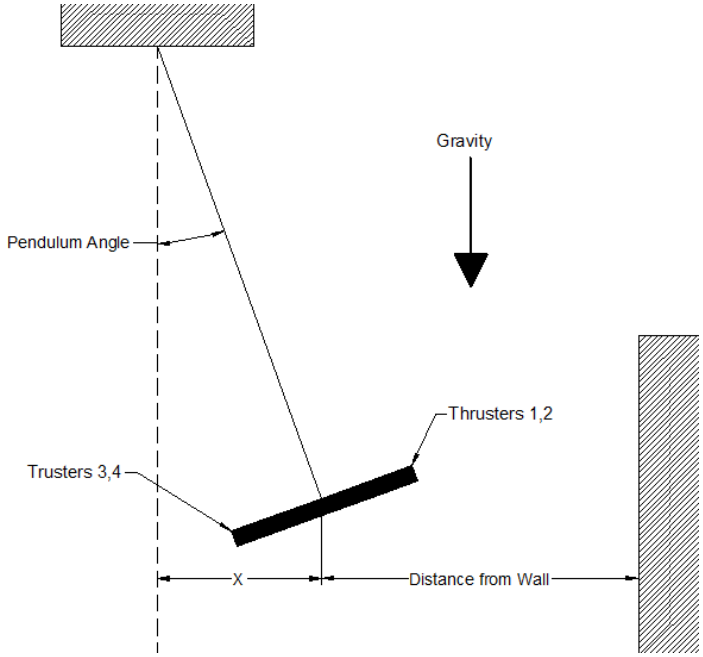

Figure 5.7. Diagram showing 2D pendulum motion.

$$m\ddot{x} = -T_1 \sin(\emptyset_1) - T_2 \sin(\emptyset_2) - T_3 \sin(\emptyset_3) - T_4 \sin(\emptyset_4) - \frac{mg}{L}x \tag{5.2}$$

With equations 5.1 and 5.2 derived, the perpendicular distance and angle from the wall could be controlled. These equations are reassembled into state space form as shown in equation 5.3.

$$\begin{bmatrix} \dot{\theta} \\ \ddot{\theta} \\ \dot{x} \\ \ddot{x} \end{bmatrix} = \begin{bmatrix} 0 & 1 & 0 & 0 \\ 0 & -\frac{c}{J} & 0 & 0 \\ 0 & 0 & 0 & 1 \\ 0 & 0 & -\frac{g}{L} & 0 \end{bmatrix} \begin{bmatrix} \theta \\ \dot{\theta} \\ x \\ \dot{x} \end{bmatrix} + \begin{bmatrix} 0 & 0 & 0 & 0 \\ \frac{R_1}{J} & \frac{R_2}{J} & \frac{R_3}{J} & \frac{R_4}{J} \\ 0 & 0 & 0 & 0 \\ \left(-\frac{\sin(\emptyset_1)}{m}\right) & \left(-\frac{\sin(\emptyset_2)}{m}\right) & \left(-\frac{\sin(\emptyset_3)}{m}\right) & \left(-\frac{\sin(\emptyset_4)}{m}\right) \end{bmatrix} \begin{bmatrix} T_1 \\ T_2 \\ T_3 \\ T_4 \end{bmatrix} \tag{5.3}$$

5.4.2. Thruster Placement for Controllability

With the equations of motion / equation 5.3 derived, it was possible to design a vehicle for controllability. First, a Simulink model was created utilizing the state space equation listed

equation 5.3 and a full state feedback controller, utilizing the control law $-\boldsymbol{Ku}$ in the feedback loop. Saturation limits were put in place to limit the actuation of the thrusters (shrouded propellers / ducted fans) between 0 and the top end limit of 3.3N. The Simulink model is shown in Figure 5.8.

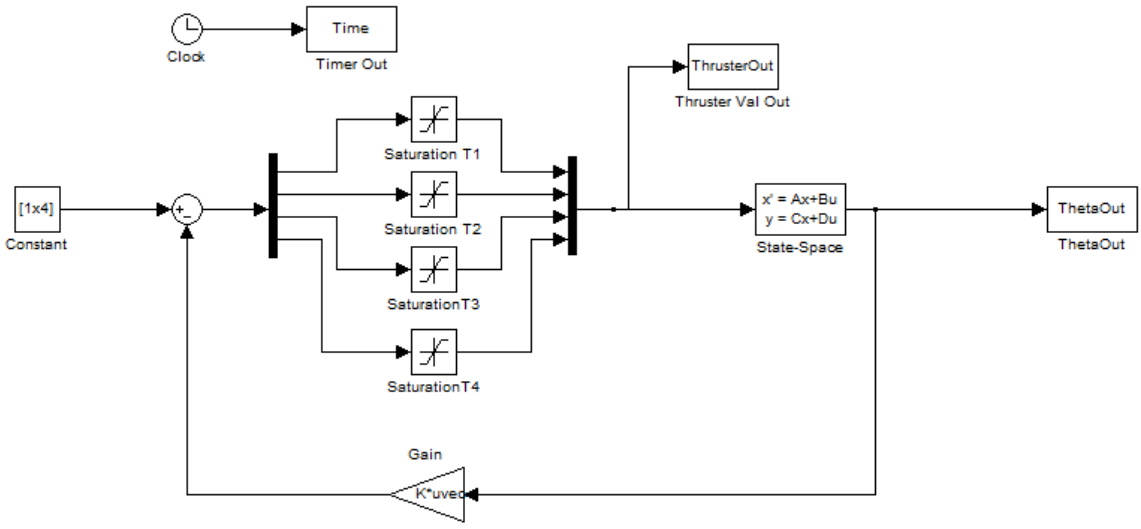

Figure 5.8. Original Simulink model used to design the vehicle for controllability.

Once the Simulink model shown in Figure 5.8 was created, a MATLAB code was written to utilize the model. This MATLAB code iterated the physical parameters of the vehicle for a given set of poles and initial conditions and logged the settling time (time it took for each state to reach 0 to within 2%). The calculated results from the MATLAB code had to be balanced with the requirements of the vehicle. For example, depending on the initial conditions of the vehicle, the MATLAB script may have optimized the thrusters to be in a position to minimize settling time turning in a particular direction, but leave the vehicle with little control authority if it needed to turn the opposite direction.

It was ultimately decided to design a tethered vehicle with a three-thruster arrangement. While a fourth thruster would arguably provide more control authority if oriented properly, it was decided to use a three-thruster arrangement to minimize weight. By sticking to three thrusters, the entire propulsion system would only contribute 2.97lb to the entire vehicle weight (less than the 4lb requirement discussed previously in Chapter 3). The thruster placement configuration chosen featured two fixed shrouds and one with a vectoring mechanism. The thrust vectoring shroud will allow the vehicle to output .1g in a direction. However, because a

linearized model was used (equations 5.1, 5.2), thrust vectoring was not incorporated in the current controller. It was decided to "lock" the vectoring mechanism at a particular angle for testing. The final design geometric parameters are shown in Table 5.1. These measurements are based off of the geometric parameters shown in Figure 5.6.

Table 5.1. Thruster placement parameters, **indicates thrust vectoring shroud.*

	Angular Placement, degrees	**Thrust Moment Arm, m**
Thruster 1	30	.0662
Thruster 2	120	-.0662
Thruster 3	250*	.0619

As a final check on the thruster placement, plots were made to observe thruster output for a given initial condition / disturbance. This was done to check if the thrusters were being driven particularly hard. While the actuation of the thrusters depends partially on the pole placement of the utilized controller (and therefore cause the thrusters to be driven hard), it could also indicate that the geometric placements of the thrusters are not ideal. A plot of the thruster / shroud actuations for a 10 degree yaw initial condition (the initial conditions were chosen so the linear approximation of the dynamics remained valid) is shown in Figure 5.9. Figure 5.9 is ordered sequentially with thruster one at the top, thruster two below thruster one, etc. Except for the initial desire to actuate at full throttle for thruster one, none of the thrusters saturate during the time of operation.

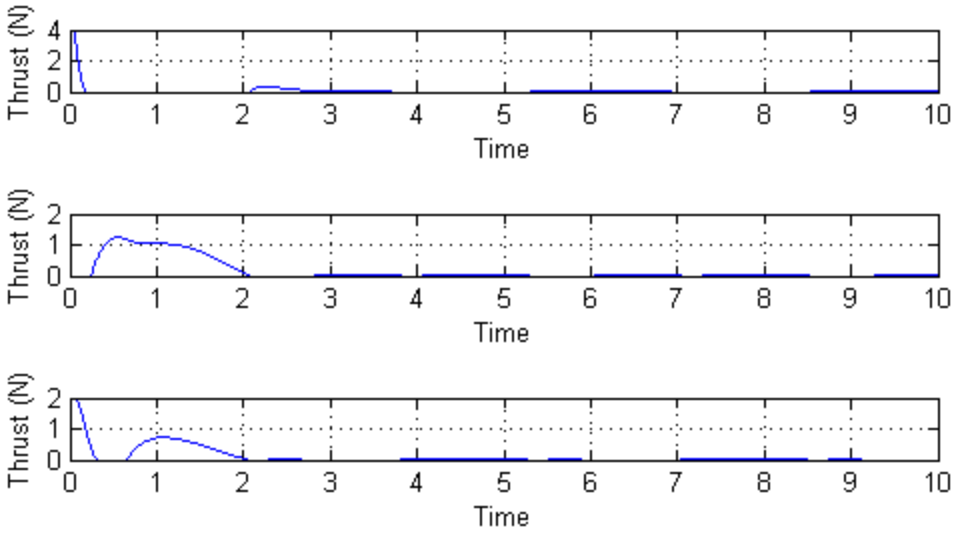

Figure 5.9. Simulated thruster output for a 10 degree yaw initial condition. In this case, the tethered vehicle is simply trying to rotate itself to be parallel with the detected wall. Except for thruster one at the start of the simulation, none of the thrusters are actuated to the maximum saturation limit.

5.5 Vehicle Mechanical Design

At this point, the system architecture was designed and thruster placement was chosen. The next step was to design the tethered vehicle to meet the requirements discussed in section 5.1 and to marry the subsystems together. This subsection discusses the mechanical design of the tethered vehicle.

5.5.1 Designing for Requirements

Several requirements listed in section 5.1 directly impact the mechanical design of the vehicle. For example, the weight requirement of the vehicle dictates the method of construction and material of choice. In addition, the geometric constraints imposed on the vehicle by the winch pod and sensors / electronics placement influence the overall shape and geometric features of the vehicle. Perhaps most importantly, the strength requirement influences just about every aspect of the vehicle and directly competes with the other requirements.

In order to address the geometric constraints of the vehicle, the previously-developed USL winch pod must be considered. A solid model of the winch pod with the Yamaha RMAX landing gear is shown in Figure 5.10. Note that the winch pod payload area is square in nature, with the supporting legs converging to the electronics mounting surface area of the vehicle. To

maximize the usage area of a vehicle, it was decided to design the vehicle to be of a square planform area. Because the supporting legs converge to the electronics mounting surface area, the length and width were limited to 16”x16”.

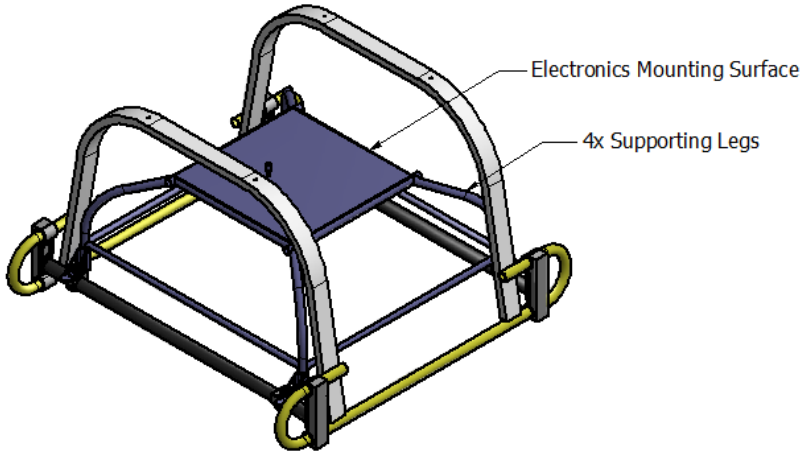

Figure 5.10. Yamaha RMAX landing gear with the USL developed winch pod attached. The tethered vehicle was designed to fit in the underside volume.

With the overall shape and dimensions of the vehicle decided, the next step was to address the vehicle’s weight. To maximize the useful load of the vehicle and helicopter, the weight of the vehicle needed to be kept to a minimum. It was decided to fabricate the structure of the vehicle out of components constructed from 6061 aluminum sheet, .030” thick and to avoid the use of steel fasteners as much as possible. While many materials are light, aluminum was also selected for manufacturability concerns. For example, the use of polymers or composites could require molds / fixtures, processes such as vacuum-bagging, etc. Aluminum however is able to be machined and bent easily.

5.5.2 Sensor and Electronics Placement

The next issue to address was the placement of the necessary instruments and onboard computer. Placement of the major components is shown in Figure 5.11. The choice of instrument placement was strategic rather than arbitrary. For example, the IMU is located in the center of the vehicle, coinciding with the axis of rotation and the center of mass. The Hokuyo laser range finder was placed on the leading edge of the vehicle so that the payload cannot obstruct the field

of view. Placements of the microcontroller and onboard computer (and their respective enclosures) were governed by the overall center of gravity of the vehicle.

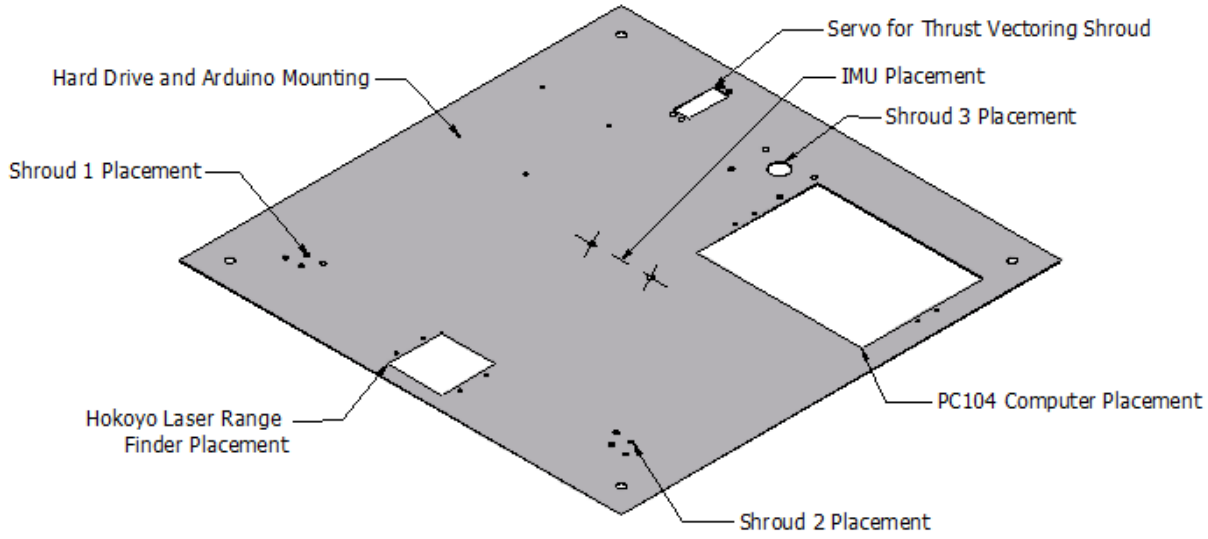

Figure 5.11. Solid model of the tethered vehicle's base structure. This illustrates the placements of all of the major components.

5.5.3 Structural Considerations

In effort to stiffen the vehicle up considerably, a structure was designed underside the vehicle. The structure was comprised of .030" thick aluminum sheet, bent to give a geometric cross section similar to a "C channel." This cross section was chosen to take advantage of the area moment of inertia, which resulted in a large bending stiffness. The area moment of inertia of all of the channels fabricated for the structure are equivalent, measuring in at .0022in^4. Figure 5.12 illustrates the layout of the bent channel structure. Note that holes were drilled in the vertical cross section component of each C channel beam. This was done in effort to lighten the structure. It was desired to secure the vehicle's base to the channel structure via aluminum rivets.

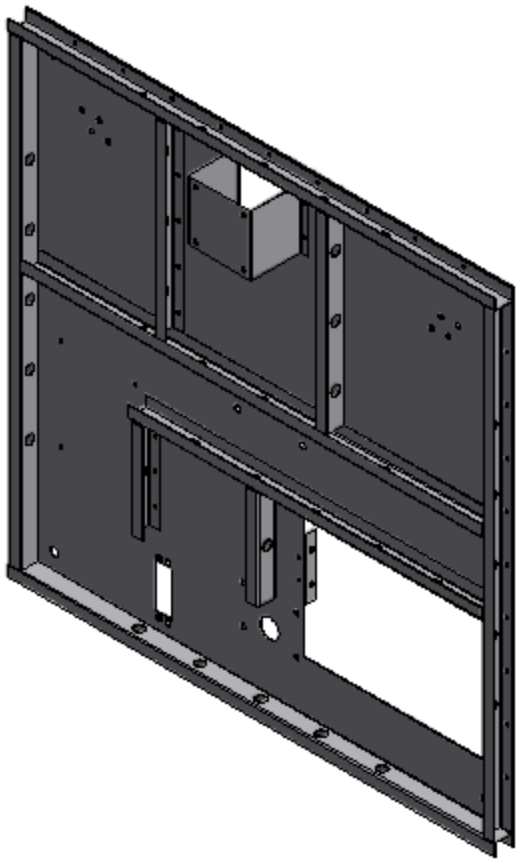

Figure 5.12. The bottom of the vehicle is visible here to show the designed supporting structure. The C channels are fabricated out of bent aluminum 6061 and feature lightening holes.

To validate the design of the vehicle's chassis / structure, several linear perturbation finite element models were developed in Abaqus CAE 6.10-2. The vehicle was loaded with a 20lb evenly distributed load and constrained at all four corners in the Z (vertical) axis. Only one corner was constrained in all three dimensions ($U_x = U_y = U_z = 0$) to allow the structure to deform as if it were tethered. The material properties used in the model are shown below in Table 5.2. The aluminum properties were obtained from [25].Note that the ABS material used and printed by the rapid prototyping machine does not exhibit the same properties as ABS that would otherwise be molded or extruded (properties used listed in [26]). In fact, the ABS material printed by the rapid prototyping machine is not isotropic [27]. However, with little data on the anisotropic constants of the FDM ABS, the model treats elements assigned the FDM ABS properties as isotropic. While this is not correct, the FDM ABS parts modeled are not structural and are not expected to carry any significant load. The finite element model of the vehicles

chassis / structure includes the use of several different elements to represent the geometry of the structure. In particular, continuum shell and brick elements were used. The components of the assembly were constrained by tying the contacting nodes together.

Table 5.2. Material properties used in the linear static deformation finite element model.

Aluminum 6061	
Young's Modulus, E	10,000ksi
Poissons Ratio, v	.33
FDM ABS Polymer	
Young's Modulus, E	236ksi
Poissons Ratio, v	.31

Prior to running the model, hand calculations were performed to estimate the maximum deflection and maximum bending stress on the C channel structural members of a simplified model. Stresses and deflections were estimated for the members running front-to-back (nominally 15.2" long) and left-to-right (nominally 16" long). This was done by assuming that bending was in the direction of the interest, and that the perpendicular members were rigid. The maximum bending stress and corresponding deflection was calculated by utilizing equations 5.4, 5.5, and 5.6 presented below. Note that 5.4 and 5.5 were derived for a simply supported beam.

$$M = \frac{\omega x}{2}(l - x) \tag{5.4}$$

$$\delta_{max} = -\frac{5\omega l^4}{384EI} \tag{5.5}$$

$$\sigma = \frac{Mc}{I} \tag{5.6}$$

Once the approximated stress and deflection values were calculated, the finite element model was executed. Several models were created with different meshes; mesh densities, etc until the model converged to a solution. Figure 5.13 is a plot of the von mises stress over the entire vehicle. Note that the maximum stress of 3000psi is occurring at the front-to-back C channels located on the outside perimeter near the lightening hole. The maximum deflection of .025" occurs in the front center of the vehicle, behind the Hokuyo laser range finder mount.

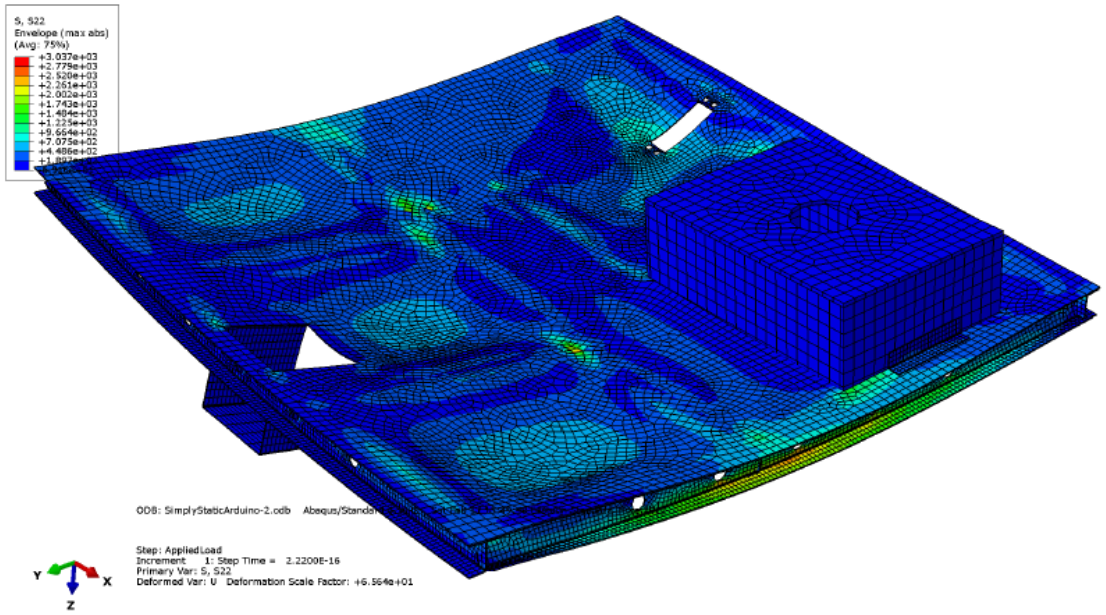

Figure 5.13. A plot of the averaged von mises stress on the loaded vehicle. The deformation is scaled by a factor of 65.

Table 5.3 tabulates the maximum von mises stresses and deflection. The values from the FEA model agree well with the approximated values calculated by equations 5.4, 5.5, and 5.6, suggesting that the finite element model is converging to the correct result. Note that the maximum stress is far less than the 40,000psi yield strength.

Table 5.3. Stresses and deflections as calculated from the finite element model.

Front-to-Back	**Finite Element**	**Strengths of Materials Solution**
Von Mises Stress, *psi*	2350	2560
Deflection, *in*	.020	.021
Left-to-Right		
Von Mises Stress, *psi*	1340	1350
Deflection, *in*	.017	.012
Maximum Stress, psi	3000	N/A
Maximum Deflection, *in*	.025	N/A

5.6. Vehicle Fabrication

Vehicle fabrication was fairly straight-forward, utilizing .030" thick 6061 aluminum. Part profiles were cut using a mill (in lieu of a water-jet, or laser cutter) and bent with a brake. Once the individual parts were fabricated, they were assembled by riveting them together using AN470A-3-2 solid aluminum rivets. Figure 5.14 shows the vehicle while being fabricated – both in the component phase and as it's being assembled together. Figure 5.15 shows the final product tethered to the ceiling of the Unmanned Systems Lab. In Figure 5.15, all subsystems are present. The onboard computer and Hokuyo laser range finder are visible. Because testing will focus on the linear control model presented briefly in this chapter and in chapter 6, the thrust vectoring servo was not installed.

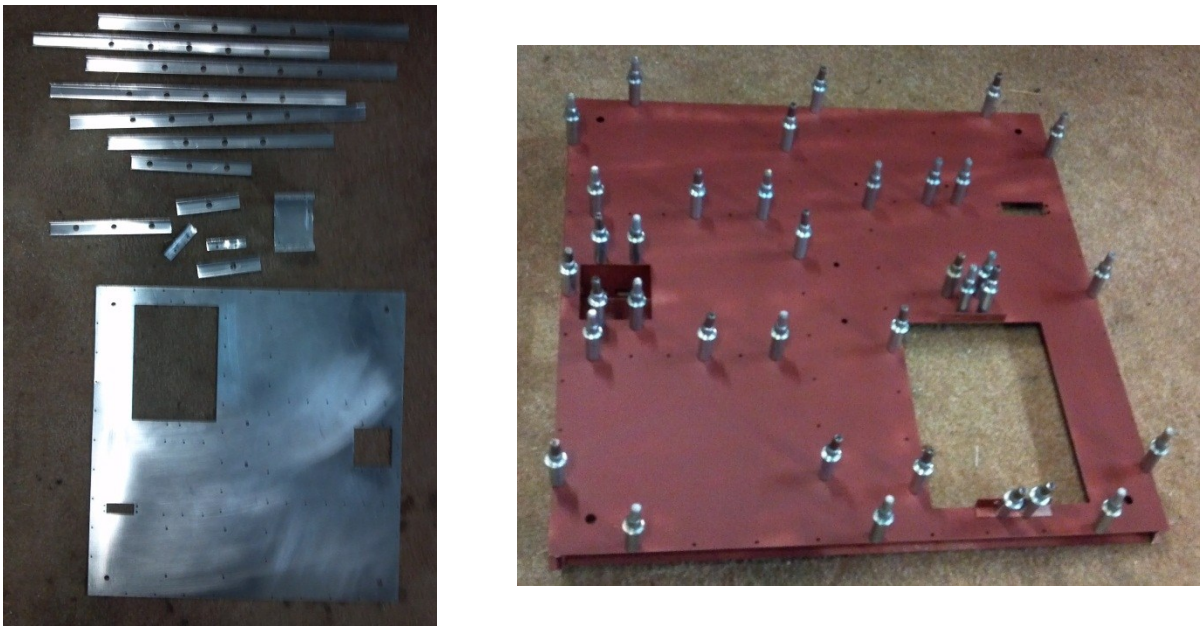

Figure 5.14. Left – the individual components of the vehicle structure are shown before assembly. Right – vehicle is in the process of being riveted.

Without batteries, the entire vehicle with all of the systems and wires installed weighed 8.1lb, which is below the 5kg (11.0lb) limit requirement discussed earlier in the chapter. This reduces the amount of thrust the thrusters must be able to produce to accelerate the vehicle .1g from the approximate 1lbf discussed earlier. At this point, the vehicle is ready to have the software uploaded to its onboard computer to tune the control algorithm. The next chapter focuses on the control of the vehicle.

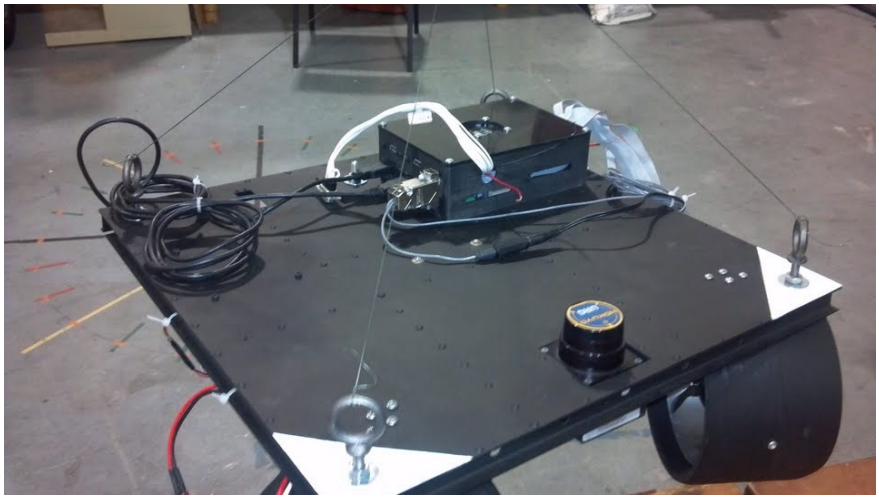

Figure 5.15. The vehicle with all of the subsystems installed. Note that the corners were painted white in case cameras were to be used to collect orientation and position information.

Chapter 6
Controller Design and Implementation

Chapter 5 briefly covered the dynamic model and control scheme used to control the vehicle as it relates to the vehicle's design. This chapter however will focus more in-depth on the dynamic model, controller, filtering, etc used to make the vehicle pilotless.

6.1 Spherical Pendulum Dynamics

The tethered vehicle paired with a helicopter resembles dynamics that can be represented by a spherical pendulum model as it can be described by X, Y, and Z coordinates. To derive the equations of motion, it was assumed that the base (helicopter) position was fixed, the tether was massless and rigid, and the payload could be represented by a point mass. Figure 6.1 illustrates a generic spherical pendulum system.

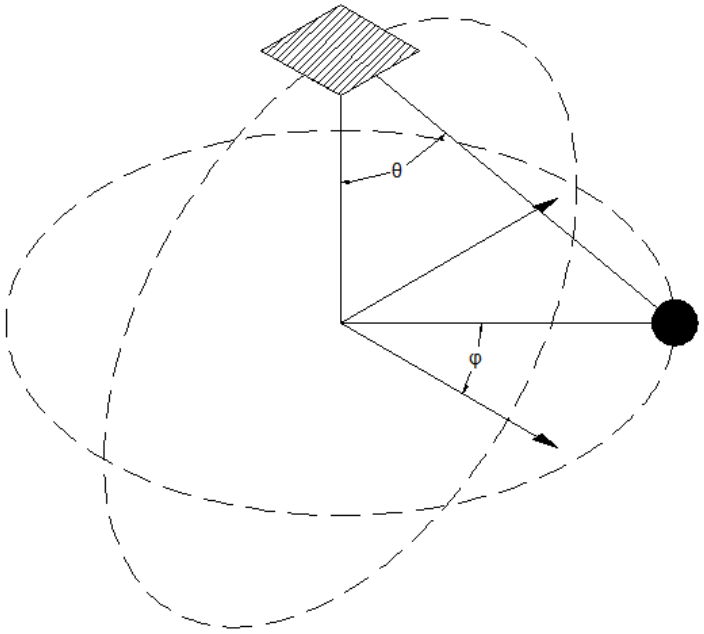

Figure 6.1. A generic model of a spherical pendulum attached to a fixed point.

Using the labeled parameters in Figure 6.1, the equations of motion were derived by taking the Lagrangian of the system. The Lagrangian of the system in terms of the angles φ and θ is shown in equation 6.1.

$$L = \frac{1}{2}mL^2\left(\dot{\theta}^2 + \dot{\emptyset}^2 \sin(\theta)^2\right) + mgL\cos(\theta) \tag{6.1}$$

The equations of motion in terms of these angles can be found by applying the Euler-Lagrange equations. There is more complete derivation of this shown in the appendix showing this step. From equation 6.1, it is apparent that the Lagrangian is independent of φ. The resultant equation of motion is shown in equation 6.2.

$$\ddot{\theta} + \frac{g}{L}\sin(\theta) - \dot{\emptyset}^2 \sin(\theta)\cos(\theta) = 0 \tag{6.2}$$

Two immediate problems arise from trying to control a spherical pendulum as governed by equation 6.2. First and foremost, the equation is nonlinear, presenting a problem for linear control theory. Second, the equation is in terms of two angular coordinates, θ and φ, both of which will not be measured. Instead, it is desired to measure the distance from the wall / obstacle and a corresponding yaw angle (with the Hokuyo laser range finder and Microstrain 3DM-GX2 IMU. This means that the equations of motion should be written in the Cartesian coordinate system. The linearized equation of motion, in terms of X is presented again below as equations 6.3. A similar equation can be derived for the Y direction; however it is not presented here as it was not used in the control scheme. In addition, the linearized equation for yaw is presented as 6.4. Note that the nonlinear equations expressed in Cartesian coordinates are not presented. The derivation is quite long, and is presented in numerous resources such as in [28].

$$m\ddot{x} = -T_1 \sin(\emptyset_1) - T_2 \sin(\emptyset_2) - T_3 \sin(\emptyset_3) - \frac{mg}{L}x \tag{6.3}$$

$$J\ddot{\theta} = R_1T_1 + R_2T_2 + R_3T_3 - c\dot{\theta} \tag{6.4}$$

The linearized equations of motion presented above are unfortunately valid for only a small operating range as they omit the difficulties surrounding the true nonlinear equations. For example, the small angle approximation (sin(x) is approximately equal to x, and cos(x) is approximately equal to 1) was used to linearize the equations. Large deflections in yaw therefore cannot be modeled, nor controlled correctly. In addition, the angles φ and θ as defined in Figure 6.1 must remain sufficiently small. As stated earlier, the helicopter is assumed to be stationary. Recall however that these assumptions and limitations are appropriate for the design range as it was assumed the helicopter was going to be operated in a quasi-hovered state with small pendulations.

6.2 Collecting Data and Filtering

Before a controller can be utilized to stabilize the vehicle, the data collected from the Hokuyo laser range finder and 3DM-GX2 IMU must be fused and filtered. This section of the chapter discusses the acquisition and processing of the data.

6.2.1 Data Collection

Recall from the previous chapter that data is collected from both the laser ranger finder and the IMU via USB and serial respectively. Even though both instruments are operating on relatively fast communication interfaces, they are constrained by their maximum update rates. These update rates, tabulated in table 6.1, are critically important to the success of any controller attempting to control a dynamic system. The rates shown in Table 6.1 are ideal as they do not account for processing / computational time. This is critically important to note for the scanning laser range finder as the collected data points must be processed first with the wall and window detection algorithm, which is already computationally intensive for the vehicle's computer.

Table 6.1. Instrument Update Rates for the primary instruments used onboard the vehicle [22] [24].

Hokuyo URG-04LX	10Hz
3DM-GX2 IMU	250Hz

Accounting for the instrument update rate and all of the processing that must be done, the vehicle's instrument update rate is going to be slow. Steps can be taken to combat this however. It is first noted in Table 6.2 that the dynamic states can theoretically be provided by both the laser ranger finder and the IMU. Code was written to update the controller with data collected just from the IMU (as opposed to using the IMU and laser range finder together) when laser range finder data is unavailable. It's important to note however that control solely off of the IMU is normally not done as MEMS (Micro-Electrical-Mechanical) IMU measurements based on the accelerometer and rate gyros have a bias error and tend to drift if not complemented with another instrument. Even though the bias error can accumulate quickly, it was hoped that the update rate of the laser range finder would be sufficient to correct the error and to provide accurate measurements.

Table 6.2. Instrument used for each dynamic state measurement. While position information is possible to collect in theory from the Microstrain IMU, it would require integrating the velocity, resulting in severe drift.

State	Laser Range Finder	IMU
Yaw Angle	X	x
Yaw Rate	X	x
Position	X	
Velocity	X	x

6.2.2 Sensor Filtering

Instruments such as the 3DM-GX2 IMU and URG-04LX laser range finder used onboard the vehicle are not perfect. Like all instruments, they have limited accuracy, resolution, repeatability, etc. In attempt to minimize the noise and provide the controller with measurements that accurately describe the vehicle's state; the acquired data needs to be filtered.

To introduce reasoning for filtering, the reader is first referred back to Figure 4.5, showing the calculated wall distance and angle from the Hough transform / wall detection algorithm. Even though the average measured distance and angle agreed with the actual physical dimensions, it is evident that noise is contained in the signal as it theoretically should be a constant measurement (.008m standard deviation for position and .979° standard deviation for the wall).

The data acquired from the laser range finder and Hough transform is not the only instrument subject to noisy measurements. IMUs, such as the 3DM-GX2 used onboard the vehicle are also subject to noise. In particular, IMUs generate erroneous measurements due to hysteresis and temperature compensation errors. IMUs also suffer from bias error, which results in drift. Considering that the operating environment of the tethered vehicle will be relatively constant, operating at ground level altitudes, bias error is arguably going to be the largest, most detrimental source of error seen from the IMU.

Bias error occurs when integration is required to acquire a state. For example, to find relative velocity or position from an IMU, it would require one or two integrations of the

accelerometer. The accumulation of the bias, b, results in a linear (to obtain velocity) or quadratic error, e, (to obtain position) as shown in equations 6.5 and 6.6 respectively.

$$e = b \cdot t \tag{6.5}$$

$$e = b \cdot \frac{t^2}{2} \tag{6.6}$$

To demonstrate the impact of bias error / drift, the yaw angle and velocity were sampled after the 3DM-GX2 IMU was disturbed in plane. Figure 6.2 shown below plots the drift of the yaw and velocity measurement from the IMU. This illustrates that while IMUs can be instrumental in providing dynamic state information, they cannot be used alone. The dynamic state measurements from the IMU will be filtered and complemented with the Hokuyo laser range finder.

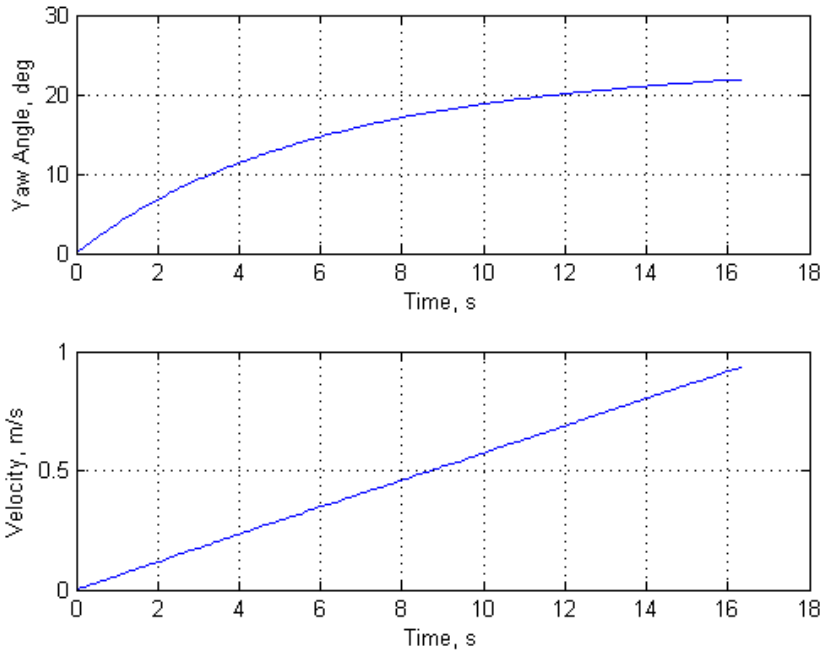

Figure 6.2. Yaw and velocity measurements, unfiltered and not complemented with any other data source. The drift of the yaw angle and velocity measurements is shown.

With the major sources of error identified, it is now possible to design a filter for the data. There are many types of filters out there – low pass, high pass, Kalman, and complementary to name a few. While all of these filter types can be used to filter the acquired data to some degree, Kalman and complementary filters are purpose-built for navigation applications [29].

Kalman filters are essentially predictor-corrector estimators. They are used to estimate a measured state by optimally minimizing the measurement's covariance. Kalman filters can be computationally intensive as the Kalman gains have to be calculated [29]. This is an issue as the onboard computer is not a high performance computer and is already being used intensively for the wall finding algorithm and instrument acquisition. Considering the limitations of the onboard computer, the Kalman filter was not implemented.

In lieu of the Kalman filter, the complementary filter was considered. Complementary filters are commonly used in navigation applications. They tend to be quicker computationally than Kalman filters; however, they do not consider the statistics of the noise in the signals [29]. In the case of the tethered vehicle, the complementary filter will be used to combine measurements from the IMU and laser range finder. A block diagram of the complementary filter that will be used is shown below in Figure 6.3.

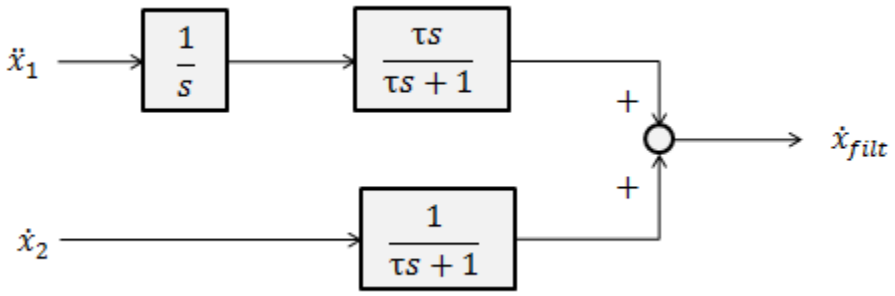

Figure 6.3. Block diagram of the complementary filter. In this particular example, acceleration from one source and velocity from another are complemented to produce a filtered velocity.

Figure 6.3 shows a complementary filter with two inputs, acceleration and velocity. Acceleration is first integrated to attenuate the signal. From there, it is passed through a high pass filter. A measured velocity signal is also passed through a low pass filter (complement of the high pass). These two signals are then added together to produce a filtered velocity measurement. The time constant, τ, seen in both the low and high pass transfer function, theoretically represents the duration of time that the filter acts on the signal. As this value directly impacts the performance of the entire complementary filter, it was adjusted during the implementation of the controller. Frequency domain techniques and simulation can also be used to determine a proper time constant.

To illustrate the usefulness of the complementary filter, the angle from the wall is plotted below in Figure 6.4. In the complementary filter, the laser range finder output was complemented with the IMU's angular velocity output. Figure 6.4 plots the calculated wall angle (in blue) from the Hough transform / laser range finder and the total state output as calculated from the complementary filter (in red).

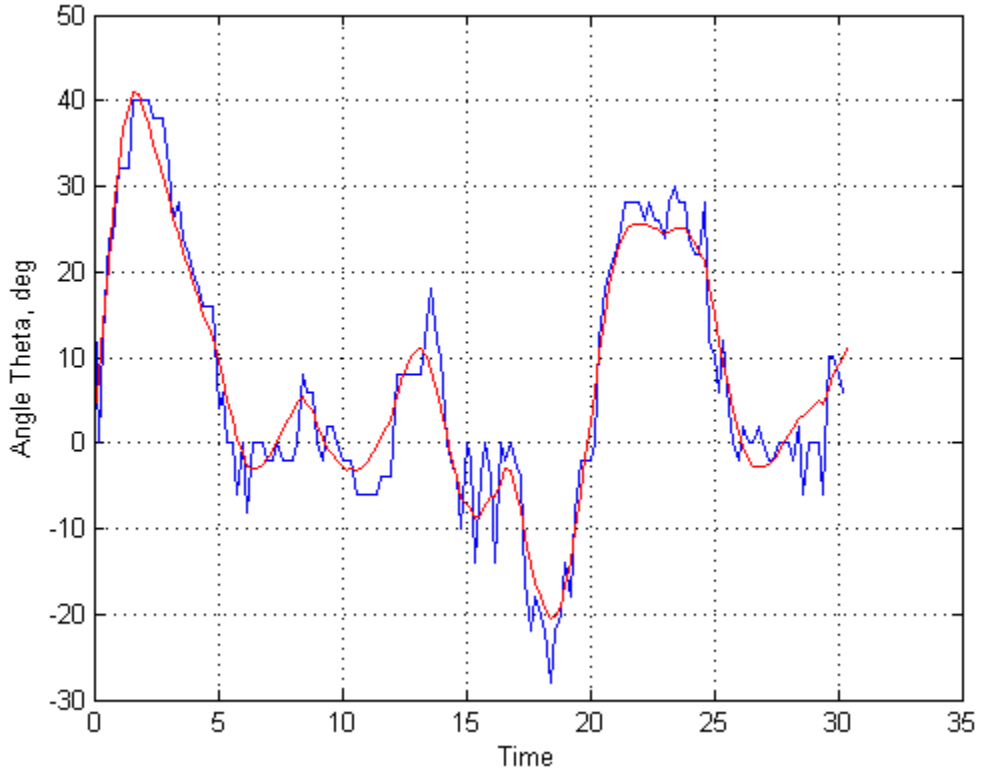

Figure 6.4. The perpendicular angle from the wall filtered and unfiltered. The perpendicular angle from the wall from the laser range finder is displayed in blue. The complementary filtered angle is shown in red.

The blue (original as calculated by the laser range finder) plot shown in Figure 6.4 is quite noisy compared to the filtered (red) plot. Considering that the tethered vehicle is a slow moving system, it is unlikely it would ever see angular rates of change as indicated by the original laser range finder output. If the vehicle was controlled off of the unfiltered input, it is likely it would oscillate, if not diverge. Figure 6.5 plots the position from the wall as collected from the laser range finder and complemented with the IMU output. While the noise associated with position is much less, the filter nevertheless attenuates the signal.

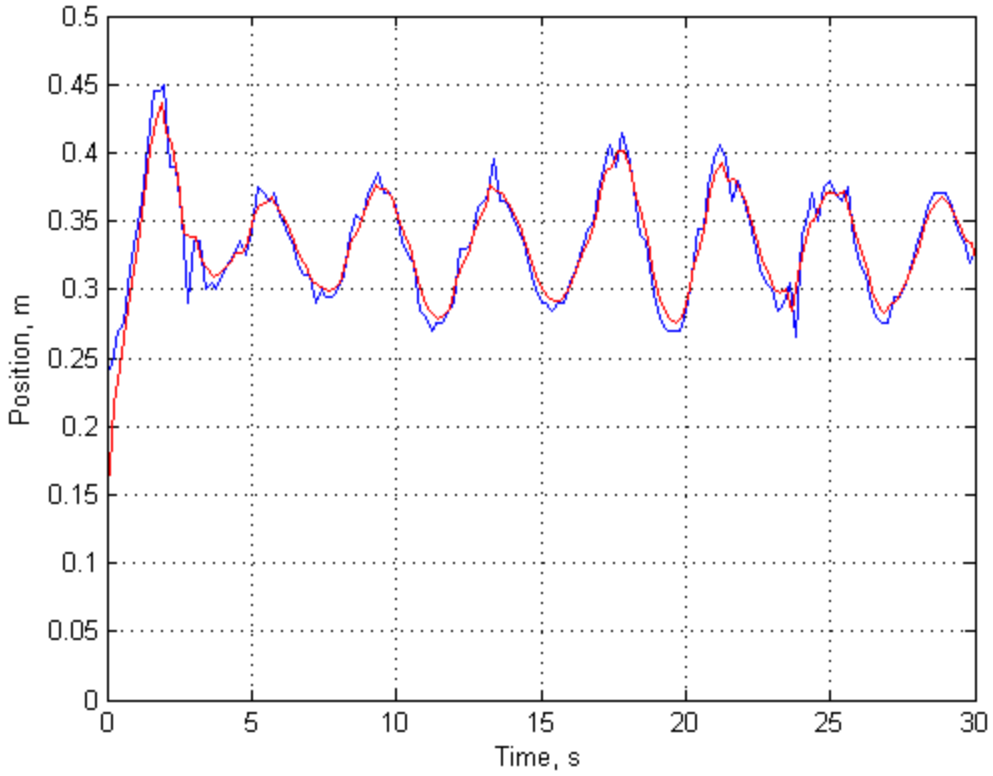

Figure 6.5. The perpendicular distance filtered and unfiltered. Perpendicular distance from the wall from the laser range finder is shown in blue, while the filtered is shown in red.

It's important to note that the complementary filter time constant, τ, is a function of the sampling time between intervals, *dt*. With a real time operating system, it's possible to control the sampling intervals, meaning the time constant will be constant. The vehicle's onboard computer is not a real time operating system however. As such, sampling times from iteration to iteration may be different, which may degrade the performance of the filter if severe enough.

6.3 Controller Design

This section of the chapter expands upon the controller design discussed in Chapter 5. The results of testing the implemented discrete controller are also compared to simulations and discussed.

6.3.1 Multiple Input Multiple Output Control

Multiple-input multiple-output control can be achieved in many different ways. In the linear control world, this is commonly done by a full state feedback controller utilizing state-

space equations. Optimal methods also exist for linear controllers, such as the linear quadratic regulator. The controller designed for the tethered vehicle is a full state feedback controller; of which iterative pole placement techniques were used.

Before a controller can be designed, a state space representation of the dynamic system must be derived. Equation 6.8, reprinted from earlier in section 6.1 and also in Chapter 5, is shown below and represents the state space representation of the system. This system will be controlled using the linear control law shown in equation 6.9. Using equation 6.8, the controller (6.9) will be able to control yaw angle, yaw angle rate, position from the wall, and velocity to the wall. Recall that sway parallel to the wall and the motor / shrouded propeller dynamics are not accounted for in these equations. Equation 6.8 utilizes the assumptions discussed in section 6.1. In particular, small oscillations and yaw of the payload is necessary for equation 6.8 to be valid.

$$\dot{x} = Ax + Bu \tag{6.7}$$

$$\begin{bmatrix} \dot{\theta} \\ \ddot{\theta} \\ \dot{x} \\ \ddot{x} \end{bmatrix} = \begin{bmatrix} 0 & 1 & 0 & 0 \\ 0 & -\frac{c}{J} & 0 & 0 \\ 0 & 0 & 0 & 1 \\ 0 & 0 & -\frac{g}{L} & 0 \end{bmatrix} \begin{bmatrix} \theta \\ \dot{\theta} \\ x \\ \dot{x} \end{bmatrix} + \begin{bmatrix} 0 & 0 & 0 & 0 \\ \frac{R_1}{J} & \frac{R_2}{J} & \frac{R_3}{J} & \frac{R_4}{J} \\ 0 & 0 & 0 & 0 \\ \left(-\frac{\sin(\emptyset_1)}{m}\right) & \left(-\frac{\sin(\emptyset_2)}{m}\right) & \left(-\frac{\sin(\emptyset_3)}{m}\right) & \left(-\frac{\sin(\emptyset_4)}{m}\right) \end{bmatrix} \begin{bmatrix} T_1 \\ T_2 \\ T_3 \\ T_4 \end{bmatrix} \tag{6.8}$$

The next step in designing a linear full state feedback controller is to determine controllability. By calculating the controllability matrix, controllability of the system can be determined. This is done by subtracting the rank of the controllability matrix from the maximum length of the *A* matrix. Executing this calculation reveals that for the given physical parameters of the system, no uncontrollable states exist. The system should be controllable given proper pole placement.

$$u = -\boldsymbol{K}x \tag{6.9}$$

Once controllability was determined, the open loop system was turned into a closed loop system by placing a feedback loop with gain matrix *K* in the loop and utilizing the control law in equation 6.9. A Simulink schematic is shown in Figure 6.6. Pole placement techniques were used to calculate the gain matrix *K*. Considering pole placement determines the eigenvalues of the *A-BK* matrix (the closed loop system), this is a critical step. Placing poles therefore directly influences the dynamics of the system. Incorrectly placing poles can result in an unstable system. Pole placement will also influence the system's response (speed, oscillation, etc).

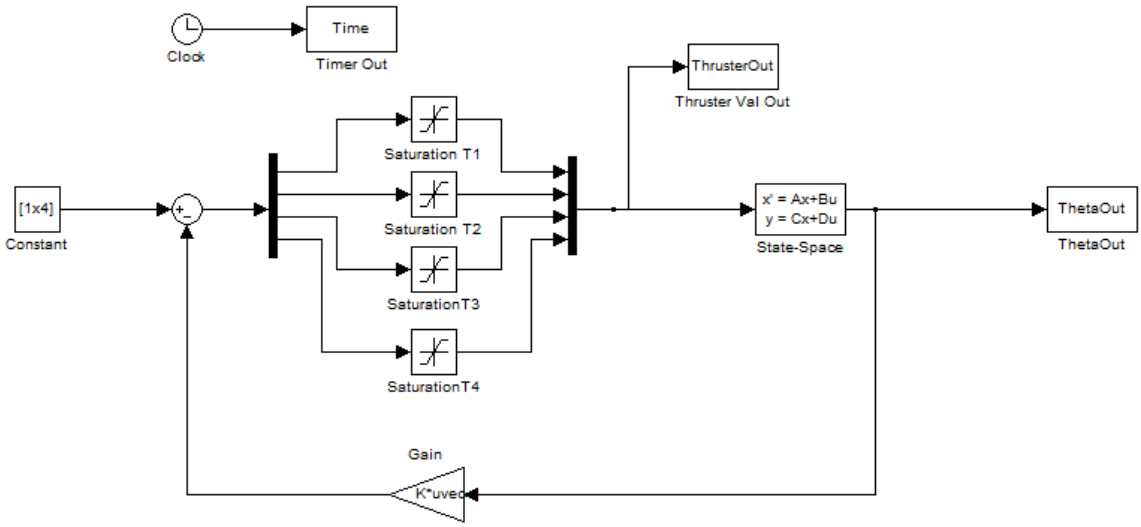

Figure 6.6. Original Simulink model used to design the full state feedback controller.

Similar to the method explained in Chapter 5, pole placement was done iteratively by a MATLAB script and Simulink model. Poles were changed for the given design parameters with the goal of minimizing settling time. In addition, thruster output was examined to make sure the thrusters were not saturating during operation. Several poles (and therefore gain matrices) were selected and tested with mixed success (this process will be explained later).

It's important to note that the full state feedback controller designed to control the vehicle was designed in continuous time. This is significant as the controller will be executed on a computer, where the state and actuation update rates will be discrete. Seeing as most implementations are discrete, this isn't necessarily an unknown practice. Implementing a controller designed in continuous time will cause the eigenvalues of the system (and therefore cause the dynamic response to change) when implemented on a discrete system.

The controller was simulated in continuous time and implemented discretely (using a digital computer to execute it). Both results indicated that the system should remain stable. The system responses of the continuous and discrete implementations are shown in Figure 6.7. Figure 6.8 plots the shrouded propeller output for the continuous and discrete controllers. Note that the red plotted line is the discrete controller.

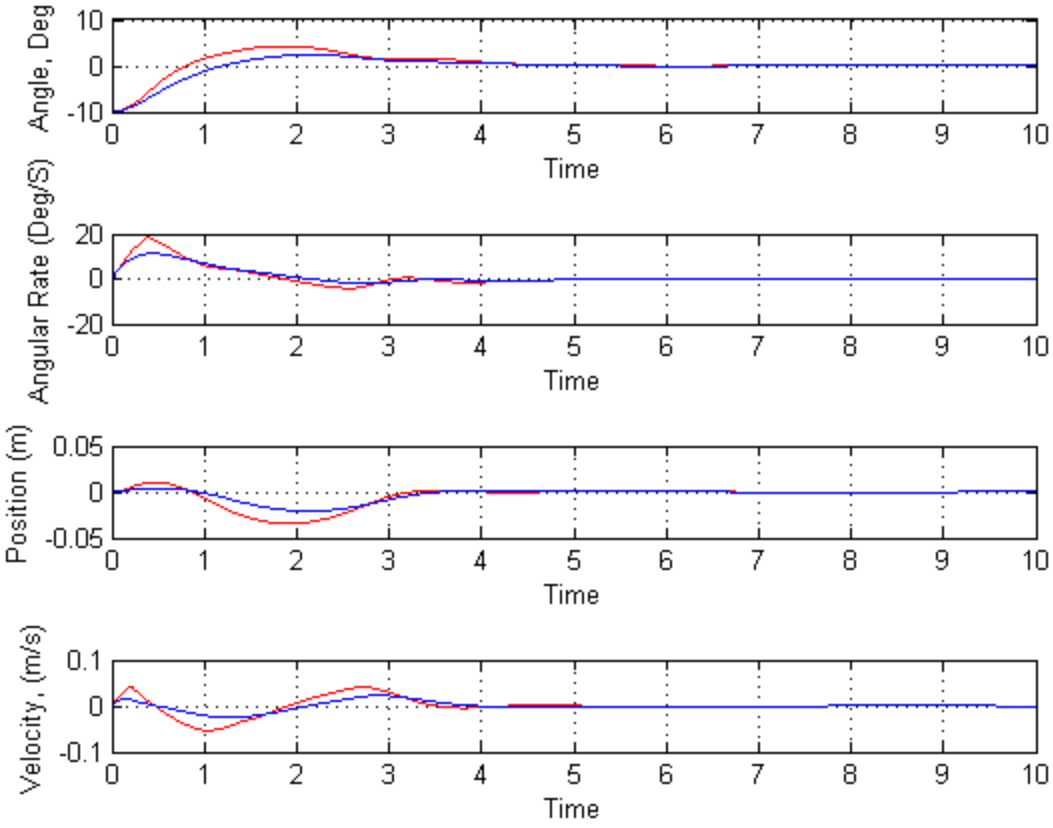

Figure 6.7. The continuous and discrete responses. The continuous response is shown in blue. The discrete response is plotted in red. While both implementations converge, the continuous response exhibits less overshoot.

Figure 6.7 illustrates both the continuous and discrete response in continuous time. That is to say, this is not representing the state information that the controller would be using as that information is discrete as well. It is evident from this plot that the discrete simulation of the controller tends to overshoot more than the continuous simulation. The discrete implementation was simulated by using a zero-order hold function. Given that the acquisition rate of the laser range finder is slow, the wall detection algorithm is time consuming, and other data processing / communication must occur, the sampling frequency was estimated to be 5Hz. This frequency was used as the update rate for the zero-order hold.

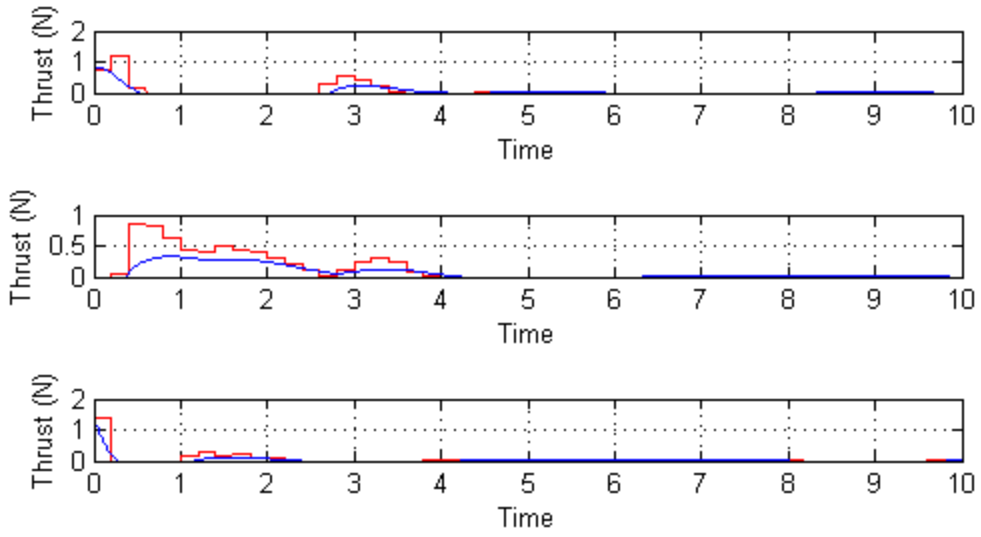

Figure 6.8. Simulated actuator / thruster output for the continuous and discrete implementations of the controller. The discrete controller is shown in red.

The controller was designed for the physical parameters shown in Table 6.3. These values were predicted from computer generated solid models and verified with measurements. These are important to note, as while the controller will exhibit some robustness, a significant deviation from these physical values could cause divergence. In an actual implementation of the vehicle, these parameters could change significantly depending on the payload and tether length.

Table 6.3. Physical parameters used in designing the linear full state feedback controller. The controller was tested onboard a vehicle with these physical parameters

Parameter	**Value**
Pendulum Length, *m*	3.8
Mass, *kg*	4.4
Moment of Inertia, kgm^2	.121
Thrust Saturation, *N*	3.1

6.3.2 Modeling Deficiencies

Despite simulating the controller in discrete time, several modeling deficiencies exist. In addition to the linearized dynamics the controller must use for a nonlinear problem, the following deficiencies exist:

- The thrusters / shrouded propellers have dynamics of their own that are not accounted for. In the model presented above, the controller is assuming an instantaneous response of the shrouded propellers. In reality, the motors have a finite acceleration and therefore need time to spin up to speed. Likewise, the shrouded propellers' angular velocity cannot be reduced instantaneously. These deficiencies are arguably the most important. In addition, the dynamic effects associated with the shrouded propeller are not characterized either (static thrust was characterized only at steady state).
- Gyroscopic effects of the shrouded propellers are not accounted for. If the propellers are spinning while the vehicle is rotating, forces will be generated due to the angular conservation of momentum. These forces will vary with respect to the angular velocities of the propellers and the vehicle.
- Aside from the simulated 5Hz zero-order hold, the software acquisition and output is not accounted for (ex communication between instruments, microcontroller, etc). Seeing as the onboard computer is running Microsoft Windows with NI's LabVIEW, it is possible for the iteration / update rates of the controlling and acquisition loops to be variable as low level timing control is not possible. It is for these reasons that the 5Hz rate may not be realistic at times.
- Long tether dynamic are not accounted for. The model assumes that the tether is always in tension and aside from the joints, not flexible. In reality, a tether is unable to resist any appreciable moment. Depending on the length of the tether, aerodynamic drag due to translation, wind, etc, could influence the dynamics.

6.4 Controller Implementation

After designing the controller and simulating it in MATLAB, it was coded in LabVIEW and installed on the vehicle's onboard computer. Many implementations were attempted by varying the matrix K and saturation limits. The response of each implementation was compared. This section of the chapter discusses the testing of the vehicle controller. In addition, the several issues were discovered during the testing of the controller are discussed.

6.4.1 Verifying the Controller

Many experiments were run to verify the operation of the designed controller. In particular, the controller was tested to make sure the vehicle was stable and to verify its response

to small disturbances. The vehicle was tested using DOW residential sheathing to simulate walls / windows. To simulate a tether, the vehicle was suspended from the ceiling of the Unmanned Systems Lab using a 3.8m length 80lb test line.

Many implementations of different gain matrices *K* and actuator saturation limits were tested with the vehicle. Even though simulations indicated stability, some implementations were not stable for all time. In addition, it was found that the vehicle entered instability when the position state deviated from zero. This is most likely due to the fact that the vehicle's controller did not control yaw very well. A plot of the yaw state as collected is shown in Figure 6.9. Compared to the simulations for the same initial conditions shown also in Figure 6.9, the actual implementation does not agree well as the actual controller does not settle. If the vehicle was trying to control position as well, this extreme oscillation would violate the small angle approximation and cause the vehicle to go unstable.

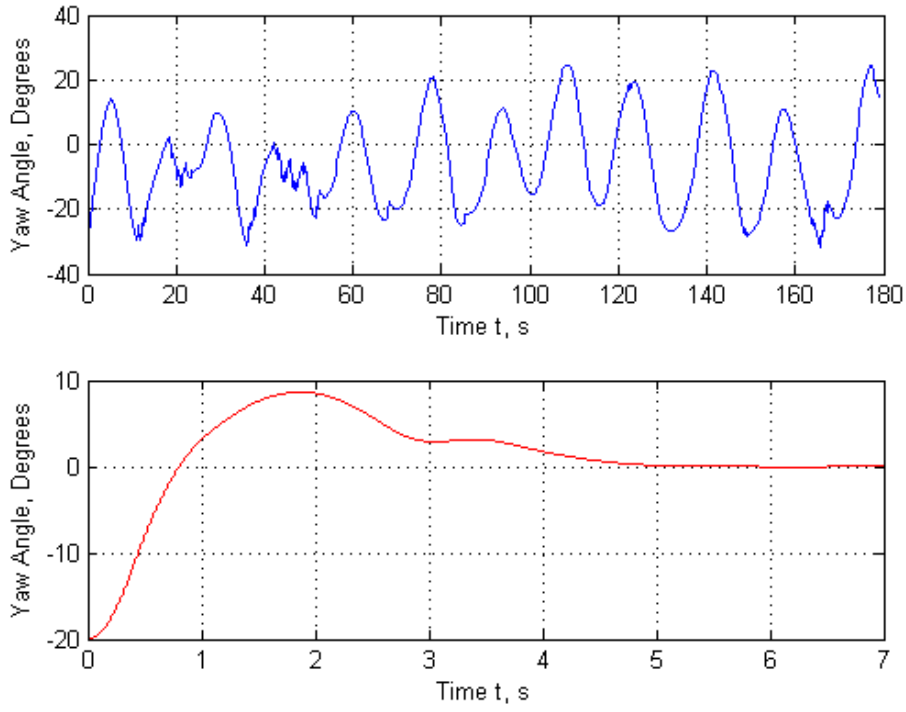

Figure 6.9. Comparison of actual yaw data to simulated data. Actual response is plotted as blue, while the discrete response is shown in red. The implemented controller does not settle.

The behavior shown in Figure 6.9 was typical of all stable controllers implemented on the vehicle. Physical parameters such as the mass, moment arms of the shrouds, center of gravity (and rotation), and moment of inertia of the vehicle were measured and verified through

software. The shrouded propeller saturation limits were also adjusted multiple times. In these trials, it was discovered that 25% of the maximum producible thrust was the maximum allowable saturation limit before the vehicle's motion became divergent. The "thrust vectoring" shroud was placed in multiple orientations, with no significant improvement. Despite these efforts, the controller response did not noticeably improve. Several cases were run with the wires suspended from the edge of the vehicle (used to power the vehicle). In these cases, the vehicle eventually settled (attributed to the light damping / restoring force of the wires).

The failure of the controller to adequately control yaw and distance from the wall is attributed to the model deficiencies discussed previously in this chapter (section 6.3.2). In particular, it is thought that deriving a model that can account for more of the dynamics would be beneficial. This includes modeling of the shrouded propellers and their respective electronic speed controllers, the gyroscopic forces, and perhaps using more representative nonlinear equations. A linear model based on pole placement or optimization techniques such as a linear quadratic regulator may be used with some success if the shrouded propeller dynamics are more appropriately accounted for.

A simulation was recreated in MATLAB Simulink using the same linear controller in attempt to match the experimental data. This new model included the use of time constants in attempt to simulate the inertia and response of the shrouded propellers. The simulated plot as compared to the actual data is shown below in Figure 6.10. The period and amplitude of the simulation are roughly equivalent to the actual collected data. Several sources of error include the variable sampling increment and the simulation of collected data with noise and filtering. It's important to note though that the use of a time constant to represent the shrouded propellers can be deceiving. In essence, all of the dynamic deficiencies are being lumped into the time constant. While it is likely that the shrouded propellers do have a significant lag as discussed earlier, it is difficult to ascertain the relative magnitude and contribution of each deficiency.

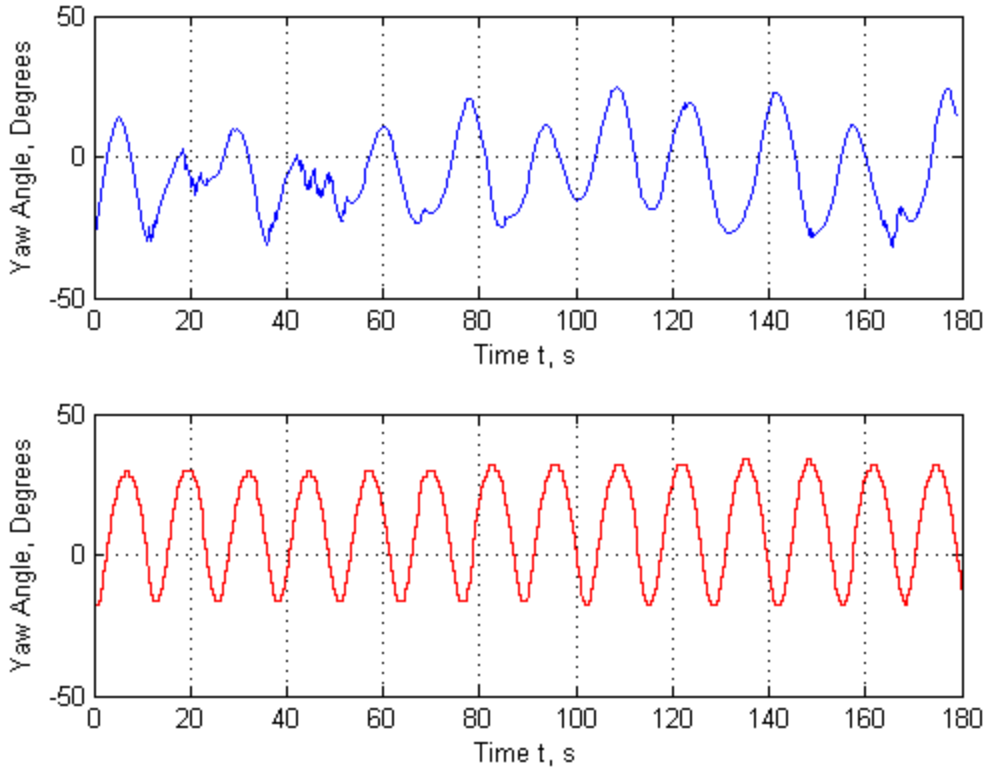

Figure 6.10. Comparison of actual yaw data to corrected simulated data. Time constants are included to represent the actual dynamics and control. The implemented (blue) and simulated controller (red) do not settle.

6.5 Momentum Actuation and Control

In addition to using the shrouded propellers as actuators, yaw control by the use of a momentum-exchange system was investigated, simulated, and tested. This was primarily done as the controller developed for the shrouded propellers exhibited little control authority. In addition, it was of interest if actuation by another method with the same hardware and sensors could provide better authority. Momentum control was achieved by the use of a reaction wheel. In general, reaction wheels find their use in space vehicle applications such as satellites. They are generally used as part of a broader attitude control system, which may feature several reaction wheels, thrusters, etc. Reaction wheels in these systems are often used to compensate for small disturbances such as radiation pressure. Using a motor or other device to spin the wheel, momentum can be exchanged between the vehicle and the actuator and the orientation of the vehicle can be preserved [30].

Reaction wheels do have their disadvantages. In particular, due to conservation of angular momentum and the physical limitations of the motor / device to actuate the wheel, the wheel may saturate. That is to say, the maximum speed of the reaction wheel may be reached before the disturbance is compensated for.

The reaction wheel as an actuation method was implemented onboard the tethered vehicle for several different reasons. First, the dynamic model of a single reaction wheel to control yaw is relatively simple and can describe the dynamics more completely than the model used for the shrouded propellers. System parameters such as the motor constants, moments of inertia, etc are respectively published by manufacturers and can be designed for. In addition, by using the more complete reaction wheel dynamic model, it may be possible to evaluate if system deficiencies such as the slow update rates still act as a severe detriment to the controller.

6.5.1 Reaction Wheel Design

The reaction wheel actuation system was designed to be small enough to fit onboard the vehicle in the payload area and to possess enough actuation authority to yaw the vehicle. First, a motor, motor controller / driver, and gearbox were selected. These were selected based on simulations conducted in MATLAB Simulink to determine the necessary torque to actuate the vehicle based on a given initial condition and the maximum rotational velocity. A Maxon EC-max30 brushless DC motor with a GP32 4.8:1 gearhead was selected to provide actuation to the reaction wheel. To drive the wheel, a Maxon DEC 50/5 motor controller was selected. The DEC 50/5 is capable of speed and current control modes by the use of a 0-5V analog pin. In addition, the 50/5 driver is able to reverse direction and brake the motor (although uncontrolled) by shorting the coils. Finally, a National Instruments myDAQ was used to provide the 0-5V and digital pins required by the DEC 50/5. Figure 6.11 shows the system layout for the reaction wheel.

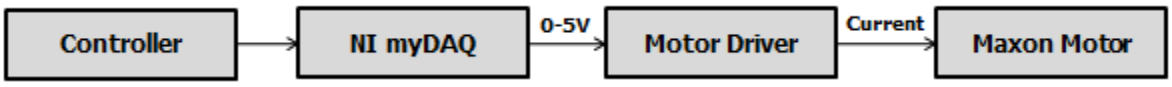

Figure 6.11. The reaction wheel system layout.

Several reaction wheels were designed and machined out of 6061 aluminum into a solid circular disc. The wheel and motor were mounted at the vehicle's center of mass. The physical

parameters of the system as implemented are shown in Table 6.4. It's important to note that the machined wheel must be concentric and balanced, especially if the vehicle is expected to counteract any disturbance.

Table 6.4. Physical parameters of the reaction wheel.

Parameter	**Value**
Wheel Moment of Inertia, kg-m^2	.0028
Motor Rotor Inertia, g-cm^2	21.9
Motor Torque Constant, Nm/A	.0243
Motor and Gearhead No-Load Max RPM	1940

Figure 6.12 is a photograph of the implemented system. The reaction wheel consumed most of the usable payload area of the vehicle. An actual practical implementation would most likely have to include a wheel below the payload area to ensure the vehicle is still useful.

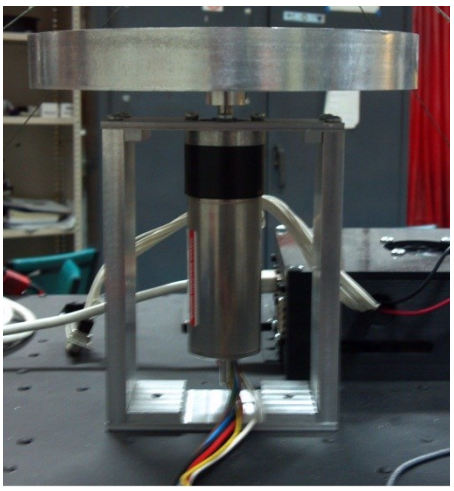

Figure 6.12. The reaction wheel implemented onboard the vehicle.

6.5.2 Reaction Wheel Dynamic Model

As stated earlier, the reaction wheel dynamic model is simple consisting of mostly known parameters. The model presented in equations 6.10 (rewritten as 6.11 in terms of the wheel moment of inertia and acceleration) was derived using a torque balance. The torque, T, required to actuate the vehicle can be written in terms of the moment of inertia of the wheel and angular acceleration. Torque can also be expressed in terms of current and the torque-current constant of

the motor. These relationships were used to develop a linear full state feedback controller, controlling angle and angular rate of the vehicle.

$$J\ddot{\theta} = T \tag{6.10}$$

$$J\ddot{\theta} = -I\ddot{\theta_w} \tag{6.11}$$

The DEC 50/5 will be used to control current delivered to the motor. This is critical because while many of the system parameters are known in this case, the characteristics of the DEC 50/5 motor driver / controller are not known. While the 0-5V input to output current relationship can be measured, the actual response, braking, slowing down (the motor will spin down in an uncontrolled fashion), etc can be difficult to characterize and incorporate into control dynamics. In addition, the gears in the gearhead will have some sort of backlash that can become evident, especially if the wheel has to change direction or slow down substantially (during testing, the backlash was audible during direction change). Nevertheless, equation 6.10 with the system parameters discussed in this chapter was formed into a state space equation which was used to implement a linear full state feedback controller.

6.5.3 Controller Implementation

As stated previously, a linear full state feedback controller was implemented to control the vehicle via actuating the reaction wheel. It's important to note here that during testing that the motor was constrained through limits imposed in software. This was done to prevent the motor from damaging the DEC 50/5 should the software controller want to brake / change directions of the motor. This limited the amplitude of the disturbances that could be introduced into the system.

The controller was first evaluated in its steady state performance. This was done ensuring the vehicle was first parallel with the wall before the controller was enabled. Once the controller was enabled, the yaw was collected and plotted in Figure 6.13. Note how the vehicle still oscillates, although at a much smaller amplitude as before with the shrouded propellers (about 2 degrees from the mean 0). This oscillation is most likely due to the slow update rates (which have not changed from the shrouded propeller actuation) and the model deficiencies.

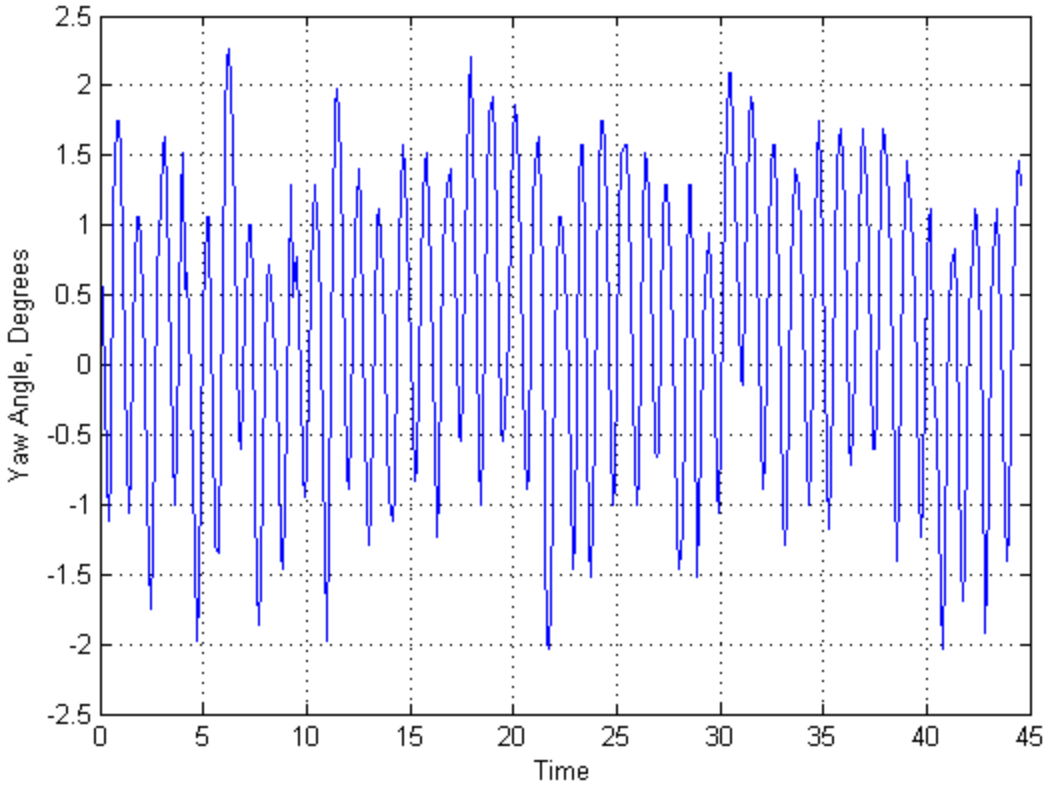

Figure 6.13. Yaw performance using the reaction wheel at steady state.

It's important to note that the reaction wheel controller, while written in LabVIEW, was not implemented on the PC104. The controller was implemented on a computer with an Intel Core2 Duo clocked at 2.54GHz with 4.00GB of RAM, which is substantially faster than the PC104. While computation time should decrease with this setup, the acquisition limitations of the instruments (laser range finder and IMU) should stay the same. The computer running the controller was not equipped onboard the vehicle. This required several wires to be connected to the vehicle, which arguably provided some amount of damping and restoring torque.

Several tests were conducted by setting the vehicle to an initial condition. In these tests, the wheel was able to turn the vehicle to have a 0 degree angle with the wall. The results of such a test are shown in Figure 6.14.

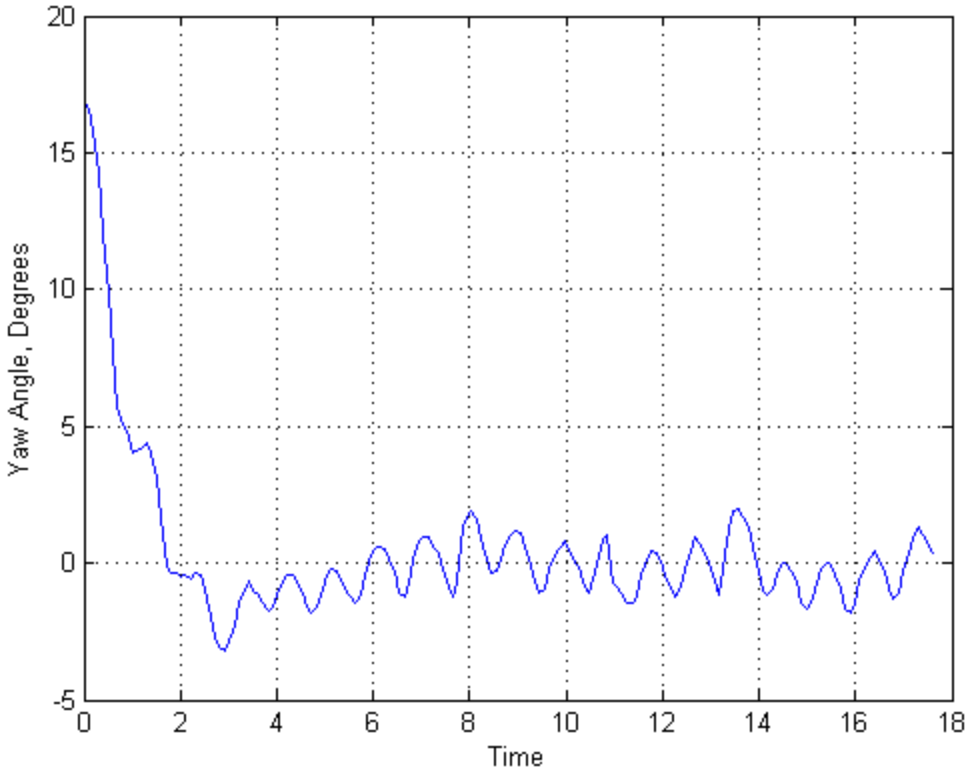

Figure 6.14. Yaw performance using the reaction wheel with an initial condition of approximately 15 degrees.

As Figure 6.14 illustrates, the vehicle was able to be turned successfully to the proper orientation. Notice the vehicle still oscillates about the zero set point. This again is due to probably the slow sampling rate and model deficiencies. Recall that the motor will spin freely down in an uncontrolled manner. The lack of control is probably one of the single biggest deficiencies of the model and most likely contributes the most to the oscillatory response. The system response to other initial conditions was similar to that shown in Figure 6.14, possessing the oscillatory behavior about 0 degrees. This was true so long as the Hokuyo laser range finder was able to see a wall.

Even though the controller seemed to perform better than the controller using the shrouded propellers, several practical considerations remain. First and foremost is the actuation authority of the reaction wheel. A long duration or high amplitude disturbance torque can saturate the reaction wheel rendering it useless. Second, the reaction wheel usually must be designed to have a relatively high moment of inertia. This generally involves using a

combination of a high density material and a large diameter wheel. These two traits contrast the requirements of the vehicle to be light and to be able to support some sort of payload. The wheel will not only lower the useful weight of the tethered vehicle but also use area and volume that could otherwise be used to carry a useful load.

Chapter 7
Conclusion and Recommendations

This thesis presented the research and design methodology used in the development of the helicopter slung actuated vehicle. The completed tasks and a discussion of recommended changes to continue onward with this research are presented in this final chapter.

7.1 Summary of Work

The overall design requirements and project motivation / applications are discussed in the first chapter. These design requirements with the consideration of the project motivation were used to develop a helicopter slung vehicle for the purpose of precision placement of payloads. The overall vehicle requirements imposed requirements on the vehicle's subsystems.

The vehicle developed in this thesis was unique not only in terms of application, but also in the fact that it required multiple, very different systems to be developed, tested, and implemented. This included the development of the propulsion system, the wall and window detection system, the controller, and the system architecture / mechanical design of the vehicle itself. Each system was split into its own separate chapter, covering the design requirements of that and the resultant design / implementation of each individual system.

The propulsion system was the first system to be presented in this thesis. Utilizing the vehicle design requirements, design requirements specific to propulsion were developed and presented. In particular, a system that was relatively quiet and could produce 1.0lbf in the direction perpendicular to the wall was desired. After briefly examining multiple propulsion mechanisms / machinery, it was decided to utilize shrouded propellers. Shrouded propellers were researched to develop a set of more specific design requirements. From these requirements, a shrouded propeller that had a nominal 5.0" inlet diameter and had a 4.0" chord length was designed. To increase thrust output, a diffuser was designed, causing the shroud to have an area ratio of 1.25.

Initially, the shrouded propeller was manufactured completely by an FDM rapid prototyping machine utilizing a machined down remote control aircraft propeller. The shrouded propeller was characterized in a series of static thrust tests. Power consumption, thrust, and thrust vs pulse width of the electronic speed control were determined. Unfortunately however, the prototype shroud had several deficiencies, the most important being an eccentric shroud.

Even though the prototype propeller had a deficiency with the eccentrically printed shroud, the aerodynamic properties were considered favorable. The final shroud design therefore possessed the same geometry; however, it was now split until a multi-component assembly. The assembly consisted of a shroud lip, center body, and diffuser. To address the issue of eccentricity and rigidity, the shroud center body was manufactured using machined 6061 aluminum parts. Consuming about 50W of power at full throttle, the final shroud design produces 0.7lb of thrust, meeting the design requirement.

In order for the vehicle to navigate and avoid walls while slung from the helicopter, a wall and window detector needed to be developed. A wall detection algorithm was developed utilizing the Hough transform and a Hokuyo URG-04LX scanning laser range finder. The wall and window algorithm were tuned for accuracy and speed using thresholds and resolution parameters. Ultimately, this algorithm was used to provide state information to the controller.

The mechanical design and system architecture of the vehicle was presented next. In this chapter, electronic hardware was selected so that all of the systems could reliably communicate. Software was then developed in LabVIEW to run on the onboard computer, incorporating debugging tools and the controller in an easy to use interface. Linear control theory was utilized to develop a program to iterate pole placement and physical parameters of the system (placement and orientation of the shrouded propellers, weight, etc). The vehicle's mechanical design takes into consideration the parameters as calculated by the program and the design requirements. Ultimately, a vehicle was developed out of 6061 aluminum utilizing aircraft fabrication techniques. It had a square planform area measuring 16"x16" and incorporated all of the necessary systems for the vehicle to function.

Finally, a linear controller was developed. This controller controlled four states of the vehicle, yaw, yaw rate, position from the wall, and velocity. Utilizing pole placement techniques and an iterative MATLAB program, the controller gain matrix was calculated. The controller was implemented in LabVIEW. Theoretical simulations were also constructed and analyzed for stability and settling time. When implemented however, the controller did not perform to expectations. Many trials of different gain matrices and saturation limits were conducted; however, none provided a completely non-oscillatory response. It was concluded that the limitations of the linear controller, the simplified linear dynamic model, and the low sampling rate were the main causes of failure.

7.2 Suggestions for Future Work

This thesis presents a good foundation for an actuated tethered vehicle. Even so, there are many improvements one could make should the research be continued. Deficiencies exist at a system and vehicle level that should be corrected to increase reliability. This section of the chapter identifies deficiencies that should be corrected in the future.

While the shrouded propellers satisfy the design requirements, they can be improved a number of different ways. For example, the propellers used in the shrouded propeller are commercially available propellers for remote control aircraft that were machined to fit inside the shroud. Propellers can potentially be fabricated using injection molding techniques to better suit the application. For example, the solidity ratio, chord length, number of blades, angle of incidence, etc, can all be manipulated and optimized for the operating conditions of the shroud.

In addition to propellers, the shrouds can be redesigned to save weight and space. This can be achieved principally by addressing the shrouded propellers length. Recall that the shrouds were designed to be rather long to assist the diffuser. However, with experimental data showing the diffuser is only causing modest gains in thrust, the diffuser can probably be shortened. Decreasing the chord length of the shroud will reduce viscous drag, possibly allowing for an increased thrust output. Nevertheless, shortening the chord length will decrease the weight of the vehicle.

Since the shrouded propellers are the actuators the controller is using to orient the vehicle, their dynamics are important. In this thesis, the characterization of the thrust and pulse width signal delivered to the electronic speed controller was used in the controller to determine the thrust output. In actuality, the shrouded propeller has dynamics of its own as the motor has a finite acceleration. Modeling the shrouded propellers accurately would likely help in the control of the vehicle.

The wall and window detector seems to work accurately and produce repeatable results. However, the speed of the detector can probably be increased using a probabilistic Hough transform. In any case, the Hokuyo URG-04LX is not sufficient for acquiring the data. With scan rates of 100ms, the URG-04LX inherently limits the update speed of the vehicle. For a system that needs to have a controller onboard to perform correctly, this limitation placed on the update

rate is certainly not ideal. To correct this, another instrument (or multiple instruments) should probably be used to obtain faster acquisition rates.

In addition to the scanning laser range finder, acquisition and update rates are influenced by the onboard PC104 computer. The PC104, used in many embedded applications, is not necessarily the best computational platform to use for this application. Equipped with just an Intel Atom processor and 1.0GB of RAM, the computer is far from state-of-the-art. In addition to this, the onboard computer was running Microsoft Windows and LabVIEW, both of which can be resource demanding. This combination of software left a lot to be desired as well – as minimum timing control was available at this level. To correct this in the future, a computational platform that has a real time processor should be investigated. FPGAs, National Instruments' RIO, and various other platforms exist that could provide more computational power and access to the lower level hardware. If a platform is selected that has digital GPIO ports available, the ATmega1280 microcontroller used in the system architecture could be eliminated in its entirety.

Even though the simulated controller did well, the actual implemented controller left a lot to be desired. The controller is undoubtedly influenced by the update rate issue discussed previously. In addition, highly nonlinear system dynamics were linearized. This is inconsistent with the actual dynamics and is somewhat responsible for poor controller performance, especially when the system experiences a large perturbation, or needs to control position while yawing. To correct this issue, a more advanced modern controller may need to be implemented. While an optimal linear controller, such as the linear quadratic regulator, can be used with probably a little more success on a faster system that modeled more of the dynamics (ex thruster dynamics), it may be worth it to jump straight to a controller that can account for the nonlinear dynamics. In addition, this system will be experiencing large disturbance forces as well from the rotor blades, wind / wind gusts, etc – all of which may cause a linear controller to diverge.

While a tether ideally doesn't collapse and can be modeled as a rigid link, this may not be adequately representative enough of tether dynamics. Future work therefore may include investigating scenarios at which the vehicle is deployed using a very long tether. For example, the dynamics of a long tether may be susceptible to the wind and gust like disturbances. These disturbances could cause the vehicle / tethered payload to deviate from its orientation and position.

Bibliography

[1] Department of the Air Force, Airdrop of Supplies and Equipment: Rigging Airdrop Platforms TO13C7-1-5, Washington, DC: Headquarters, 2001.

[2] Lockheed Martin, "K-MAX Delivers for U.S. Marines," 31 January 2012. [Online]. Available: http://www.lockheedmartin.com/us/ms2/features/120131-k-max-delivers-for-u-s-marines.html. [Accessed 19 February 2012].

[3] J. Vaughan, A. Yano and W. Singhose, "Comparison of robust input shapers," *Journal of Sound and Vibration,* vol. 315, no. 4-5, pp. 797-815, 2008.

[4] W. Singhose, J. Lawrence, K. Sorensen and D. Kim, "Applications and Educational Use of Crane Oscillation Control," *FME Transactions,* vol. 34, no. 4, pp. 175-183, 2006.

[5] J. Lawrence and W. Singhose, "Command Shaping Slewing Motions for Tower Cranes," *Journal of Vibrations and Acoustics,* vol. 132, no. 1, 011002, 2010.

[6] R. A. Stuckey, "Mathematical Modelling of Helicopter Slung-Load Systems," DSTO Aeronatuical and Maritime Research Laboratory, Victoria, Australia, 2002.

[7] J. E. May, "Tethered Payload Control from an Autonomous Helicopter," Virginia Polytechnic Institute and State University, 2010.

[8] Input Shaping Lab @ Georgia Tech, "Flying Crane Research," 29 May 2007. [Online]. Available: http://singhose.marc.gatech.edu/FlyingCrane/index.html. [Accessed 21 February 2012].

[9] S.-R. Oh, J.-C. Ryu and S. K. Agrawal, "Dynamics and Control of a Helicopter Carrying A Payload Using A Cable-Suspended Robot," University of Delaware, Newark, 2005.

[10] W. Kruger, "On Wind Tunnel Tests and Computations Concerning the Problem of Shrouded Propellers," National Advisory Committee for Aeronautics, Washington, 1949.

[11] R. J. Platt, "Static Tests of a Shrouded and an Unshrouded Propeller," National Advisory Committee for Aeronautics, Washington, 1948.

[12] H. H. Hubbard, "Sound Measurements for Five Shrouded Propellers at Static Conditions," National Advisory Committee for Aeronautics, Washington, 1950.

[13] D. M. Black, H. S. Wainauski and C. Rohrbach, "Shrouded Propllers - A Comprehensive Performance Study," American Inst of Aeronautics and Astronautics, Philadelphia, 1968.

[14] R. O. Duda and P. E. Hart, "Use of the Hough Transform to Detect Lines and Curves in Pictures," Artificial Intelligence Center, Menlo Park, 1971.

[15] C. Galambos, J. Matas and J. Kittler, "Progressive Probabilistic Hough Transform for line detection," in *Computer Vision and Pattern Recognition, 1999. IEEE Computer Society Conference on.*, Fort Collins, 1999.

[16] P. Kultanen, L. Xu and E. Oja, "Randomized Hough Transform (RHT)," in *Pattern Recognition, 1990. Proceedings., 10th International Conference on*, 1990.

[17] K. D. Korkan, G. M. Gregorek and D. C. Mikkelson, "A Theoretical and Experimental Investigation of Propeller Performance Methodologies," in *AIAA/ASME/SAE 16th Joint Propulsion Conference*, Hartford, 1980.

[18] A. Raspet, "The Ducted Propeller for STOL Airplanes 60-AV-11," in *ASME Aviation*

Conference, Dallas, 1960.

[19] A. Akturk and C. Camci, "Tip Clearance Investigation of a Ducted Fan Used in VTOL UAVS," in *ASME Turbo Expo Turbine Technical Conference*, Vancouver, 2011.

[20] R. J. Weir, "Ducted Propeller Design and Analysis," Sandia National Laboratories, Albuquerque, 1987.

[21] R. J. Weir, "Aerodynamic Design Considerations for a Free-Flying Ducted Propeller," in *AIAA Atmospheric Flight Mechanics Conference*, Minneapolis, 1988.

[22] Hokuyo, "Hokoyo Laser Range Finder URG-04LX Specifications," [Online]. Available: http://www.hokuyo-aut.jp/02sensor/07scanner/urg_04lx.html. [Accessed 20 January 2012].

[23] Embedded Solutions, "ADLS15PC," [Online]. Available: http://www.adl-usa.com/products/cpu/datasheets/ADLS15PC.pdf. [Accessed 25 January 2012].

[24] MicroStrain, "3DM-GX2 Technical Product Overview," 13 July 2008. [Online]. Available: http://files.microstrain.com/3dm-gx2_datasheet_v1.pdf. [Accessed 26 January 2012].

[25] Matweb, LLC, "Aluminum 6061-T6 Material Properties," Matweb, LLC, [Online]. Available: http://www.matweb.com/search/DataSheet.aspx?MatGUID=1b8c06d0ca7c456694c7777d9e10be5b&ckck=1. [Accessed 28 Dec 2011].

[26] Redeye, "Parts for Prototype and Production - ABS," Redeye, Eden Prairie, 2008.

[27] S.-H. Ahn, M. Montero, D. Odell, S. Roundry and P. K. Wright, "Anisotropic material properties of fused deposition modeling ABS," *Rapid Prototyping,* vol. 8, no. 4, pp. 248-257, 2002.

[28] E. M. Abdel-Rahman, A. H. Nayfeh and Z. N. Masoud, "Dynamics and Control of Cranes: A Review," *Journal of Vibration and Control,* vol. 9, no. 7, pp. 863-908, 2003.

[29] W. T. Higgens, "A Comparison of Complementary and Kalman Filtering," *Aerospace and Electronic Systems, IEEE Transactions on,* Vols. AES-11, no. 3, pp. 321-325, 1975.

[30] R. W. Froelich and H. Patapoff, "Reaction Wheel Control for Space Vehicles," *Automatic Control, IRE Transactions on,* vol. 4, no. 3, pp. 139-149, 1959.

[31] W. Singhose, N. Singer and W. Seering, "Comparison of Command Shaping Methods for Reducing Residual Vibration," in *European Control Conference*, Rome, Italy, 1995.

Appendices

Appendix A

Shrouded Propeller Static Thrust Theory

Thrust and power relations for shrouded propellers / ducted fans can be theoretically calculated by the use of momentum theory. First consider the hypothetical shroud cross section pictured below in Figure A-1 with a propeller and a diffuser.

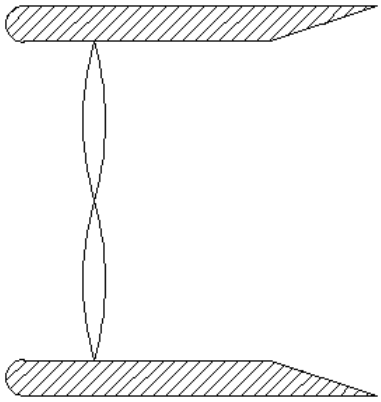

Figure A-1. Cross section of a generic shrouded propeller.

Recall that the propeller spins, generating lift, and therefore thrust. So long as the flow doesn't separate from aggressive diffusion, the downstream flow remains attached to the walls. Assuming the air is a constant density, a mass balance of the shrouded propeller can be written where the subscript *e* refers to the exit and *p* refers to the propeller disc.

$$A_e V_e = A_p V_p$$

It is next noted that the power required for the generated thrust, assuming no losses, can be written as follows.

$$P = \frac{1}{2}\dot{m}V_e^2$$

With,

$$\dot{m} = \rho A_p V_p$$

Then,

$$P = \frac{1}{2}\rho A_p V_p V_e^2$$

Substituting the relations discussed above, power is then expressed as

$$P = \frac{1}{2}\rho A_p V_e^3 \frac{A_e}{A_p}$$

The thrust generated by the shrouded propeller can be found using conservation of momentum.

$$T = \dot{m} V_e$$

From the above power relation,

$$V_e = \sqrt[3]{\frac{2P}{\rho A_e}}$$

$$T = \sqrt[3]{\frac{2P}{\rho A_e}} \rho A_e V_e$$

This is simplified to,

$$T = \rho A_e \left(\frac{2P}{\rho A_e}\right)^{\frac{2}{3}}$$

It is important to note that there are several assumptions in the function presented above. First, inviscid flow theory is used. Viscous drag, which plays a large part in the low Reynolds number shrouds designed in this thesis, is not accounted for. Second, it is assumed that the pressure at the exit of the shroud is equivalent to atmospheric (far-field). Rotational effects are also neglected. Nevertheless, the equations derived with momentum theory, as shown above, were used in the preliminary design of the shroud.

Appendix B

Derivation of Spherical Pendulum Equations of Motion

The tethered vehicle developed in this thesis is governed by an equation of motion that resembles a spherical pendulum. This appendix derives the spherical pendulum equations of motion. The derivation presented below considers Figure B-1.

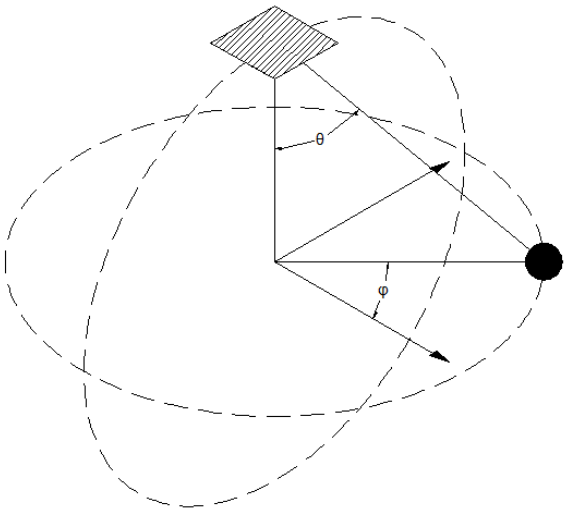

Figure B-1. A generic model of a spherical pendulum attached to a fixed point. This figure is reprinted from Chapter 6.

The spherical pendulum equations of motion are derived using the Lagrangian. The :Lagrangian is defined as

$$L = T - V$$

Using the conventional right-hand coordinate system in Figure B-1, the x, y, and z position of the pendulum can be written in terms of angles φ and θ.

$$x = L\cos(\emptyset)\sin(\theta)$$

$$y = L\sin(\emptyset)\sin(\theta)$$

$$z = -L\cos(\theta)$$

Writing the Lagrangian (a function of kinetic and potential energy),

$$L = \frac{1}{2}m(\dot{x}^2 + \dot{y}^2 + \dot{z}^2) - mgz$$

The equations of motion are easily written in terms of the angles φ and θ as opposed to the rectangular coordinates x, y, and z. Taking the derivative of the x, y, and z relations presented above, the Lagrangian can be rewritten as,

$$L = \frac{1}{2}mL^2\left(\dot{\theta}^2 + \sin(\theta)^2\,\dot{\phi}^2\right) + mgL\cos(\theta)$$

Applying the Euler-Lagrange equations,

$$\frac{d}{dt}\left(\frac{\partial L}{\partial \dot{\theta}}\right) - \frac{\partial L}{\partial \theta} = 0$$

$$\frac{\partial L}{\partial \dot{\theta}} = L^2 m\dot{\theta}$$

$$\frac{\partial L}{\partial \theta} = -gLm\sin(\theta) + L^2 m\cos(\theta)\sin(\theta)\,\dot{\phi}^2$$

This yields the equation of motion,

$$\ddot{\theta} + \frac{g}{L}\sin(\theta) - \dot{\phi}^2\sin(\theta)\cos(\theta) = 0$$

Appendix C

Mechanical Prints

The following table is a list of mechanical prints for the components of the vehicle that were machined. Please refer to the page number for the corresponding print.

Component	Quantity	Page
Shroud Center Body Ring	1	96
Shroud Motor Mount	1	97
Stiffeners	10	98
Floorboard	1	99-106

MATERIAL: 6061 Aluminum

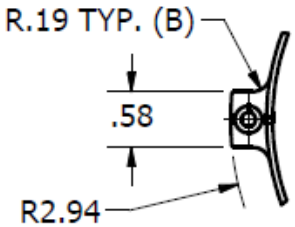

DETAIL B
SCALE 1/2

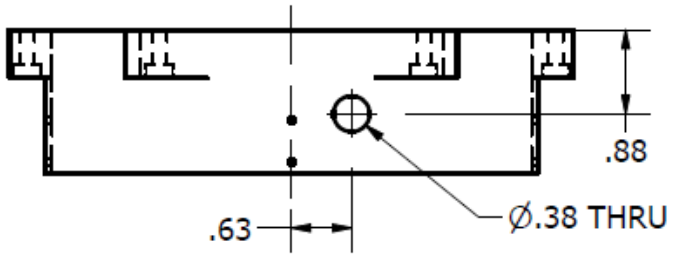

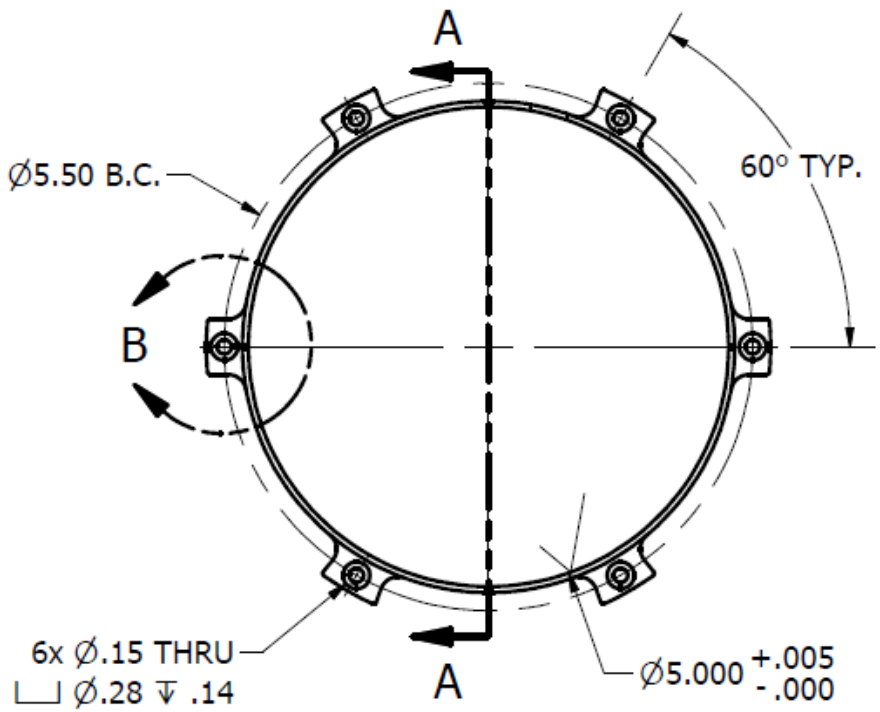

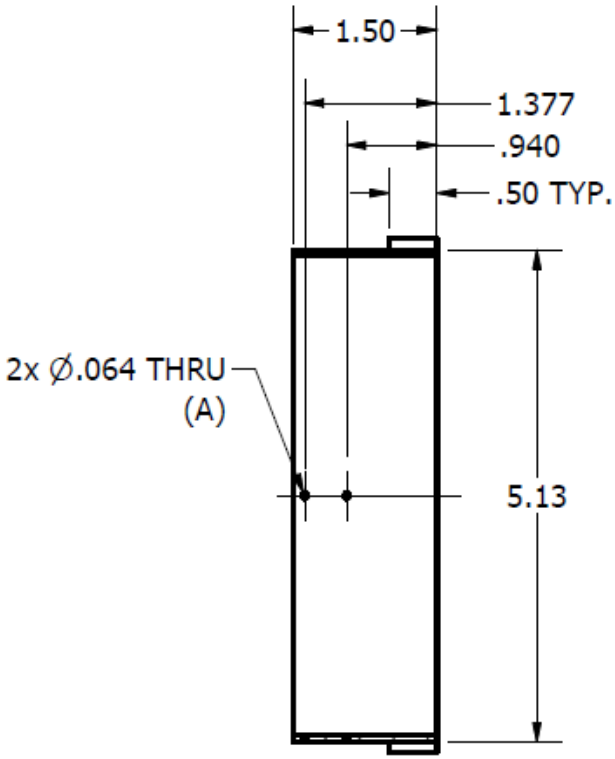

SECTION A-A
SCALE 1/2

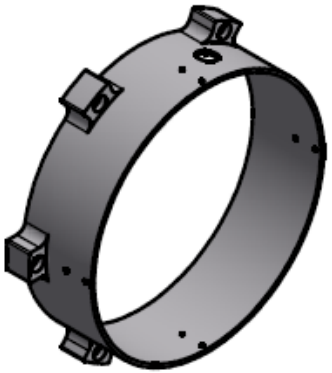

NOTES:
1. Feature (B) radius in DETAIL B is not critical.
2. Part to be free of burrs and sharp edges.
3. Feature (A) to be indexed every 90 degrees.

Dimensional Tolerances Unless Otherwise Specified
Machining
Fractions: ±1/64, Angles:±1°
2 place decimals: ±0.010, 3 place decimals: ±0.005
Unmarked surface finishes: 125 RMS or better
Castings
d < 1": ±1/64, 1" < d < 12": ±1/32, d > 12": ±1/16
Angles: ±1°, Concentricity: 0.03 T.I.R.

Notes:

This drawing exists as a solid model. Please contact the designer if desired.

REV	DESCRIPTION	DATE	APPROVED
1	RELEASED		RJC

Unmanned Systems Lab
Virginia Tech
Blacksburg, VA
http://www.me.vt.edu/unmanned/

Ring, Centerbody, Shroud

Drawn	Checked	Date	Drawing No.	Rev
RJC	RJC		SR-1	1

Scale	Part No.	Size
1/2	SR-1	A

MATERIAL: 6061 Aluminum

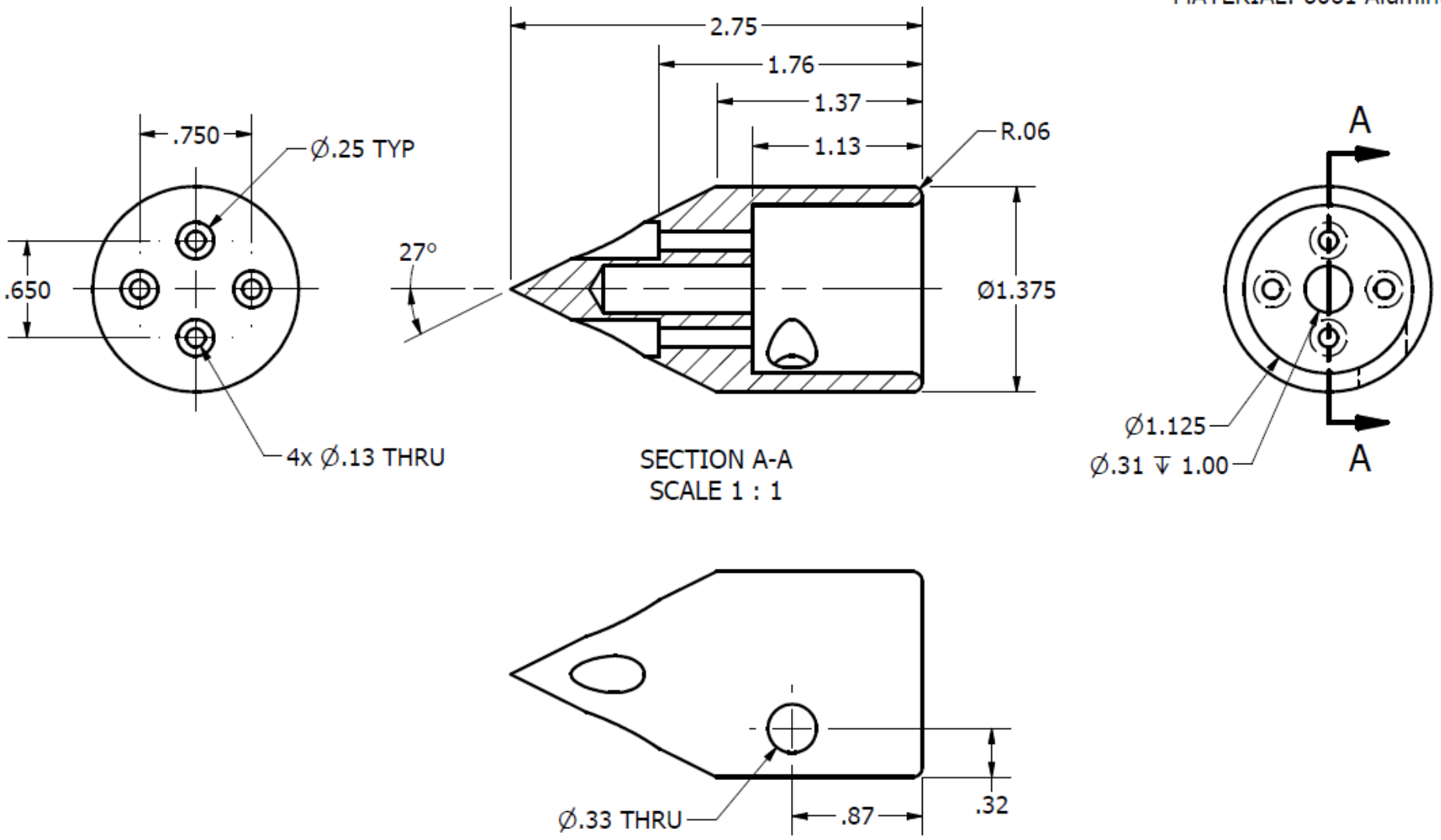

Dimensional Tolerances Unless Otherwise Specified
Machining
Fractions: ±1/64, Angles:±1°
2 place decimals: ±0.010, 3 place decimals: ±0.005
Unmarked surface finishes: 125 RMS or better
Castings
d < 1": ±1/64, 1" < d < 12": ±1/32, d > 12": ±1/16
Angles: ±1°, Concentricity: 0.03 T.I.R.

Notes:

This drawing exists as a solid model. Please contact the designer if desired.

REV	DESCRIPTION	DATE	APPROVED
1	RELEASED		RJC

Unmanned Systems Lab
Virginia Tech
Blacksburg, VA
http://www.me.vt.edu/unmanned/

Mount, Motor, Shrouded Propeller

Drawn	Checked	Date	Drawing No.	Rev
RJC	RJC		SR-2	1

Scale	Part No.	Size
1:1	SR-2	A

MATERIAL: 6061 Aluminum

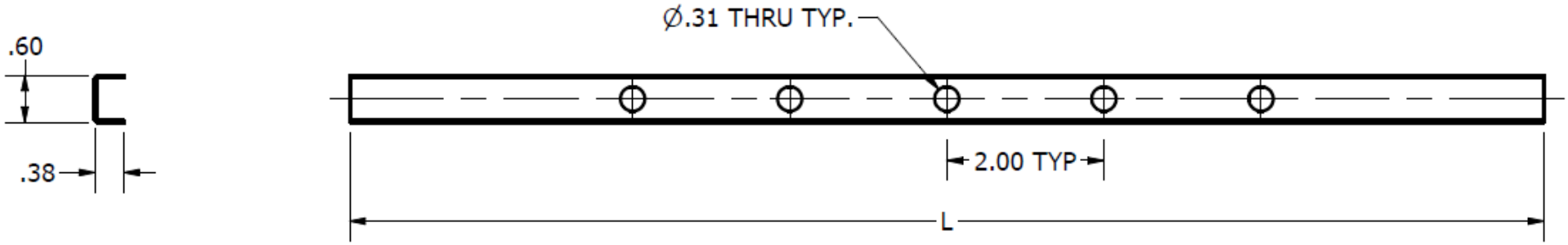

Stiffeners	
Length	QTY
16	2
15.2	3
11.63	1
6.25	2
3.25	2

NOTES:
1. All stiffeners to have the same cross section.
2. Desired thickness of .025 inches.
3. Holes to be drilled every 2.00 inches.
4. All parts to be free of burrs and sharp edges.
5. Bending radius not critical.
6. Stiffeners to be secured to floor board with $^{3}/_{32}$ rivets, match drilled thru the top flange.

REV	DESCRIPTION	DATE	APPROVED
1	RELEASED		RJC

Dimensional Tolerances Unless Otherwise Specified
Machining
Fractions: ±1/64, Angles:±1°
2 place decimals: ±0.010, 3 place decimals: ±0.005
Unmarked surface finishes: 125 RMS or better
Castings
d < 1": ±1/64, 1" < d < 12": ±1/32, d > 12": ±1/16
Angles: ±1°, Concentricity: 0.03 T.I.R.

Notes:

This drawing exists as a solid model. Please contact the designer if desired.

Unmanned Systems Lab
Virginia Tech
Blacksburg, VA
http://www.me.vt.edu/unmanned/

Stiffener, Vehicle

Drawn	Checked	Date	Drawing No.	Rev
RJC	RJC		V-STF	1

Scale	Part No.	Size
NONE		A

MATERIAL: 6061 Aluminum

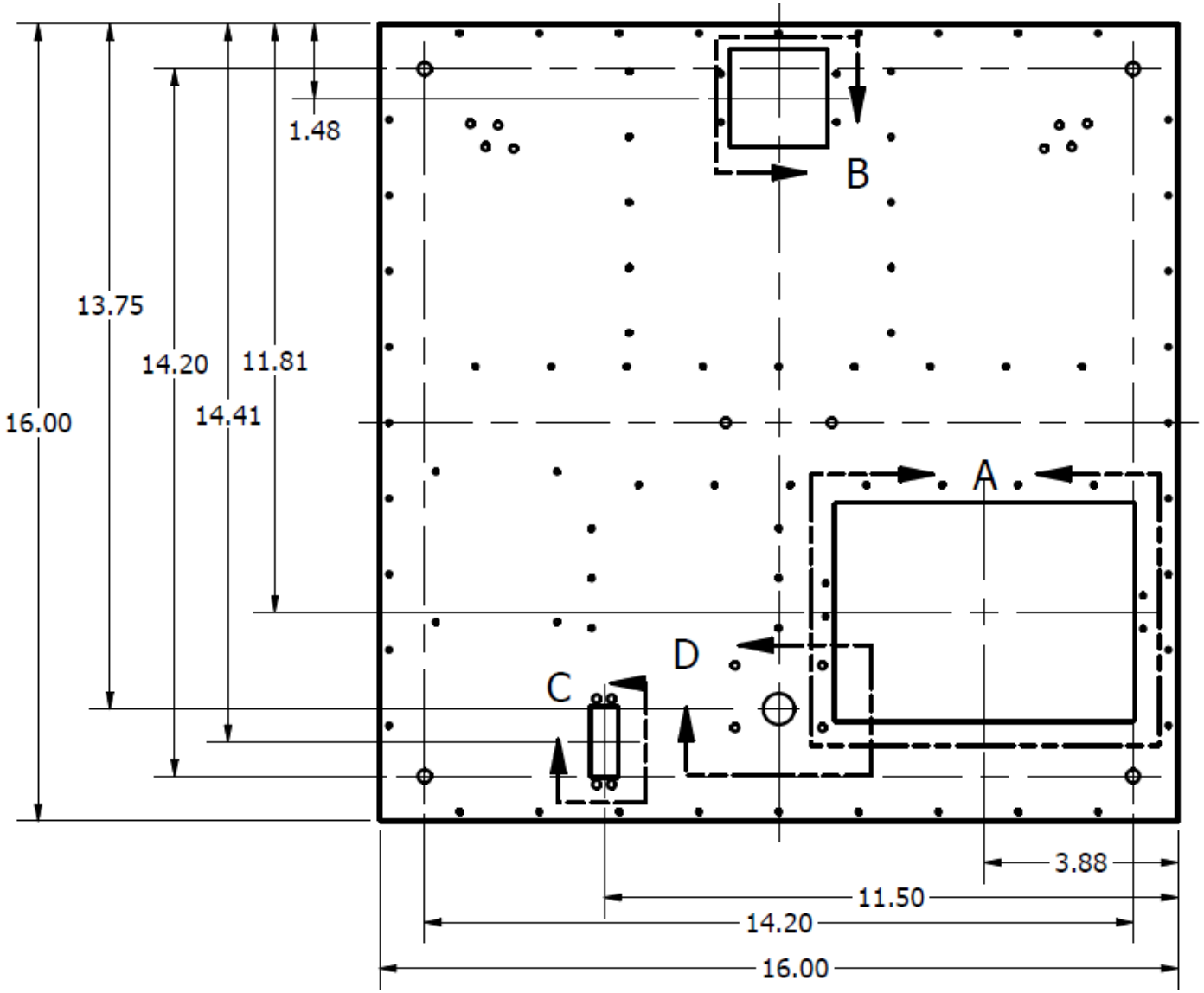

NOTES:
1. Part to be fabricated from .025" thick sheet.
2. Part to be free of burrs and sharp edges.

Dimensional Tolerances Unless Otherwise Specified
Machining
Fractions: ±1/64, Angles:±1°
2 place decimals: ±0.010, 3 place decimals: ±0.005
Unmarked surface finishes: 125 RMS or better
Castings
d < 1": ±1/64, 1" < d < 12": ±1/32, d > 12": ±1/16
Angles: ±1°, Concentricity: 0.03 T.I.R.

Notes:

This drawing exists as a solid model. Please contact the designer if desired.

REV	DESCRIPTION	DATE	APPROVED
1	RELEASED		RJC

Unmanned Systems Lab
Virginia Tech
Blacksburg, VA
http://www.me.vt.edu/unmanned/

Floorboard, Tethered Vehicle

Drawn	Checked	Date	Drawing No.	Rev
RJC	RJC		V-FLR	1

Scale	Part No.	Size
	V-FLR	A

MATERIAL: 6061 Aluminum

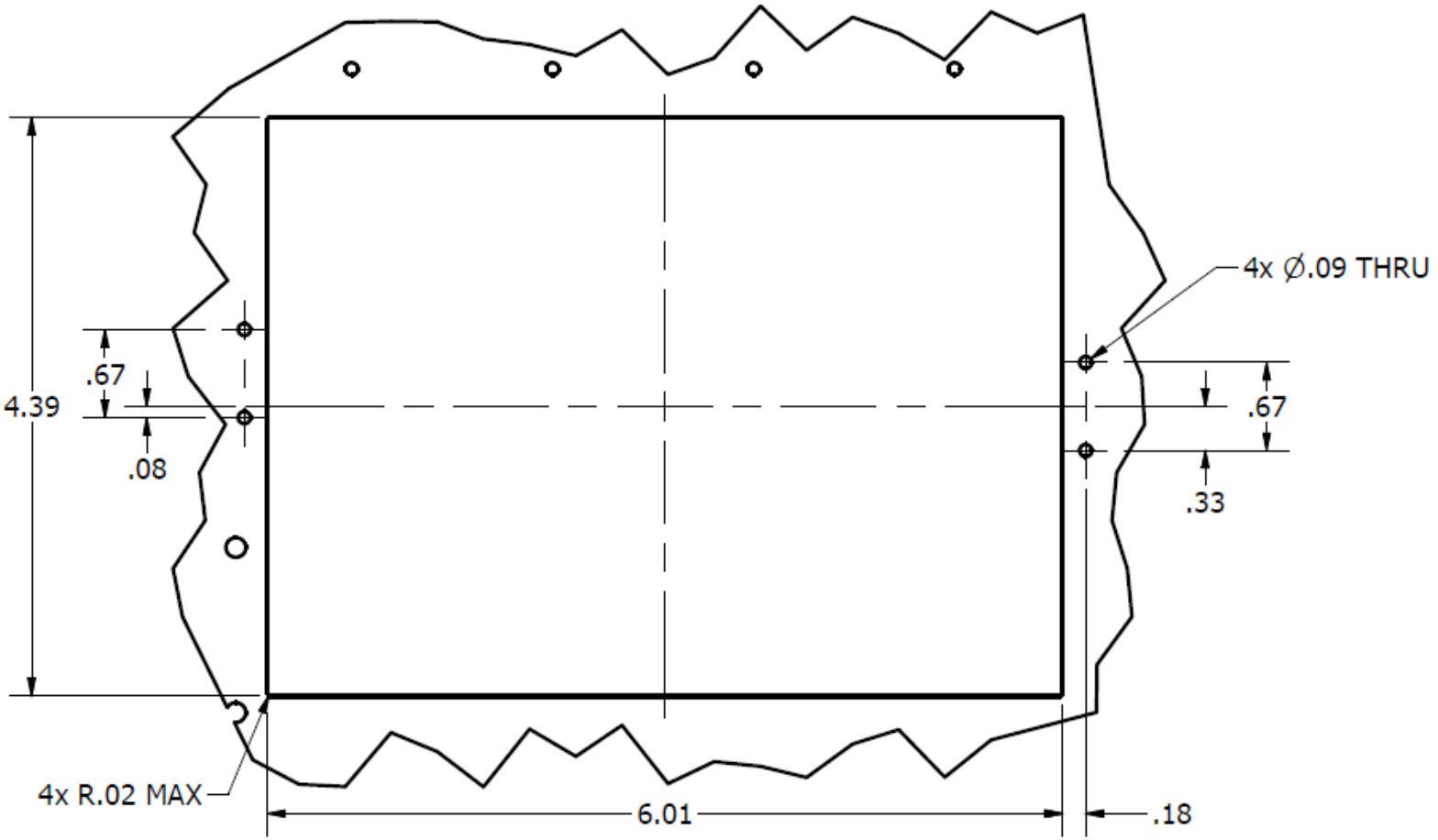

DETAIL A
SCALE .75

Dimensional Tolerances Unless Otherwise Specified
Machining
Fractions: ±1/64, Angles:±1°
2 place decimals: ±0.010, 3 place decimals: ±0.005
Unmarked surface finishes: 125 RMS or better
Castings
d < 1": ±1/64, 1" < d < 12": ±1/32, d > 12": ±1/16
Angles: ±1°, Concentricity: 0.03 T.I.R.

Notes:

This drawing exists as a solid model. Please contact the designer if desired.

Unmanned Systems Lab
Virginia Tech
Blacksburg, VA
http://www.me.vt.edu/unmanned/

Floorboard, Tethered Vehicle

Drawn	Checked	Date	Drawing No.	Rev
RJC	RJC		V-FLR	1

Scale	Part No.	Size
	V-FLR	A

MATERIAL: 6061 Aluminum

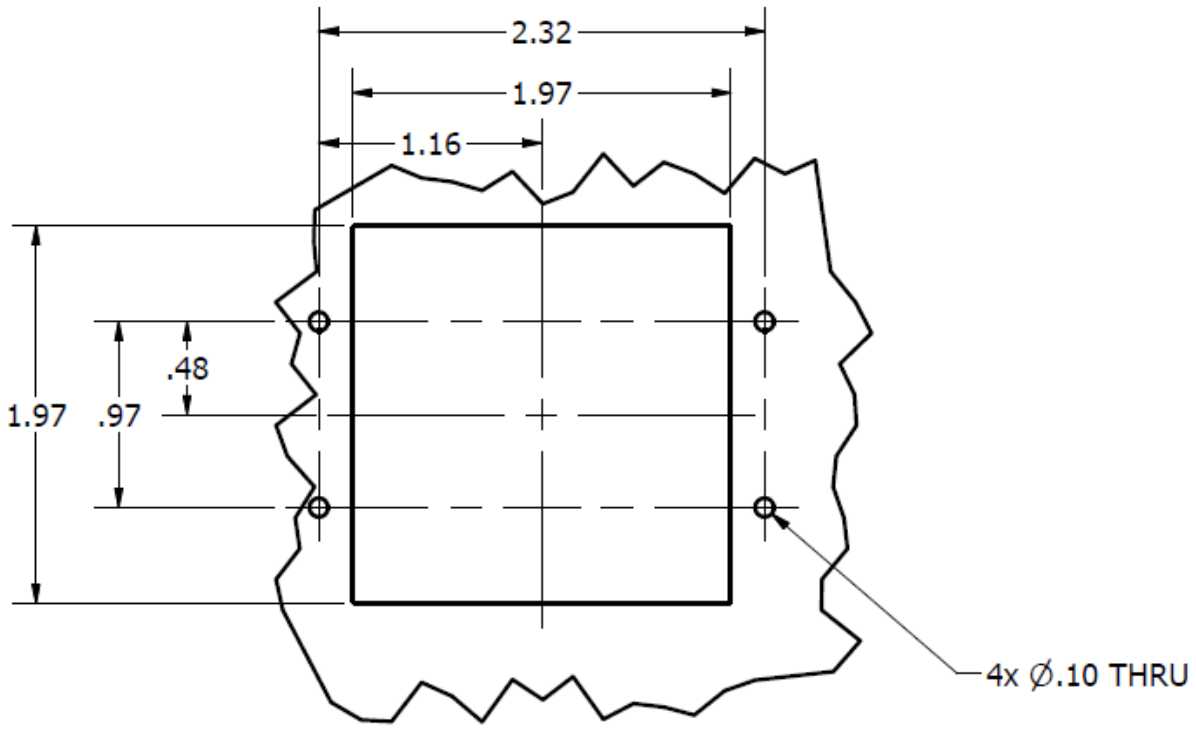

DETAIL B
SCALE 1

Dimensional Tolerances Unless Otherwise Specified
Machining
Fractions: ±1/64, Angles:±1°
2 place decimals: ±0.010, 3 place decimals: ±0.005
Unmarked surface finishes: 125 RMS or better
Castings
d < 1": ±1/64, 1" < d < 12": ±1/32, d > 12": ±1/16
Angles: ±1°, Concentricity: 0.03 T.I.R.

Notes:

This drawing exists as a solid model. Please contact the designer if desired.

Unmanned Systems Lab
Virginia Tech
Blacksburg, VA
http://www.me.vt.edu/unmanned/

Floorboard, Tethered Vehicle

Drawn	Checked	Date	Drawing No.	Rev
RJC	RJC		V-FLR	1

Scale	Part No.	Size
	V-FLR	A

MATERIAL: 6061 Aluminum

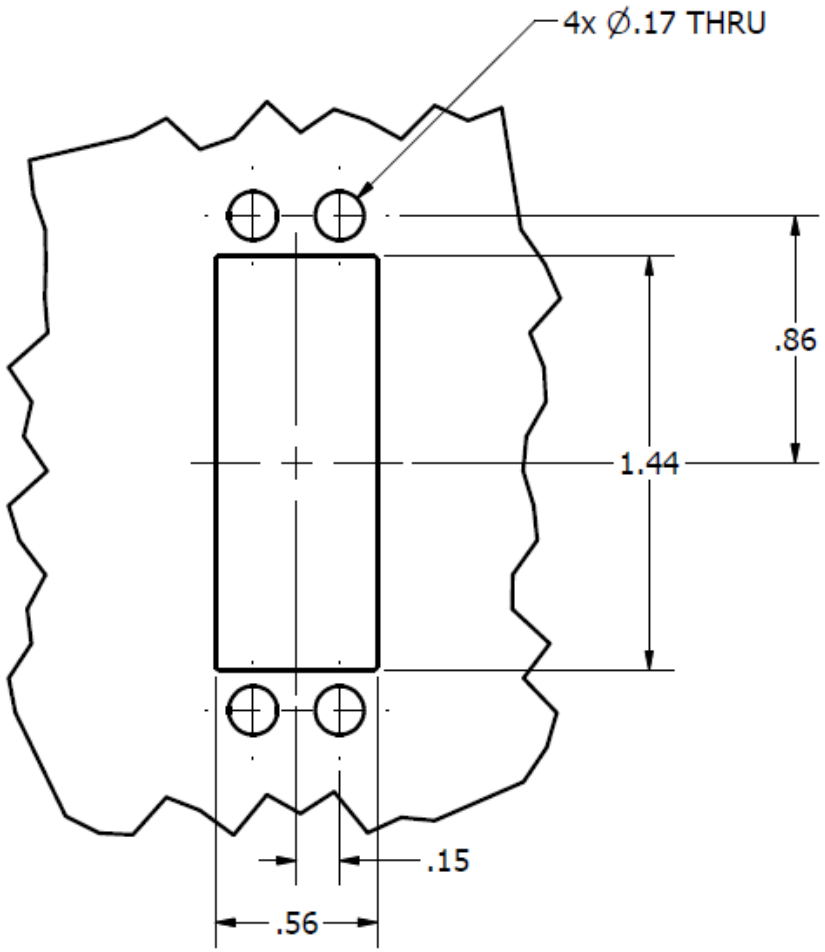

DETAIL C
SCALE 1.5

Dimensional Tolerances Unless Otherwise Specified
Machining
Fractions: ±1/64, Angles:±1°
2 place decimals: ±0.010, 3 place decimals: ±0.005
Unmarked surface finishes: 125 RMS or better
Castings
d < 1": ±1/64, 1" < d < 12": ±1/32, d > 12": ±1/16
Angles: ±1°, Concentricity: 0.03 T.I.R.

Notes:

This drawing exists as a solid model. Please contact the designer if desired.

Unmanned Systems Lab
Virginia Tech
Blacksburg, VA
http://www.me.vt.edu/unmanned/

Floorboard, Tethered Vehicle

Drawn	Checked	Date	Drawing No.	Rev
RJC	RJC		V-FLR	1

Scale	Part No.	Size
	V-FLR	A

MATERIAL: 6061 Aluminum

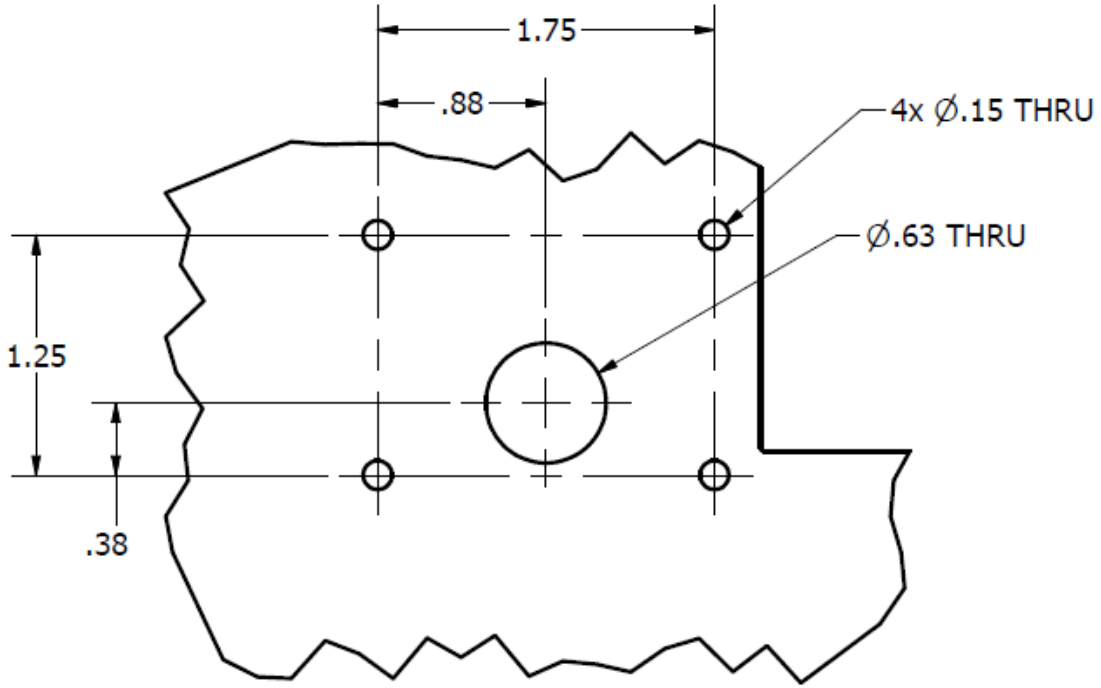

DETAIL D
SCALE 1

Dimensional Tolerances Unless Otherwise Specified
Machining
Fractions: ±1/64, Angles:±1°
2 place decimals: ±0.010, 3 place decimals: ±0.005
Unmarked surface finishes: 125 RMS or better
Castings
d < 1": ±1/64, 1" < d < 12": ±1/32, d > 12": ±1/16
Angles: ±1°, Concentricity: 0.03 T.I.R.

Notes:

This drawing exists as a solid model. Please contact the designer if desired.

Unmanned Systems Lab
Virginia Tech
Blacksburg, VA
http://www.me.vt.edu/unmanned/

Floorboard, Tethered Vehicle

Drawn	Checked	Date	Drawing No.	Rev
RJC	RJC		V-FLR	1

Scale	Part No.	Size
	V-FLR	A

MATERIAL: 6061 Aluminum

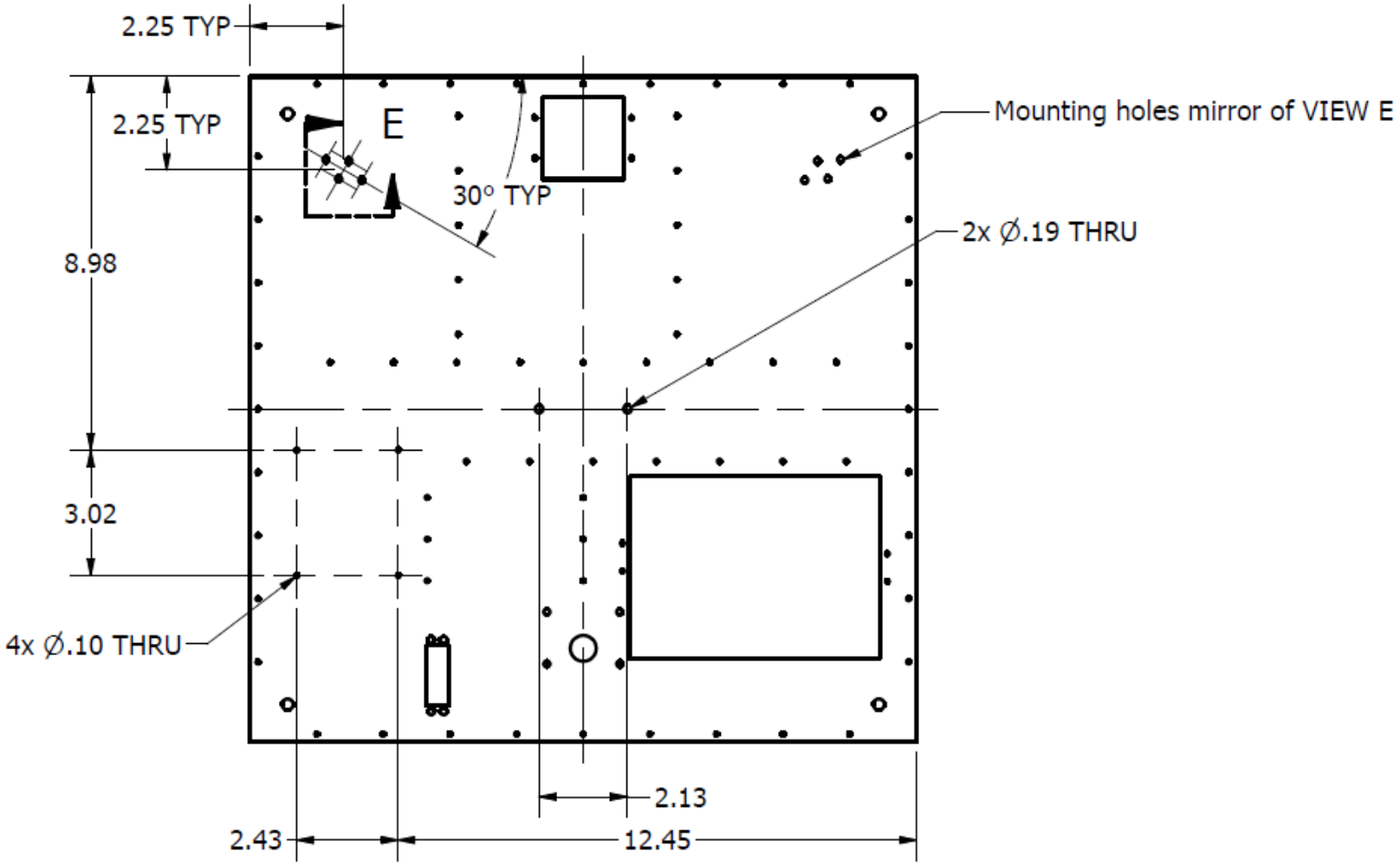

Dimensional Tolerances Unless Otherwise Specified
Machining
Fractions: ±1/64, Angles:±1°
2 place decimals: ±0.010, 3 place decimals: ±0.005
Unmarked surface finishes: 125 RMS or better
Castings
d < 1": ±1/64, 1" < d < 12": ±1/32, d > 12": ±1/16
Angles: ±1°, Concentricity: 0.03 T.I.R.

Notes:

This drawing exists as a solid model. Please contact the designer if desired.

Unmanned Systems Lab
Virginia Tech
Blacksburg, VA
http://www.me.vt.edu/unmanned/

Floorboard, Tethered Vehicle

Drawn	Checked	Date	Drawing No.	Rev
RJC	RJC		V-FLR	1

Scale	Part No.	Size
	V-FLR	A

MATERIAL: 6061 Aluminum

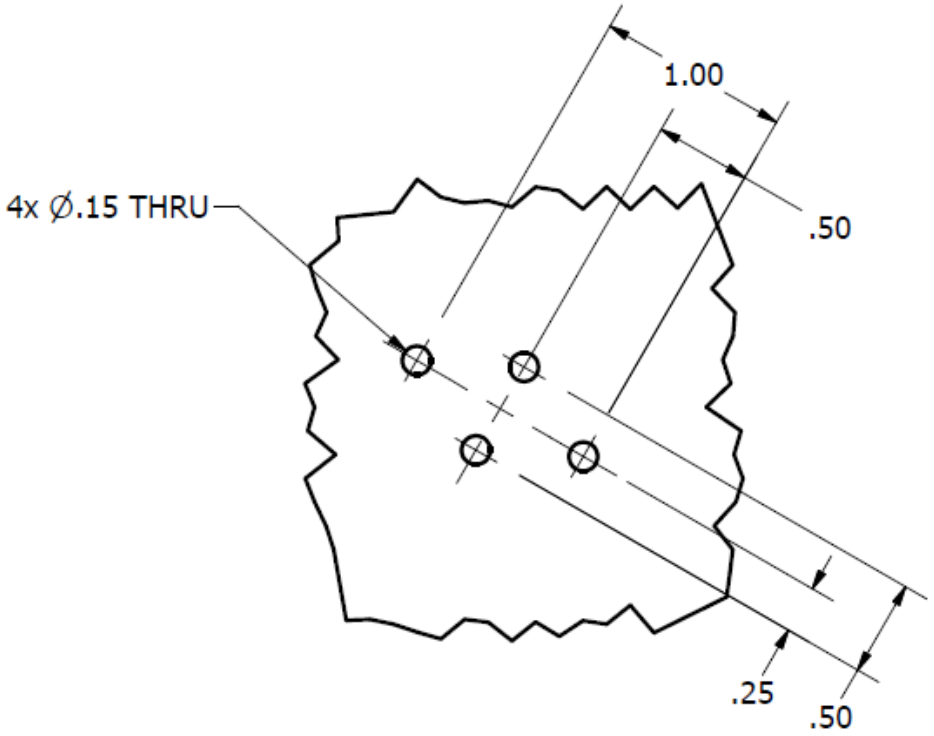

DETAIL E
SCALE 1

Dimensional Tolerances Unless Otherwise Specified
Machining
Fractions: ±1/64, Angles:±1°
2 place decimals: ±0.010, 3 place decimals: ±0.005
Unmarked surface finishes: 125 RMS or better
Castings
d < 1": ±1/64, 1" < d < 12": ±1/32, d > 12": ±1/16
Angles: ±1°, Concentricity: 0.03 T.I.R.

Notes:

This drawing exists as a solid model. Please contact the designer if desired.

Unmanned Systems Lab
Virginia Tech
Blacksburg, VA
http://www.me.vt.edu/unmanned/

Floorboard, Tethered Vehicle

Drawn	Checked	Date	Drawing No.	Rev
RJC	RJC		V-FLR	1

Scale	Part No.	Size
	V-FLR	A

MATERIAL: 6061 Aluminum

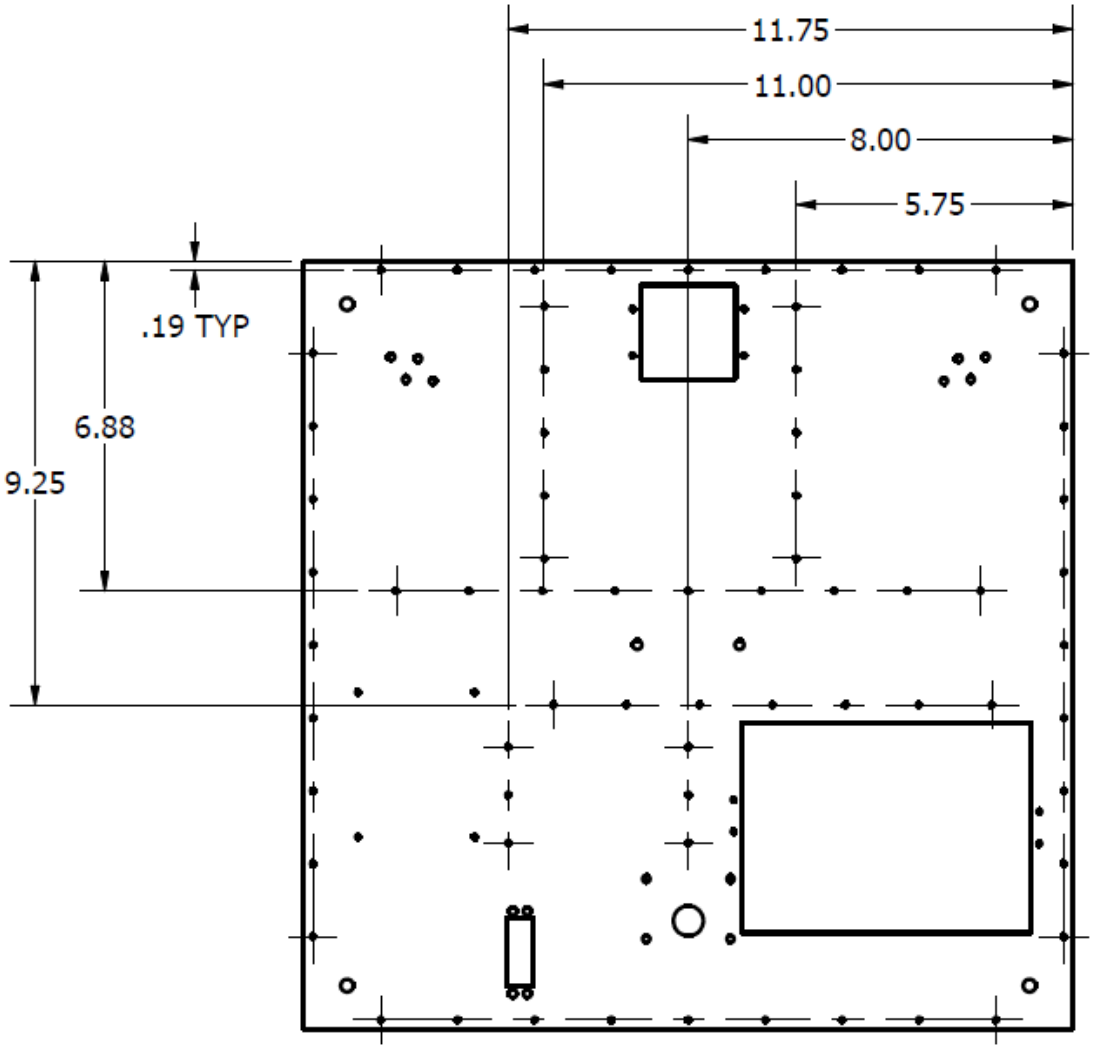

Dimensional Tolerances Unless Otherwise Specified
Machining
Fractions: ±1/64, Angles:±1°
2 place decimals: ±0.010, 3 place decimals: ±0.005
Unmarked surface finishes: 125 RMS or better
Castings
d < 1": ±1/64, 1" < d < 12": ±1/32, d > 12": ±1/16
Angles: ±1°, Concentricity: 0.03 T.I.R.

Notes:

This drawing exists as a solid model. Please contact the designer if desired.

Unmanned Systems Lab
Virginia Tech
Blacksburg, VA
http://www.me.vt.edu/unmanned/

Floorboard, Tethered Vehicle

Drawn	Checked	Date	Drawing No.	Rev
RJC	RJC		V-FLR	1

Scale	Part No.	Size
	V-FLR	A